Metallaboratrane Facilitated E–H Bond Activation and Hydrogenation Catalysis

Thesis by
Henry Fong

In Partial Fulfillment of the Requirements for the
Degree of
Doctor of Philosophy

CALIFORNIA INSTITUTE OF TECHNOLOGY
Pasadena, California
2015
(Defended December 5, 2014)

Acknowledgements

First and foremost, I would like to thank my advisor Prof. Jonas Peters. Graduate school is a formative period in a young scientist's development, and I would not have grown into the scientist that I am today without Jonas's mentorship. Jonas took a chance on me when I was a graduate student in my first quarter at Northwestern University in 2009. I contacted him about joining his research group, and within a few days he accepted me into his lab at Caltech. I am truly grateful for this. Jonas's attention to detail, scientific rigor, and approach to research can be summed in a phrase he once told me, "Do it once, and do it right." Ever since then I have approached my work, both in- and outside of chemistry, by this maxim. This and other lessons from Jonas will remain with me as I embark on my career. I am proud to call him my advisor and scientific mentor.

I would also like to acknowledge my committee members: Prof. Theodor Agapie (chair), Prof. Sarah Reisman, and Prof. Harry Gray. Needless to say, the periods leading up to committee meetings and oral exams were invariably stressful, but my committee members always made me feel at ease. I came out of these meetings and exams reinvigorated. They were genuinely interested in my work and ideas, and I appreciated their constructive criticisms and truly enjoyed the discussions.

I was also very fortunate to have worked alongside a group of talented individuals in the Peters lab. Each and every member of the group, past and present, has provided me with both professional and personal support throughout my tenure in the group. I would like to mention a few in particular. Prof. Marc-Etienne Moret, with whom I concurrently joined the group, was always generous with his time and effort whenever I needed help and advice. Marc-Etienne,

Dr. Daniel Suess, and Prof. Hill Harman, who was also my graduate student mentor when I was an undergraduate in the Chris Chang Group at Berkeley, were instrumental in helping me develop a nuanced view of chemical bonding and reactivity. I learned a large number of synthetic inorganic chemistry techniques from Prof. Yunho Lee and Prof. Caroline Saouma. Dr. Charlene Tsay taught me X-ray crystallography. When times were tough, I relied on the calming influence of Dr. Samantha MacMillan and the optimism of Dr. David Lacy. Dr. John Anderson was a blast to be around in the lab. Dr. Ayumi Takaoka, Alicia Chang, and I overlapped as undergraduates in the Chris Chang Group at Berkeley; I will always think fondly back upon the years we worked in the same lab space. Dr. Charles McCrory taught me nearly all I know about electrochemistry, and I will miss the near daily lunches that we had together. I will also miss working with Jonathan "JR" Rittle, Sidney Creutz, and Dr. Tzu-Pin Lin; all of whom I could always turn to for invigorating discussions. I have also had the privilege of working alongside Prof. Chris Uyeda, Dr. Yichen Tan, Dr. Gäel Ung, Dr. Miles Johnson, Kenny Lotito, Joe Rheinhardt, Ben Matson, Trevor Del Castillo, Tanvi Ratani, Mark Nesbit, Joe Ahn, Niklas Thompson, Kareem Hannoun, Trixia Buscagan, and Gregory Harlow.

One of the highlights of my graduate studies has been performing two separate and rare single crystal neutron diffraction experiments at the Spallation Neutron Source at Oak Ridge National Laboratory in Tennessee. The experiment and structure determination would not have been possible without the help and support of the instrument team: Dr. Xiaoping Wang, Dr. Christina Hoffmann, and Helen He.

In the last two-and-a-half years of my graduate studies, I also worked in the Molecular Catalysis group at the Joint Center for Artificial Photosynthesis (JCAP). The unique,

interdisciplinary research structure at JCAP afforded me a learning experience that complemented my time in a traditional research group setting. I am grateful to have had the chance to interact with Prof. Cliff Kubiak, who is the Project Lead of Molecular Catalysis, as well as Prof. Carl Koval, Prof. Jenny Yang, Dr. Daniel Sieh, Dr. Oana Luca, Dr. David Shaffer, Dr. Suho Jung, Alyssia Lilio, and Michelle Hansen.

I would not have been able to perform my research without the assistance of the technical staff at Caltech. Dr. David VanderVelde has on several occasions helped me setup key NMR experiments. Critical parts of my work would not have been possible without X-ray crystallographic assistance from Dr. Mike Takase and Larry Henling, the latter of whom is kind enough to mount crystals at any hour. Dr. Nathan Dalleska of the Environmental Analysis Center at Caltech provided valuable assistance with gas-chromatography analysis.

I have also immensely enjoyed the company of my friends at Caltech outside of the lab. I have had a lot of fun playing intramural and recreational league basketball for the "Labinger Panthers," "3 Turnovers-per-hour" (named after my slow catalysts), and "Buckets." The teammates with whom I've shared this experience include Prof. Tom Teets, Prof. Ian Tonks, Marc-Etienne, Charles McCrory, John Anderson, Josh Buss, Matt Chao, Matt Kovach, Dr. Graham de Ruiter, Dr. Aaron Sattler, Dr. Wes Sattler, Adam Nichols-Nielander, Connie Wang, and last but not least, Guy Edouard, whose easy-going attitude and comic attributes can turn even our most crushing losses into something to laugh about.

I have also been very fortunate to attend graduate school close to my extended family and friends. Their support and love throughout this period has helped me maintain a healthy work-life balance. My grandparents, all of my aunts and uncles, as well as my sister Jessica have

kept me in touch with the real world outside of the graduate school bubble. Alfred Tran, Karyee Chow, Connie Tat, and Melody Wong have taken me out on many tasty and re-energizing coffee and dinner outings throughout L.A. I would also like to thank Julia Ding, who not only didn't run-away when I uttered the words "nitrogenase" and "CO_2 hydrogenation" on our first date, but has been my most enthusiastic supporter since. Her passion for and hard-work in her own profession has helped motivate me in my own work, as well.

Finally, I dedicate this thesis to my Dad, Kim Soon Fong, who passed-away two months prior to my graduation from Berkeley, and to my Mom, Fanny Fong, who has bravely gone through so much since then. Both of my parents instilled in me the importance of hard-work and education, and I hope that this thesis makes them proud.

Abstract

The E–H bond activation chemistry of *tris*-phosophino-iron and -cobalt metallaboratranes is discussed. The ferraboratrane complex (**TPB**)Fe(N_2) heterolytically activates H–H and the C–H bonds of formaldehyde and arylacetylenes across an Fe–B bond. In particular, H–H bond cleavage at (**TPB**)Fe(N_2) is reversible and affords the iron-hydride-borohydride complex (**TPB**)(μ–H)Fe(L)(H) (L = H_2, N_2). (**TPB**)(μ–H)Fe(L)(H) and (**TPB**)Fe(N_2) are competent olefin and arylacetylene hydrogenation catalysts. Stoichiometric studies indicate that the B–H unit is capable of acting as a hydride shuttle in the hydrogenation of olefin and arylacetylene substrates. The heterolytic cleavage of H_2 by the (**TPB**)Fe system is distinct from the previously reported (**TPB**)Co(H_2) complex, where H_2 coordinates as a non-classical H_2 adduct based on X-ray, spectroscopic, and reactivity data. The non-classical H_2 ligand in (**TPB**)Co(H_2) is confirmed in this work by single crystal neutron diffraction, which unequivocally shows an intact H–H bond of 0.83 Å in the solid state. The neutron structure also shows that the H_2 ligand is localized at two orientations on cobalt *trans* to the boron. This localization in the solid state contrasts with the results from ENDOR spectroscopy that show that the H_2 ligand freely rotates about the Co–H_2 axis in frozen solution. Finally, the (**TPB**)Fe system, as well as related *tris*-phosphino-iron complexes that contain a different apical ligand unit (Si, PhB, C, and N) in place of the boron in (**TPB**)Fe, were studied for CO_2 hydrogenation chemistry. The (**TPB**)Fe system is not catalytically competent, while the silicon, borate, carbon variants, (**SiP$^{R}_{3}$**)Fe, (**PhBP$^{iPr}_{3}$**)Fe, and (**CP$^{iPr}_{3}$**)Fe, respectively, are catalysts for the hydrogenation of CO_2 to formate and methylformate. The hydricity of the CO_2 reactive species in the silatrane system (**SiP$^{iPr}_{3}$**)Fe(N_2)(H) has been experimentally estimated.

Table of Contents

Detailed Table of Contents

List of Figures

List of Schemes

List of Charts

List of Tables

List of Abbreviations

$(BH)^+$	Generic conjugate acid of base B
[M]	Generic transition metal complex
$\{^1H\}$	Proton decoupled
$\{^{31}P\}$	Phosphorous decoupled
°	Degree
^{11}B	Boron-11
^{13}C	Carbon-13
^{19}F	Fluorine-19
^1H	Hydrogen-1
^{29}Si	Silicon-29
^2H	Hydrogen-2 *or* deuterium
2-Me-THF	2-Methyl-tetrahydrofuran
^{31}P	Phosphorous-31
6-311G(d)	Basis sets for DFT
Å	Angstrom
A	Hyperfine coupling constant
Abs	Absorbance
Anal	Analysis
Ar	Generic aryl group
asym	Asymmetric

atm	Atmosphere
ATR	Attenuated total reflectance
au^{-3}	Inverse cubic atomic units
B	Generic base
$B(mim^{tBu})_3$	*tris*(2-mercapto-1-*tert*-butyl-imidazolyl)-borane
$B(NIn)_3$	*tris*(1H-pyrrolo-2-3-pyridin-1-yl)borane
B3LYP	DFT functionals
$BAr^F{}_4$	$[B(3,5\text{-}(CF_3)_2\text{-}C_6H_3)_4]^-$
br	Broad
BZQ	Benzo[*h*]quinolin-10-yl
C	Celsius
C(sp)	s-p Hybridized carbon atom
$C(sp^2)$	$s\text{-}p^2$ Hybridized carbon atom
calc'd	Calculated
C_{Ar}	Carbon atom of an aryl group
C_{ipso}	Ipso carbon atom
cm^{-1}	Wave numbers
C_n	n-Fold rotational symmetry
COD	Cyclooctadiene
$CP^{iPr}{}_3$	$[C(o\text{-}C_6H_4P^iPr_2)_3]^-$
$C^{Si}P^{Ph}{}_3$	$[C(Si(CH_3)_2CH_2PPh_2)_3]^-$

CW	Continuous-wave
Cy	Cyclohexyl
D	Deuterium
d	Doublet *or* deuterium
d-d	Doublet-of-doublets
DFT	Density Functional Theory
DMF	Dimethylformamide
E	Generic main-group element
ENDOR	Electron nuclear double resonance
EPR	Electron paramagnetic resonance
Et	Ethyl
FID	Flame ionization detector
FpH	$(C_5H_5)Fe(CO)_2(H)$
G	Gibbs free energy
g	grams
GC	Gas chromatography
GHz	Megahertz
h	Hour(s)
HMDSO	Hexamethyldisiloxane
I	Nuclear spin
*i*Pr *or* ^{i}Pr	iso-Propyl

IR	Infrared
J	NMR coupling constant
K	Kelvin
K_a	Acid dissociation constant
kcal	Kilocaloies
K_{eq}	Equilibrium constant
L	Generic L-type ligand
LF	Ligand field
m	Medium *or meta or* multiplet
M	Generic transition metal *or* molar
MeCN	Acetonitrile
Mes	Mesityl
mg	Milligrams
MHz	Gigahertz
mL	Milliliters
mm	Millimeter
mmol	Millimoles
M^{n+}	Generic transition metal of oxidation state n
mol	Moles
MS	Mass spectrometry
$^{n}J_{x-y}$	NMR coupling constant between nuclei x and y through n bonds

nm	Nanometer
NMR	Nuclear magnetic resonance
NP^{iPr}_3	$N(CH_2CH_2P^iPr_2)_3$
o	*ortho*
OTf	SO_2CF_3
p	*para*
PDI	$2,6\text{-}(ArNC(CH_3)_2)_2C_5H_3N$
PNP	$2,6\text{-}(^iPr_2PCH_2)_2C_5H_3N$
Ph	Phenyl
$PhBP^{iPr}_3$	$[PhB(CH_2P^iPr_2)_3]^-$
pK_a	Negative logarithm of acid dissociation constant K_a
PP_3	$P(CH_2CH_2PPh_2)_3$
ppm	Parts per million
quart	Quartet
quin	Quintet
R	Gas constant *or* generic functional group
$^RDPB^{Ar}$	$Ar(o\text{-}C_6H_4PR_2)_3B$
ref	Reference
RT	Room temperature
s	Singlet *or* strong
S	Spin

SiP^{iPr}_3	$[Si(o\text{-}C_6H_4P^iPr_2)_3]^-$
SiP^{Ph}_3	$[Si(o\text{-}C_6H_4PPh_2)_3]^-$
sym	Symmetric
T	Temperature
t	Triplet
T_{1min}	Minimum spin-lattice relaxation time
TBAF	Tetrabutylammonium fluoride
TBP	Trigonal bipyramidal
*t*Bu *or* ^{t}Bu	*tert*-Butyl
TCD	Thermal conductivity detector
t-d	Triplet-of-doublets
tetraphos	$P(o\text{-}C_6H_4P^iPr_2)_3$
THF	Tetrahydrofuran
TOF	Time-of-flight *or* turnover frequency
Tol	Tolyl
TPB	$B(o\text{-}C_6H_4P^iPr_2)_3$
TPBD	$[DB(o\text{-}C_6H_4P^iPr_2)_3]^-$
TPBH	$[HB(o\text{-}C_6H_4P^iPr_2)_3]^-$
triphos	$CH_3CH(CH_2PPh_3)_3$
UV	Ultraviolet
vis	Visible

w	Weak
wR	Weighted R-factor
X	Generic X-type ligand
XRD	X-ray diffraction
XTm^{tBu}	*tris*(2-mercapto-1-*tert*-butylimidazolyl)-X-borate
δ	Chemical shift
Δ	Difference
ΔG_H-	Hydricity
ε	Extinction coefficient
η^x	Heptacity of order X
κ^n	Denticity involving n atoms
λ	Wavelength
μ_B	Bohr magneton
μ_{eff}	Effective magnetic moment
μL	Microliters
μM	Micromolar
μmol	Micromoles
μ–X	Bridging X ligand
π	Pi-symmetry orbital
σ	Sigma symmetry orbital
Σ(X−Y−Z)	Sum of angles defined by atoms X−Y−Z

Chapter 1. Introduction

1.1 Motivation

Metal catalyzed bond forming and bond cleavage reactions have played a large role in the growth of organometallic chemistry for decades.[1] These bond forming and bond breaking transformations require the formal transfer of multielectron equivalents. Noble metals, such as ruthenium, rhodium, iridium, palladium, and platinum, have proven to be particularly adept at catalyzing these reactions. This is in part due to the predisposition of noble metals to undergo controlled multielectron processes. The hydrogenation of unsaturated E=C bonds is the prototypical two-electron bond forming reaction catalyzed by organometallic complexes. Thus, the principles of hydrogenation chemistry can provide a framework by which to understand related metal-catalyzed bond forming and bond breaking reactions.

The discovery of $RhCl(PPh_3)_3$ (Wilkinson's catalyst)[2-3] is one of the most important developments in hydrogenation chemistry. The catalyst can operate at ambient temperatures and pressures in the presence of ethanol as a co-solvent. It rapidly hydrogenates unconjugated olefins and acetylenes and is selective for the hydrogenation of olefins in the presence of ester, ketone , and nitroarene functional groups.[4] The kinetics for olefin hydrogenation by the Wilkinson system has been extensively studied by Halpern.[5-6] The core of the catalytic cycle deduced from Halpern's studies is shown in Scheme 1.1A, and it illustrates some of the features of a classical (hydrogen-first) hydrogenation mechanism. Notable in the catalytic cycle are the controlled two electron steps that cycle the metal center between formal Rh^{I} and Rh^{III} oxidation states. The Rh^{I} species **B** oxidatively adds H_2 to afford the Rh^{III}-dihydride **C**. Subsequent olefin coordination followed by migratory insertion steps afford species **D** and **E**,

respectively. The product alkane is then released by reductive elimination from the Rh^{III} species **E** to regenerate the Rh^{I} species **B** and closure of catalytic cycle. Analogous mechanisms involving the transfer of both hydride equivalents from a dihydride intermediate, as in the Wilkinson system, and the similar elementary steps have been discovered for related catalysts.

Scheme 1.1 Catalytic cycles for olefin hydrogenation.

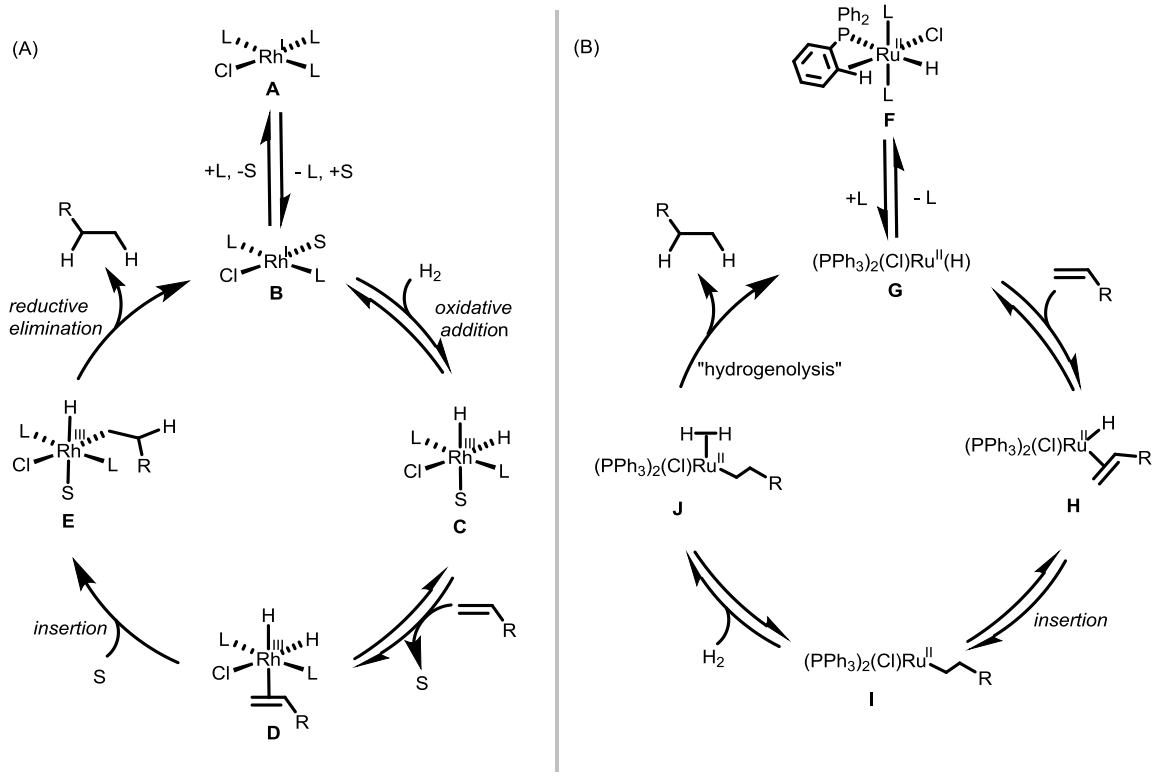

(A) Core of the catalytic cycle for Wilkinson's catalyst. (B) Catalytic cycle for $Ru(PPh_3)_3(Cl)(H)$. L = PPh_3, S = co-solvent.

Some other catalysts for olefin hydrogenation do not involve oxidative addition and reductive elimination processes.[7] For example, the $Ru(PPh_3)_3(H)(Cl)$ complex (also discovered

by Wilkinson) is a catalyst with selectivity for the hydrogenation of terminal over internal olefins.[8] The proposed catalytic for hydrogenation by this Ru^{II} catalyst is shown in Scheme 1.1B.[9-11] The process involves olefin coordination to a metal-monohydride species (**G** to **H**) followed by insertion to afford a metal-alkyl species (**I**). H_2 coordination affords **J**. Release of the alkane product from the Ru-alkyl intermediate **J** to afford **G** occurs through hydrogenolysis. By avoiding oxidative addition and reductive elimination steps in the catalytic cycle, the ruthenium center maintains a Ru^{II} oxidation state, in contrast to the rhodium system. Other mechanisms for olefin hydrogenation exist,[12-14] but like the two mechanisms shown in Scheme 1.1 they rely on the stability of the catalyst to two-electron processes, both with and without formal oxidation state changes.

The development of well-defined late first-row transition metal complexes based on iron, cobalt, and nickel for hydrogenation catalysis has lagged behind that of their second and third row counterparts such as ruthenium, rhodium, iridium, palladium, and platinum.[15] Part of the reason for this is that these first-row transition metals tend to undergo undesirable one electron reactivity. Reflecting this challenge is the limited number of iron,[16-26] cobalt,[25,27-34] and nickel[32,34-39] catalyzed hydrogenations reported in the literature. Among these example, redox-active ligand and metal-ligand cooperativity strategies have emerged as two promising methods to engender catalytic reactivity for these first-row transition metal complexes under mild conditions.

Chirik reported in 2004 that ligand redox-noninnocent pyridyl-diimine-iron complex, (**PDI**)$Fe(N_2)_2$ (where PDI = 2,6-$(ArNC(CH_3)_2)C_5H_3N$), is a precatalyst for olefin

hydrogenation at ambient temperature and 1 atm H_2.[16] The proposed mechanism for the catalytic hydrogenation of olefins by (**PDI**)Fe$(N_2)_2$ (Scheme 1.2) is similar to the catalytic cycle presented for the Wilkinson catalyst. For (**PDI**)Fe$(N_2)_2$, the bound olefin of the iron-dihydride intermediate (**PDI**)Fe$(H)_2$(olefin) (**M**) inserts into one of the Fe–H bonds to form the iron-alkyl-hydride intermediate (**PDI**)Fe(H)(alkyl) (**N**). Subsequent reductive elimination of the product alkane from **N** reforms the three-coordinate (**PDI**)Fe intermediate **K** and closes the catalytic cycle. The redox-noninnocence of the PDI ligand in this system is significant. Combined experimental and DFT studies suggest that redox changes occur on the PDI ligand rather than the iron center during catalysis. For example, for the series of sequentially one

Scheme 1.2 Olefin hydrogenation by (**PDI**)Fe$(N_2)_2$, highlighting ligand redox non-innocence.

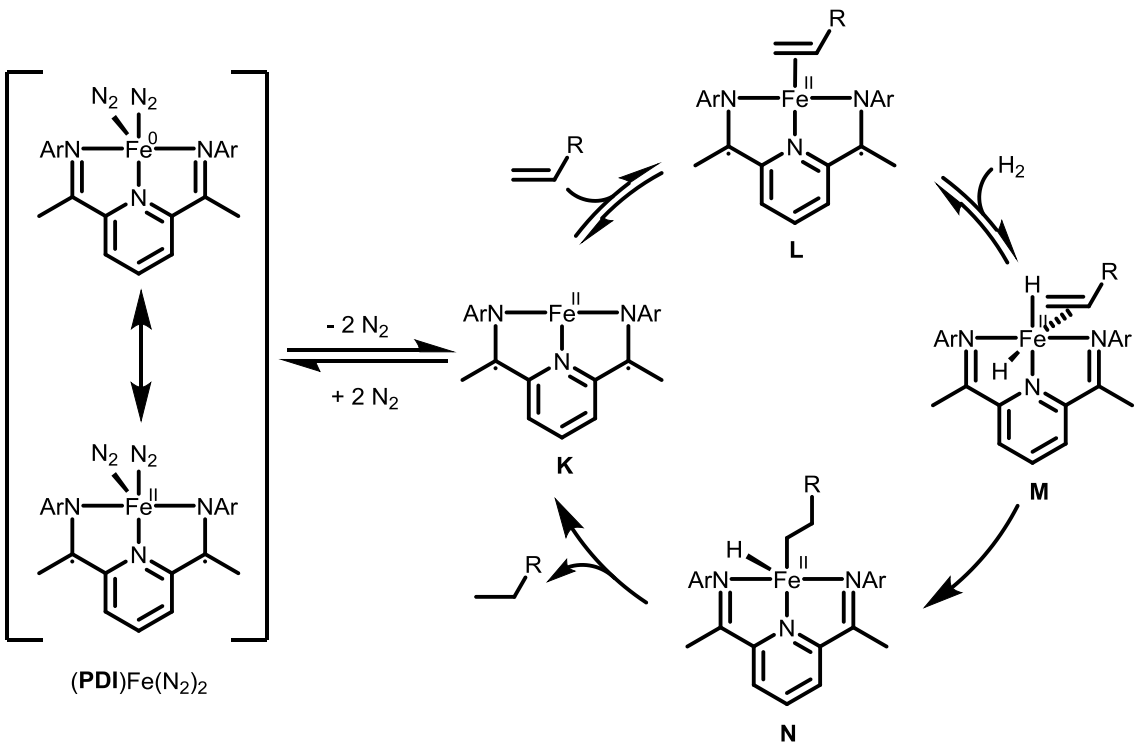

electron reduced complexes (**PDI**)$FeCl_2$, (**PDI**)FeCl, and (**PDI**)$Fe(N_2)_2$, the iron centers are all best formulated as Fe^{II} and the ligands as PDI, PDI^{1-}, and PDI^{2-}, respectively.[40] By maintaining an Fe^{II} oxidation state throughout the catalytic cycle, the iron center avoids an Fe^{IV} state or an Fe^0 state, which may not be supported by the PDI ligand by virtue of the oxidizing nature of the Fe^{IV} oxidation state and the mismatch between the hard nitrogen donors and soft, low valent iron center, respectively.

Milstein showed that the (**PNP**)Fe (PNP = 2,6-(^{i}Pr$_2$PCH$_2$)$_2$C$_5$H$_3$N) system heterolytically activates H_2 and catalytically hydrogenates ketones through metal-ligand cooperativity[41] at ambient temperature and a mild H_2 pressure (4 atm).[23] The proposed catalytic cycle for this

Scheme 1.3 (**PNP**)Fe(CO)(Br)(H) for ketone hydrogenation, highlighting metal-ligand cooperativity for H–H bond activation and hydrogenation catalysis.

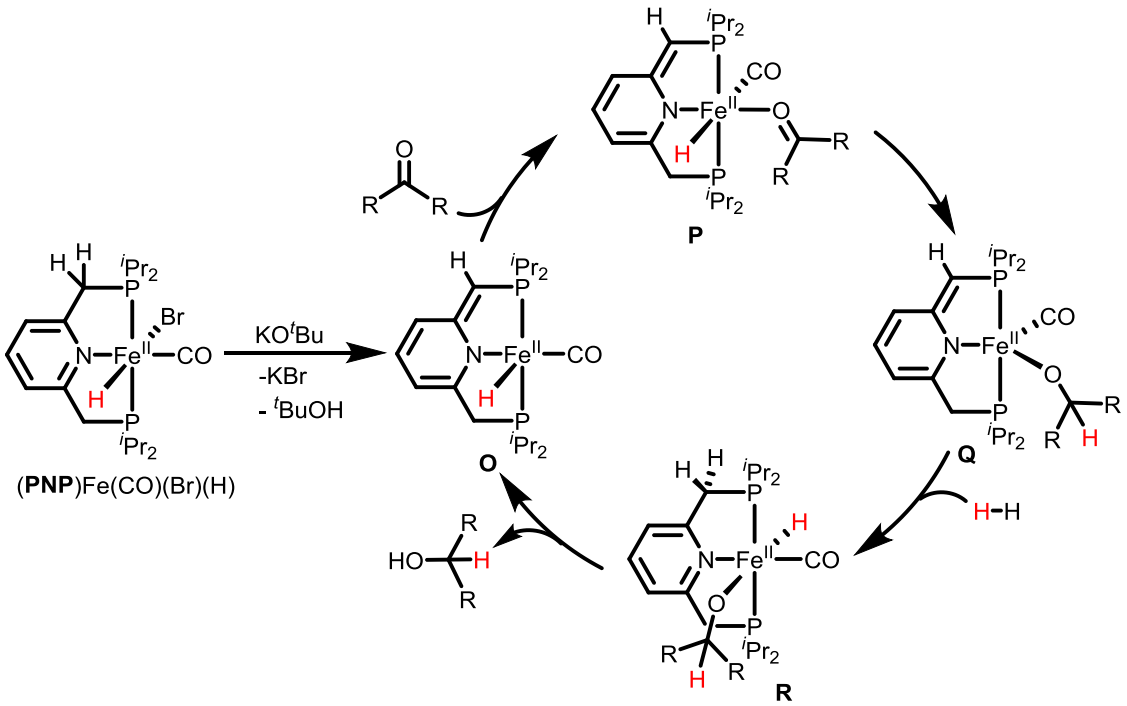

reaction is shown in Scheme 1.3. The precatalyst (**PNP**)Fe(CO)(Br)(H) enters the catalytic cycle through deprotonation of a benzylic C–H proton and bromide loss to afford the five-coordinate Fe^{II} species, (**PNP***)Fe(CO)(H) (**O**) (where PNP* is the dearomatized, deprotonated PNP ligand). The ketone subsequently pre-coordinates to the iron center (**P**) before it inserts into the *cis* Fe–H bond to afford the five-coordinate iron-alkoxide intermediate **Q**. Dihydrogen then adds to intermediate **Q** to afford **R**, in which the ligand is re-aromatized. Elimination of the product alcohol from **R** closes the catalytic cycle. Notable in the catalytic cycle is the metal-ligand cooperativity in the H–H bond cleavage step from **Q** to **R**; a hydride from H_2 is formally transferred to the iron center while the proton is transferred to the unsaturated, benzylic carbon atom. In the final elimination step that releases the alcohol product, it is not known experimentally whether it is the hydrogen from the Fe–H or the benzylic C–H that is directly transferred to the product. However, given the *trans* arrangement of the alkoxide to the Fe–H, transfer of the Fe–H is unlikely. A previous study on the (**PNP**)Ir analogue showed that D_2 addition to the dearomatized (**PNP***)IrX species results in the formation of *syn* arranged Ir-D and benzylic C-D bonds, and that E–H (E = $CH_2C(O)CH_3$ or H) elimination involves *syn* arranged Ir–E and benzylic C–D units.[42] The data collectively suggest that in the iron system the H atom from the benzylic C–H position situated *syn* to the alkoxide ligand is the most likely source of the proton on the alcohol product.

Metallaboratranes[i] are a promising alternative class of complexes for bond activation and catalysis. The Lewis acid BR_3 unit in a metallaboratrane can stabilize low valent and/or Lewis basic metal centers through a retrodative M→B interaction. These complexes may also activate small molecules (e.g., N_2, CO, or H_2) and E−H (e.g., C−H, H−H, N−H) bonds. In a (classical) scenario for the activation of H_2, the Lewis basicity of the metal center may react with the π-acidic H_2 ligand to afford a nonclassical H_2 adduct, classical dihydride, or an intermediate M−H_2 species intermediate of the two extremes (Scheme 1.4A top).[46] Alternatively, the Lewis basic, low valent metal and the Lewis acidic borane units can in principle work in tandem to heterolytically cleave the H−H bond to afford $[R_3B–H]^-$ and M−H linkages through the formal transfer of H^- to the borane and H^+ to the metal (Scheme 1.4A bottom, Scheme 1.4B). This reactivity contrasts with traditional metal-ligand cooperative H−H bond cleavage reactions, such as in the Milstein example presented above, where the Lewis acidic metal center accepts an H^- while a basic site on the ligand accepts H^+ from H_2 (Scheme 1.4C).[23] This type of reaction can be thought of as the "normal polarity" for heterolytic H−H bond cleavage. Heterolytic H_2 cleavage using a metallaboratrane is therefore a formal inversion to the polarity (i.e., "inverse polarity") of traditional metal-ligand facilitated H−H bond cleavage reactions (Scheme 1.4B). This strategy is reminiscent of H−H bond cleavage using frustrated Lewis acid-base pairs.[47] Given the success of metal-ligand cooperativity for hydrogenation catalysis,

[i] The metallaboratrane terminology has been used by Hill (see ref 43) to refer to a caged structure in which there exists a transannular dative metal-borane interaction and *three* supporting heterocylic bridges. Historically, the "atrane" terminology has also referred to transannular interactions supported by three heterocyclic bridges (see ref 44 and 45).

the cooperativity of the borane and metal in a metallaboratrane is a promising new strategy for hydrogenation catalysis. In fact, catalytic hydrogenation of alkenes and alkynes using metallaboratranes had not been reported prior to the start of my work on the ferraboratrane system discussed in this thesis.

Scheme 1.4 Heterolytic H–H bond cleavage and hydrogenation catalysis by a metallaboratranes**.**

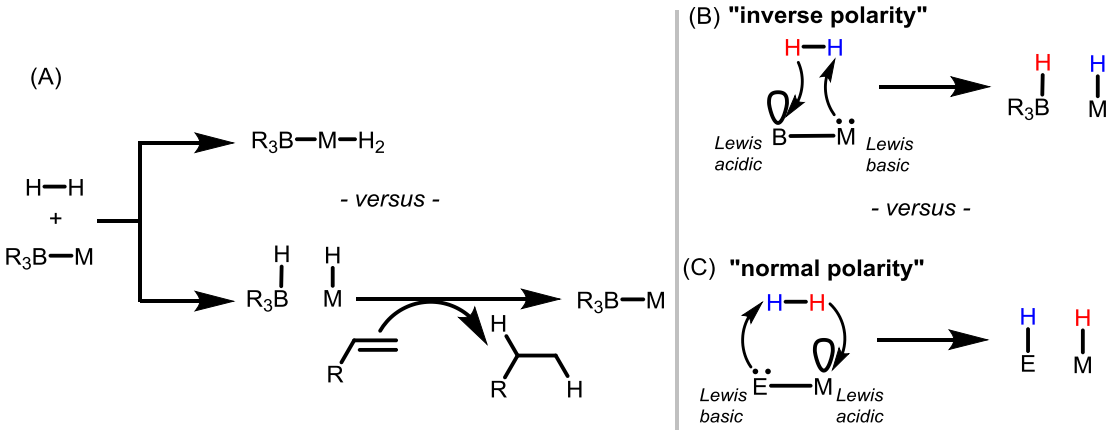

(A) H–H bond cleavage to a metallaboratrane results in bond H–H cleavage (bottom) or H_2 addition to the metal center as an H_2 adduct, dihydride, or an intermediate M–H_2 species (top). (B) "Inverse polarity" H–H bond cleavage. (C) "Normal polarity" H–H bond cleavage.

The following chapters of this thesis will discuss my studies on metallaboratrane facilitated E–H bond cleavage and hydrogenation catalysis. I will present my discoveries from my work on the (**TPB**)M system (TPB = (TPB = B(*o*-$C_6H_4P^iPr_2)_3$, M = Fe or Co) (Chart 1.1) for H_2 activation in Chapters 2 and 3. The olefin and arylacetylene hydrogenation chemistry of the (**TPB**)Fe system will also be discussed in Chapter 2. Chapter 4 will discuss the CO_2

hydrogenation chemistry of the (**TPB**)Fe and related iron-systems. For the remainder of this chapter, I will discuss some relevant aspects metallaboratrane and iron-hydride chemistry.

Chart 1.1 General forms of (**TPB**)MX and (**^{R}DPB^{Ar}**)MX complexes.

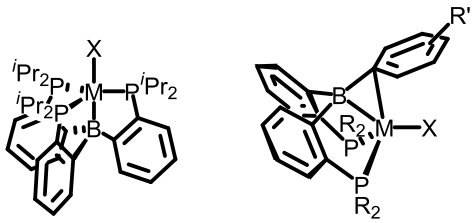

(**TPB**)MX (**^{R}DPB^{Ar}**)MX

1.2 X–Y Bond Activation and Hydride Transfer Using Metallaboratranes

1.2.1 Precedent for X–Y Bond Activation

Examples of bond activation by metallaboratranes are limited. Parkin reported the first example of X−Y bond cleavage across a M−B interaction in a metallaboratrane.[48] The ferraboratrane **B(mim^{tBu})$_3$**Fe(CO)$_2$ complex (B(mim^{tBu})$_3$ = *tris*(2-mercapto-1-*tert*-butyl-imidazolyl)-borane) undergoes a formal 1,2-addition of halogen containing X−Y bonds to afford (**XTm^{tBu}**)FeY (XTm^{tBu} = *tris*(2-mercapto-1-*tert*-butylimidazolyl)-X-borate) (Scheme 1.5A). Notable for this transformation is the breaking of the Fe–B bond. In contrast, Hill reported that the addition of halogens to the platinum analogue, **B(mim^{tBu})$_3$**Pt(PPh$_3$), do not result in Pt−B bond breakage (Scheme 1.5B).[49] Instead, oxidative addition of X$_2$ occurs at the metal center to afford **B(mim^{tBu})$_3$**Pt(X)$_2$ with retention of the Pt−B bond. The first reported

example of H_2 addition across a M–B interaction was from Owen for the rhodaboratrane **B(NIn)$_3$**RhR (B(NIn)$_3$ = *tris*(1H-pyrrolo-2-3-pyridin-1-yl)borane) (Scheme 1.5C).[50] This system is the first example to show that alkyl ligand in a metallaboratranes can be hydrogenated to an alkane. It also shows that the M–B bond can be broken to form a B–H bond in metallaboratranes. However, the reaction is stoichiometric, and catalytic reactivity has not been reported.

Scheme 1.5 Reactivity of metallaboratranes toward X–Y substrates.

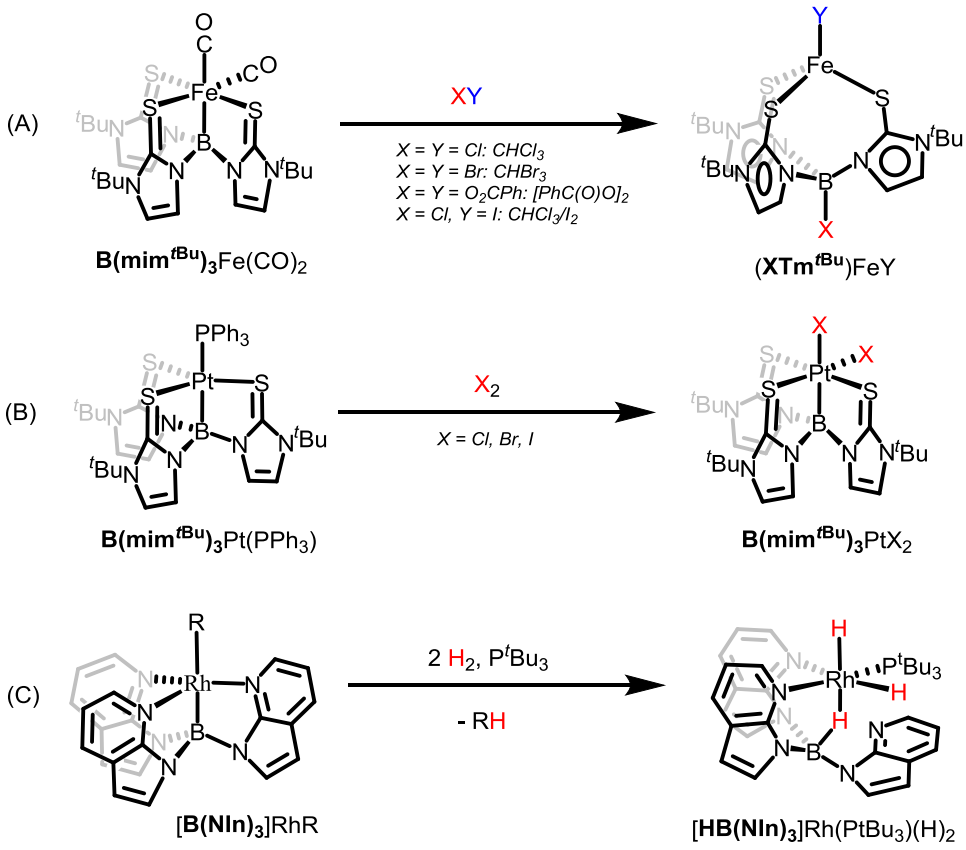

*1.2.2 Background on (**TPB**)MX*

Our group recently began to study the series of metallaboratranes (**TPB**)M[51-56,57] and ($^{\mathbf{R}}$**DPB**$^{\mathbf{Ar}}$)M[39,58,59,60] (^{R}DPB^{Ar} = ArB(*o*-$C_6H_4PR_2)_3$; R = Ph or *i*Pr; Ar = 2,4,6-$(Me)_3$-Ph or Ph; M = Fe, Co, or Ni) (Chart 1.1). At the onset, we were focused on the coordination chemistry of π-acids such as N_2 and CO and π-bases such as imides and nitrides *trans* to the boron in (**TPB**)Fe.[51-52] In light of the limited precedent for bond activation reactivity by metallaboratranes, our group was motivated to study E–H bond activations. The working hypothesis at the time was that the hemi-labile M–B bond in the (**TPB**)MX scaffold may allow the boron and metal center to cleave E–H bonds.

The hemi-lability of the M–B bond in (**TPB**)MX complexes was confirmed experimentally. The Fe–B distance in (**TPB**)FeX extends from the DFT determined value of 2.2 Å in the iron-dinitrogen adduct (**TPB**)Fe(N_2) to 2.589 Å in the iron-imide (**TPB**)Fe(NAr).[51-52] The Fe–B bond in (**TPB**)FeX thus appears to be highly susceptible to the identity of the X ligand and the formal electron count of the $\{M\text{-}B\}^n$ unit[ii] ($\{Fe\text{–}B\}^8$ and $\{Fe\text{–}B\}^6$ for (**TPB**)Fe(N_2) and (**TPB**)Fe(NAr), respectively). Between the isoelectronic (**TPB**)Ni[56] and [(**TPB**)Cu](BAr$^F{}_4$)[55] complexes, the M–B distances are also very different: 2.168 Å in (**TPB**)Ni and 2.495 Å in [(**TPB**)Cu](BAr$^F{}_4$). This pair of complexes shows that the Lewis basicity of the metal, by substitution of Ni^0 for Cu^I, and/or increasing the formal charge of the complex can disrupt the

[ii] The $\{M–E\}^n$ notation refers to the number of valence electrons that are formally assigned to the metal (e.g., Fe) and those shared with E (e.g., B). Since the M–E bond may be covalent and the M–E interaction is dictated in part by the ligand chelate and M–E distance, the bonding electrons between M–E are not reliably assigned to either atom. As such, the $\{M–E\}^n$ notation tracks the number of valence electrons without assignment of valence or oxidation numbers. See ref 61 and 62.

M−B interaction. The M−B bond distances in the (**TPB**)MX complexes are in contrast to the first row metallaboratrane complexes of **B(mim^{tBu})**MX (M = Fe(CO),[48] Co,[63] or Ni;[64-65] L = CO, Cl, OAc, NCS, PPh_3, N_3), where the M–B distances are consistently short (2.0 – 2.1 Å), regardless of the spin state and identity of M. They also contrast with the nearly static Fe−Si distances in the (**SiP$^{iPr}_3$**)MX system,[66-67] where the B in TPB is replaced by a Si atom in SiP^{iPr}_3, that has been extensively studied in our group. The rigid M−Si distance in the (**SiP$^{R}_3$**)MX system reflects the stronger M−Si bond compared to the M−B bond. How this difference in M−E (E = B or Si) bonding affects E−H bond activation and catalysis for the (**TPB**)FeX and (**SiP$^{iPr}_3$**)FeX systems will be discussed in Chapters 2 and 4.

*1.2.3 E–H Bond Activation by (**^{R}DPB^{Ar}**)MX*

The ^{R}DPB^{Ar} (Ar = Ph or Mes, R = ^{i}Pr or Ph) ligand has one less phosphine donor unit compared to the three phosphine donor units on the TPB ligand. (**^{R}DPB^{Ar}**)MX complexes all show η^2-arene or C_{ipso} interactions between the metal and arene unit, as shown in Chart 1.1.[39,60,68] Compared to the M−P bond, the M−arene interaction is more labile. It appears that this lability engenders greater reactivity for (**^{R}DPB^{Ar}**)MX complexes towards E−H bonds.

E−H bond cleavage and catalysis by (**^{Ph}DPB^{Mes}**)Ni were discovered concurrently with the (**TPB**)Fe results presented in Chapter 2. (**^{Ph}DPB^{Mes}**)Ni heterolytically cleaves the E–H bonds of H–H[39] and R_2HSi–H[58] to afford (**^{Ph}DPB^{Mes}**)(μ–H)Ni(E) (E = H or R_2HSi). The system is also competent olefin hydrogenation and ketone hydrosilation, respectively (Scheme 1.6A/B). The cleavage of the H–H bond in H_2 by (**^{Ph}DPB^{Mes}**)Ni is particularly noteworthy because it is the first well-defined example for the oxidative addition of H_2 to a single nickel center. For

comparison, the isoelectronic (**TPB**)Ni does not react with H_2 (Scheme 1.6C),[56] suggesting that lability of one ligand arm is necessary for E–H bond activation in these nickelaboratranes.

Two independent DFT studies support the cooperativity of the borane and nickel for H–H bond cleavage.[59,69] Calculations at the M06L/6-31+G* level for the model ($^{\mathbf{Me}}$**DPB**$^{\mathbf{Ph}}$)Ni system (the phenyls were replaced with methyls on the phosphines, and mesityl was replaced with phenyl) indicate that the lowest energy transition state (28.1 kcal/mol) for H–H bond cleavage involves the formation of a B–H bond in concert with H–H bond cleavage (Figure 1.1A).[59] An alternative mechanism, where B–H bond formation occurs *after* oxidative addition of H_2 at nickel to afford a nickel-dihydride, is 9 kcal/mol higher in energy (Figure 1.1B).

Scheme 1.6 H–H and Si–H bond activation reactions and catalysis by nickelaboratranes.

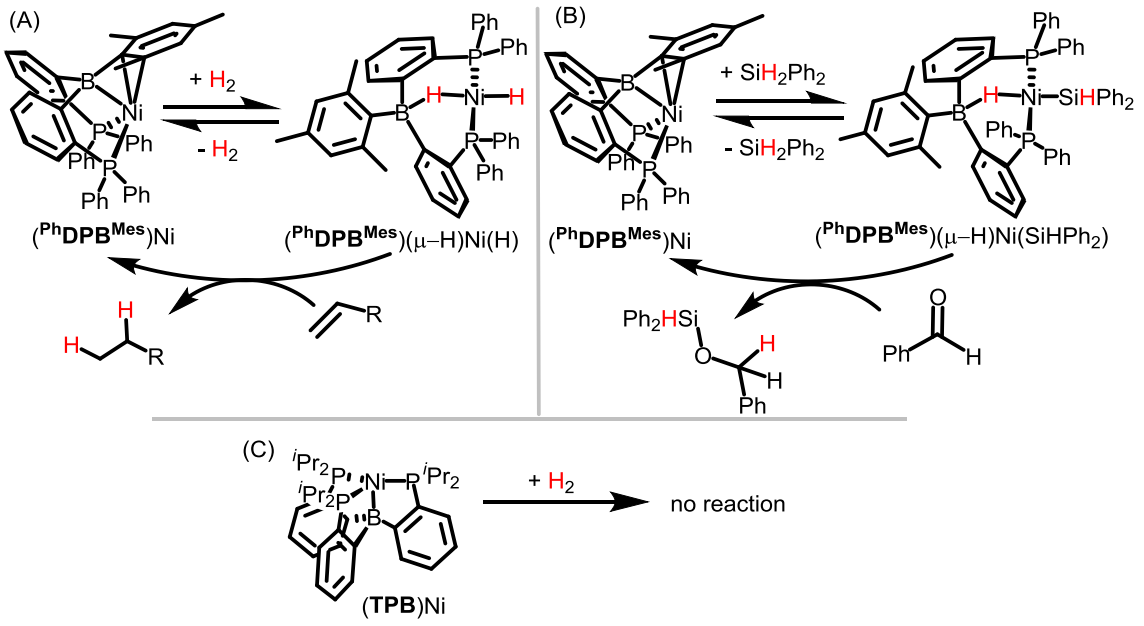

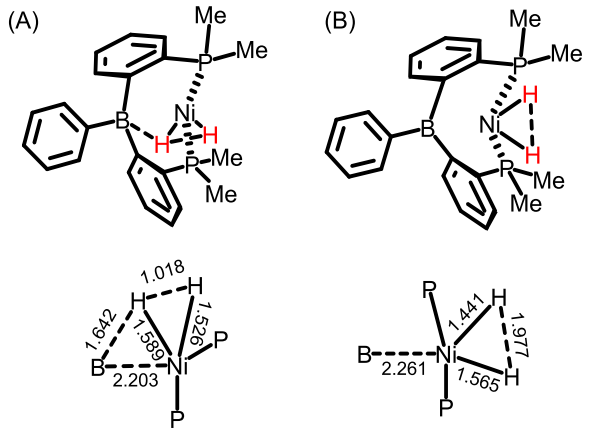

Figure 1.1 DFT calculated transition states for borane assisted and unassisted H–H bond cleavage. Selected bond distances are in Å. (A) Borane assisted H–H cleavage, $\Delta G^{\ddagger}$ = 28.1 kcal/mol. (B) Oxidative addition of H_2 at nickel unassisted by the borane, $\Delta G^{\ddagger}$ = 36.9 kcal/mol.

E–H bond activations by low coordinate iron[70] and cobalt[71] complexes are known in the literature. Iron and cobalt complexes of the ^{R}DPB^{Ar} ligand can also activate various E–H bonds. The C–H bond activation of BZQ (BZQ = benzo[*h*]quinolin-10-yl) by the N_2-bridged iron-dimer [(**^{iPr}DPB^{Ph}**)Fe]$_2$(N_2) affords the six-coordinate iron complex (**^{iPr}DPB^{Ph}**)(μ–H)Fe(BZQ), which features a hydride ligand bridging the boron and iron atoms, as well as an interaction between the iron and ipso carbon atom of the phenyl arm of the ligand (Scheme 1.7A).[72] The cobalt complex (**^{iPr}DPB^{Ph}**)Co(N_2) also activates the C–H bond of BZQ to afford (**^{iPr}DPB^{Ph}**)(μ–H)Co(BZQ).[72] In contrast to the iron-analogue, the cobalt-BZQ complex is pseudo-square pyramidal and does not have a Co–C_{ipso} interaction (Scheme 1.7B). It is thought that the pyridine group directs the C–H group towards the metal center to facilitate bond activation.

Scheme 1.7 C–H bond activation by [(***i*Pr**DPB**Ph**)Fe]$_2$(N_2) and (***i*Pr**DPB**Ph**)Co(N_2).

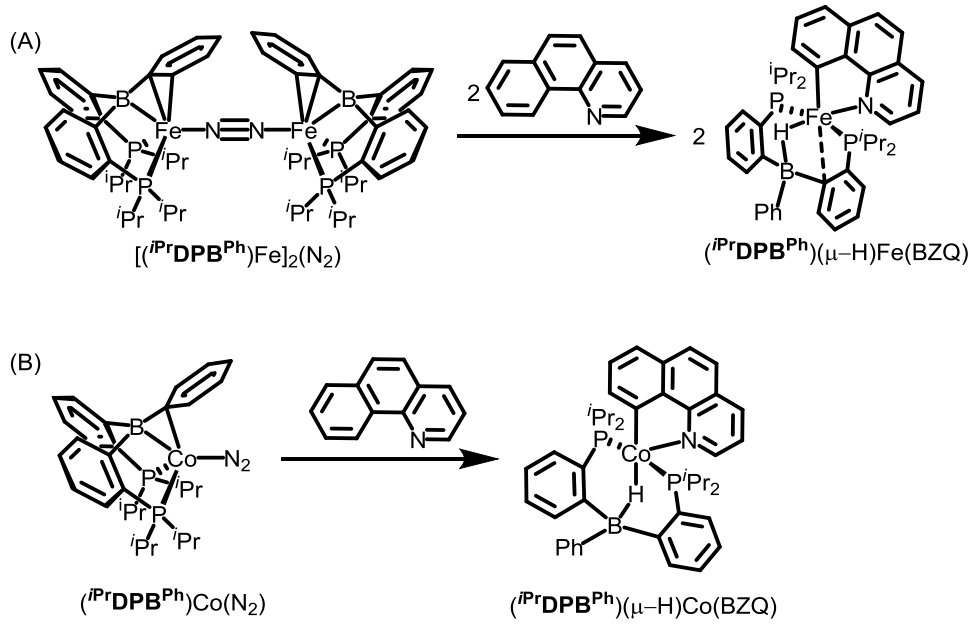

Scheme 1.8 Reactivity of [(***i*Pr**DPB**Ph**)Fe]$_2$(N_2) and (***i*Pr**DPB**Ph**)Co(N_2) towards PhOH.

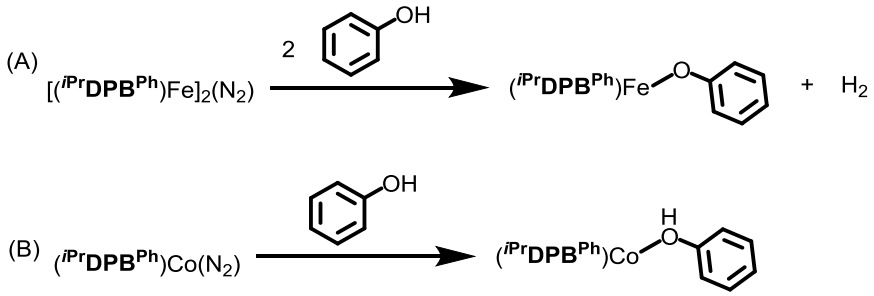

E–H bond activation by [(***i*Pr**DPB**Ph**)Fe]$_2$(N_2) and (***i*Pr**DPB**Ph**)Co(N_2) also extends to benzylic C–H and N–H bonds, as well as P–H, O–H, and S–H bonds.[72] Differences in their reactivity towards various E–H bonds exist. One difference between the two systems is their reactivity

towards phenol. [(*i*Pr**DPB**Ph)Fe]$_2$(N_2) reacts with 2 equiv of phenol to afford the iron-phenolate product (*i*Pr**DPB**Ph)Fe(OPh) and 1 equiv of H_2 (Scheme 1.8A). A B–H linkage is not present in (*i*Pr**DPB**Ph)Fe(OPh). For (*i*Pr**DPB**Ph)Co(N_2), O–H activation does not occur, and phenol ligates through the O-atom as phenol-adduct to cobalt to give (*i*Pr**DPB**Ph)Co(O(H)Ph) (Scheme 1.8B).

The activation of E–H bonds has also been coupled to other bond-forming and bond-breaking transformations. The reaction of $PhSiH_3$ with the aminoimide (Ph**DPB**Ph)Fe(NN(SiR_3)$_2$) results in the hydrosilation of the Fe–N bond with delivery of the PhH_2Si group to the α-nitrogen of the imide and H to the boron atom, affording the iron-hydrazido^{1-} species **S** (Scheme 1.9).[68] The reaction of H_2 with (Ph**DPB**Ph)Fe(NN(SiR_3)$_2$) results in H–H bond cleavage, formation of B–H and N–H linkages, and rupture of the N–N bond to afford **T** (Scheme 1.9).[68]

Scheme 1.9 Hydrogenation and hydrosilation of an iron-aminoimide.

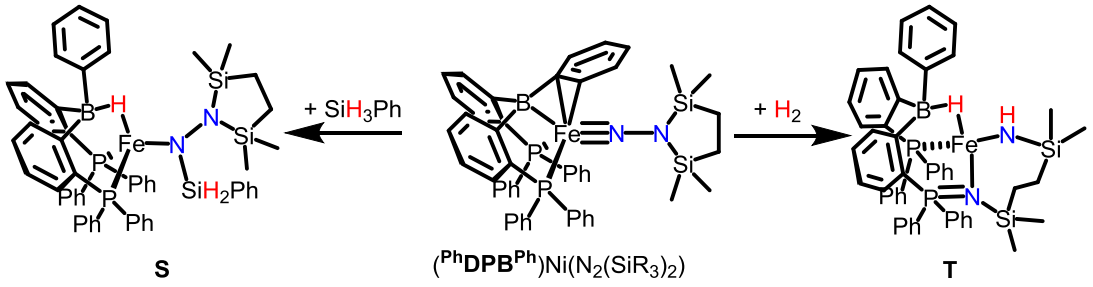

The reaction of H_2 with the iron-dicarbyne species (*i*Pr**DPB**Ph)Fe(COTMS)$_2$ (TMS = $(CH_3)_3Si$) results in the reductive C–C bond coupling and C–H bond formation to afford the CO derived disiloxyethylene product (Scheme 1.10).[60] The identity of iron containing product from this reaction is not known. Previous examples of reductive CO coupling by iron

complexes are rare, and the release of an olefin from hydrogenative CO reductive coupling is not known for iron.

Scheme 1.10 C–C coupling and C–H coupling of an iron-dicarbyne.

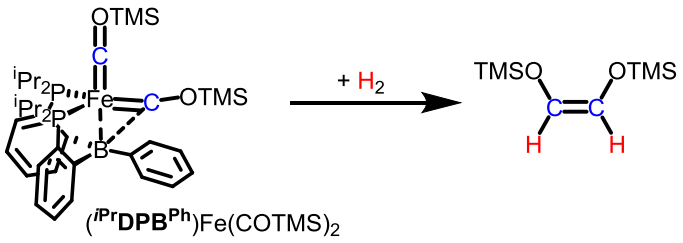

In summary, the ^{R}DPB^{Ar} ligand engenders unusual bond breaking and bond forming transformations, as well as catalytic reactivity, that are otherwise rarely observed or unknown for iron, cobalt, and nickel complexes. The reactivity is facilitated in part by cooperativity between the Lewis acidic borane and Lewis basic metal center, as well as the lability of the aryl unit of ligand. The latter point is notable because differences in hydrogenation catalysis and E–H bond activation are observed between related (**TPB**)MX and (**^{R}DPB^{Ar}**)MX complexes.

1.4 Cited References

(1) Hartwig, J. F. *Organotransition Metal Chemistry: From Bonding to Catalysis*; 1st ed.; University Science Books: Sausalito, California, 2010.

(2) Young, J. F.; Osborn, J. A.; Jardine, F. H.; Wilkinson, G. *Chemical Communications (London)* **1965**, 131-132.

(3) Osborn, J. A.; Jardine, F. H.; Young, J. F.; Wilkinson, G. *J. Chem. Soc. A* **1966**, 1711-1732.

(4) James, B. R. *Homogeneous Hydrogenation*; Wiley: New York, 1973.

(5) Halpern, J.; Wong, C. S. *J. Chem. Soc., Chem. Commun.* **1973**, 629-630.

(6) Halpern, J.; Okamoto, T.; Zakhariev, A. *J. Mol. Catal.* **1977**, *2*, 65-68.

(7) In *The Handbook of Homogeneous Hydrogenation*; Wiley-VCH Verlag GmbH: 2008.

(8) Hallman, P. S.; McGarvey, B. R.; Wilkinson, G. *J. Chem. Soc. A* **1968**, 3143-3150.

(9) James, B. R.; Wang, D. K. W. *J. Chem. Soc., Chem. Commun.* **1977**, 550-551.

(10) Alibrandi, G.; Mann, B. E. *J. Chem. Soc., Dalton Trans.* **1994**, 951-954.

(11) Stolzenberg, A. M.; Muetterties, E. L. *Organometallics* **1985**, *4*, 1739-1742.

(12) Sweany, R. L.; Halpern, J. *J. Am. Chem. Soc.* **1977**, *99*, 8335-8337.

(13) Bullock, R. M. *Chem. Eur. J.* **2004**, *10*, 2366-2374.

(14) Perutz, R. N.; Sabo-Etienne, S. *Angew. Chem. Int. Ed.* **2007**, *46*, 2578-2592.

(15) Bullock, R. M. *Catalysis without Precious Metals*; Wiley-VCH Verlag GmbH & Co. KGaA: Weinheim, Germany, 2010.

(16) Bart, S. C.; Lobkovsky, E.; Chirik, P. J. *J. Am. Chem. Soc.* **2004**, *126*, 13794-13807.

(17) Archer, A. M.; Bouwkamp, M. W.; Cortez, M.-P.; Lobkovsky, E.; Chirik, P. J. *Organometallics* **2006**, *25*, 4269-4278.

(18) Bart, S. C.; Hawrelak, E. J.; Lobkovsky, E.; Chirik, P. J. *Organometallics* **2005**, *24*, 5518-5527.

(19) Trovitch, R. J.; Lobkovsky, E.; Chirik, P. J. *Inorg. Chem.* **2006**, *45*, 7252-7260.

(20) Casey, C. P.; Guan, H. *J. Am. Chem. Soc.* **2007**, *129*, 5816-5817.

(21) Sui-Seng, C.; Freutel, F.; Lough, A. J.; Morris, R. H. *Angew. Chem. Int. Ed.* **2008**, *47*, 940-943.

(22) Nishiyama, H.; Furuta, A. *Chem. Commun.* **2007**, 760-762.

(23) Langer, R.; Leitus, G.; Ben-David, Y.; Milstein, D. *Angew. Chem. Int. Ed.* **2011**, *50*, 2120-2124.

(24) Bornschein, C.; Werkmeister, S.; Wendt, B.; Jiao, H.; Alberico, E.; Baumann, W.; Junge, H.; Junge, K.; Beller, M. *Nat Commun* **2014**, *5*.

(25) Gärtner, D.; Welther, A.; Rad, B. R.; Wolf, R.; Jacobi von Wangelin, A. *Angew. Chem. Int. Ed.* **2014**, *53*, 3722-3726.

(26) Chakraborty, S.; Dai, H.; Bhattacharya, P.; Fairweather, N. T.; Gibson, M. S.; Krause, J. A.; Guan, H. *J. Am. Chem. Soc.* **2014**, *136*, 7869-7872.

(27) Knijnenburg, Q.; Horton, A. D.; Heijden, H. v. d.; Kooistra, T. M.; Hetterscheid, D. G. H.; Smits, J. M. M.; Bruin, B. d.; Budzelaar, P. H. M.; Gal, A. W. *J. Mol. Catal. A: Chem.* **2005**, *232*, 151-159.

(28) Monfette, S.; Turner, Z. R.; Semproni, S. P.; Chirik, P. J. *J. Am. Chem. Soc.* **2012**, *134*, 4561-4564.

(29) Zhang, G.; Scott, B. L.; Hanson, S. K. *Angew. Chem. Int. Ed.* **2012**, *51*, 12102-12106.

(30) Lin, T.-P.; Peters, J. C. *J. Am. Chem. Soc.* **2013**, *135*, 15310-15313.

(31) Yu, R. P.; Darmon, J. M.; Milsmann, C.; Margulieux, G. W.; Stieber, S. C. E.; DeBeer, S.; Chirik, P. J. *J. Am. Chem. Soc.* **2013**, *135*, 13168-13184.

(32) Camacho-Bunquin, J.; Ferguson, M. J.; Stryker, J. M. *J. Am. Chem. Soc.* **2013**, *135*, 5537-5540.

(33) Zhang, G.; Vasudevan, K. V.; Scott, B. L.; Hanson, S. K. *J. Am. Chem. Soc.* **2013**, *135*, 8668-8681.

(34) Lin, T.-P.; Peters, J. C. *J. Am. Chem. Soc.* **2014**, *136*, 13672-13683.

(35) Angulo, I. M.; M. Kluwer, A.; Bouwman, E. *Chem. Commun.* **1998**, 2689-2690.

(36) Angulo, I. M.; Bouwman, E. *J. Mol. Catal. A: Chem.* **2001**, *175*, 65-72.

(37) Vasudevan, K. V.; Scott, B. L.; Hanson, S. K. *Eur. J. Inorg. Chem.* **2012**, *2012*, 4898-4906.

(38) Wu, J.; Faller, J. W.; Hazari, N.; Schmeier, T. J. *Organometallics* **2012**, *31*, 806-809.

(39) Harman, W. H.; Peters, J. C. *J. Am. Chem. Soc.* **2012**, *134*, 5080-5082.

(40) Bart, S. C.; Chłopek, K.; Bill, E.; Bouwkamp, M. W.; Lobkovsky, E.; Neese, F.; Wieghardt, K.; Chirik, P. J. *J. Am. Chem. Soc.* **2006**, *128*, 13901-13912.

(41) Noyori, R.; Yamakawa, M.; Hashiguchi, S. *J. Org. Chem.* **2001**, *66*, 7931-7944.

(42) Schwartsburd, L.; Iron, M. A.; Konstantinovski, L.; Diskin-Posner, Y.; Leitus, G.; Shimon, L. J. W.; Milstein, D. *Organometallics* **2010**, *29*, 3817-3827.

(43) Hill, A. F.; Owen, G. R.; White, A. J. P.; Williams, D. J. *Angew. Chem. Int. Ed.* **1999**, *38*, 2759-2761.

(44) Verkade, J. G. *Acc. Chem. Res.* **1993**, *26*, 483-489.

(45) Voronkov, M. G.; Dyakov, V. M.; Kirpichenko, S. V. *J. Organomet. Chem.* **1982**, *233*, 1-147.

(46) Kubas, G. J. *Chem. Rev.* **2007**, *107*, 4152-4205.

(47) Stephan, D. W.; Erker, G. *Angew. Chem. Int. Ed.* **2010**, *49*, 46-76.

(48) Figueroa, J. S.; Melnick, J. G.; Parkin, G. *Inorg. Chem.* **2006**, *45*, 7056-7058.

(49) Crossley, I. R.; Hill, A. F.; Willis, A. C. *Organometallics* **2008**, *27*, 312-315.

(50) Tsoureas, N.; Owen, G. R.; Hamilton, A.; Orpen, A. G. *Dalton Trans.* **2008**, 6039-6044.

(51) Moret, M.-E.; Peters, J. C. *Angew. Chem. Int. Ed.* **2011**, *50*, 2063-2067.

(52) Moret, M.-E.; Peters, J. C. *J. Am. Chem. Soc.* **2011**, *133*, 18118-18121.

(53) Anderson, J. S.; Moret, M.-E.; Peters, J. C. *J. Am. Chem. Soc.* **2012**, *135*, 534-537.

(54) Anderson, J. S.; Rittle, J.; Peters, J. C. *Nature* **2013**, *501*, 84-87.

(55) Moret, M.-E.; Zhang, L.; Peters, J. C. *J. Am. Chem. Soc.* **2013**, *135*, 3792-3795.

(56) Tsay, C.; Peters, J. C. *Chem. Sci.* **2012**, *3*, 1313-1318.

(57) Suess, D. L. M.; Tsay, C.; Peters, J. C. *J. Am. Chem. Soc.* **2012**, *134*, 14158-14164.

(58) MacMillan, S. N.; Hill Harman, W.; Peters, J. C. *Chem. Sci.* **2014**, *5*, 590-597.

(59) Harman, W. H.; Lin, T.-P.; Peters, J. C. *Angew. Chem. Int. Ed.* **2014**, *53*, 1081-1086.

(60) Suess, D. L. M.; Peters, J. C. *J. Am. Chem. Soc.* **2013**, *135*, 12580-12583.

(61) Hill, A. F. *Organometallics* **2006**, *25*, 4741-4743.

(62) Parkin, G. *Organometallics* **2006**, *25*, 4744-4747.

(63) Mihalcik, D. J.; White, J. L.; Tanski, J. M.; Zakharov, L. N.; Yap, G. P. A.; Incarvito, C. D.; Rheingold, A. L.; Rabinovich, D. *Dalton Trans.* **2004**, 1626-1634.

(64) Senda, S.; Ohki, Y.; Hirayama, T.; Toda, D.; Chen, J.-L.; Matsumoto, T.; Kawaguchi, H.; Tatsumi, K. *Inorg. Chem.* **2006**, *45*, 9914-9925.

(65) Pang, K.; Tanski, J. M.; Parkin, G. *Chem. Commun.* **2008**, 1008-1010.

(66) Lee, Y.; Mankad, N. P.; Peters, J. C. *Nature Chem.* **2010**, *2*, 558-565.

(67) Whited, M. T.; Mankad, N. P.; Lee, Y.; Oblad, P. F.; Peters, J. C. *Inorg. Chem.* **2009**, *48*, 2507-2517.

(68) Suess, D. L. M.; Peters, J. C. *J. Am. Chem. Soc.* **2013**, *135*, 4938-4941.

(69) Zeng, G.; Sakaki, S. *Inorg. Chem.* **2013**, *52*, 2844-2853.

(70) Selected examples of C–H activation by iron complexes: (a) Klein, H.-F.; Camadanli, S.; Beck, R.; Leukel, D.; Flörke, U. *Angew. Chem. Int. Ed.* **2005,** *44*, 975-977; (b) Baker, M. V.; Field, L. D. *J. Am. Chem. Soc.* **1986,** *108*, 7433-7434; (c) Field, L. D.; Guest, R. W.; Turner, P. *Inorg. Chem.* **2010,** *49*, 9086-9093; (d) Pan, Y. H.; Sohlberg, K.; Ridge, D. P. *J. Am. Chem. Soc.* **1991, 113,** 2406-2411; (e) Bolig, A. D.; Brookhart, M. *J. Am. Chem. Soc.* **2007,** *129*, 14544-14545. (f) (e) Wang, D.; Farquhar, E. R.; Stubna, A.; Muenk, E.; Que, L. *Nature Chem.* **2009,** *1*, 145-150.

(71) Selected examples C–H activation by cobalt complexes: (a) Klein, H.-F.; Camadanli, S.; Beck, R.; Leukel, D.; Flörke, U. *Angew. Chem. Int. Ed.* **2005,** *44*, 975-977; (b) Yoshino, T.; Ikemoto, H.; Matsunaga, S.; Kanai, M. *Angew. Chem. Int. Ed.* **2013**, 52, 2207-2211; (c) Ding, Z.; Yoshikai, N. Beilstein *J. Org. Chem.* **2012**, 8, 1536-1542; (d) Zhang, R.; Zhu, L.; Liu, G.; Dai, H.; Lu, Z.; Zhao, J.; Yan, H. *J. Am. Chem. Soc.* **2012,** 134, 10341-10344; (e) Lee, P.-S.; Fujita, T.; Yoshikai, N. *J. Am. Chem. Soc.* **2011,** 133, 17283-17295; (f) Chen, Q.; Ilies, L.; Nakamura, E. *J. Am. Chem. Soc.* **2010,** 133, 428-429; (g) Hojilla Atienza, C. C.; Bowman, A. C.; Lobkovsky, E.; Chirik, P. J. *J. Am. Chem. Soc.* **2010,** *132,* 16343-16345; (h) Aubert, C.; Betschmann, P.; Eichberg, M. J.; Gandon, V.; Heckrodt, T. J.; Lehmann, J.; Malacria, M.; Masjost, B.; Paredes, E.; Vollhardt, K. P. C.; Whitener, G. D. *Chem. Eur. J.* **2007**, *13,* 7443-7465. (i) Li, L.; Jones, W. D. *J. Am. Chem. Soc.* **2007,** *129,* 10707-10713.

(72) Unpublished results.

Chapter 2. Heterolytic H_2 Cleavage and Catalytic Hydrogenation by an Iron Metallaboratrane

Reproduced in part with permission from:
Fong, H.; Moret, M.-E.; Lee, Y.; Peters, J. C. *Organometallics* **2013,** *32,* 3053-3062.

2.1 Preface

This chapter describes the heterolytic cleavage of H–H and C–H bonds by the ferraboratrane (**TPB**)Fe(L) (L = N_2, CO, ^{t}BuNC), as well as catalytic olefin and arylacetylene hydrogenation by (**TPB**)Fe(N_2). The data show that (**TPB**)Fe(N_2) reversibly cleaves H_2 to afford (**TPB**)(μ–H)Fe(L)(H), which contains B–H and Fe–H linkages. The bond cleavage reaction contrasts with the H_2 chemistry of the related silatrane (**SiP$^{iPr}_3$**)Fe scaffold, as well as the cobaltaboratrane (**TPB**)Co(H_2) (see Chapter 3). (**TPB**)(μ–H)Fe(L)(H) (L = N_2 or H_2) and (**TPB**)Fe(N_2) are competent hydrogenation catalysts, and stoichiometric studies indicate that the B–H unit in (**TPB**)(μ–H)Fe(L)(H) is capable of H^- transfer to the olefin substrate. These findings are presented in the context of metal-borane cooperative bond activation and catalysis.

I am the first author of an article published in *Organometallics* that describes this work. The other authors of this paper are Marc-Etienne Moret, Yunho Lee, and Jonas Peters. I performed all of the experiments for the (**TPB**)Fe system described in this chapter. Marc-Etienne, Jonas Peters, and I analyzed the results. Marc-Etienne Moret also assisted me with DFT calculations. Yunho Lee worked on the H_2 chemistry of the (**SiP$^{iPr}_3$**)FeX system.

2.2 Introduction

Transition metal-catalyzed bond forming reactions often involve formal two-electron redox steps (e.g., oxidative addition and reductive elimination). Noble metal catalysts are commonly used in these reactions due, in part, to their propensity to facilitate multi-electron processes.[1] There is growing interest in developing catalysts for bond forming/cleavage reactions based on earth abundant mid-to-late first-row transition metals, a goal that presents a unique set of challenges.[2] First-row transition metal catalysts that can circumvent undesirable one electron processes in favor of concerted two electron reaction steps present one plausible design criterion.[3]

Cooperative catalysis strategies that utilize ligands that operate in tandem with a coordinated metal center to activate substrates have shown promise in addressing this issue. [4-9] First-row metallaboratranes and related compounds that contain a retrodative M→B σ-interaction[10] are appealing as catalysts[11-12] because of the boron center's ability to stabilize low valent metals.[13-19] Akin to frustrated Lewis pairs,[20] it has also been recently demonstrated that the metal-boron interaction can cooperatively facilitate the activation of H_2.[11,21] For instance, our lab reported that the diphosphine-borane nickel (^{Mes}**DPB**^{Ph})Ni complex (^{Mes}**DPB**^{Ph} = MesB(*o*-$C_6H_4PPh_2)_2$) undergoes reversible oxidative addition of H_2 to afford a nickel-borohydrido-hydride complex (Scheme 2.1).[22] This nickel system is an efficient catalyst for olefin hydrogenation. Kameo and Nakazawa have also reported on the transfer hydrogenation of ketones catalyzed by a related rhodium diphosphine-borane complex.[23]

Scheme 2.1. Related H_2 activation across a Ni–B bond.

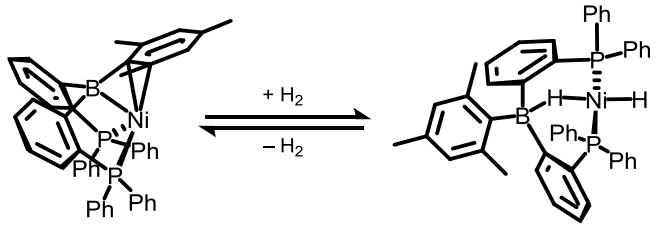

This chapter describes studies on heterolytic H–H bond cleavage at a ferraboratrane complex[24-25] of a triphosphine-borane (TPB) ligand (TPB = B(*o*-$C_6H_4P^iPr_2)_3$).[26] Dihydrogen is shown to add reversibly across the Fe–B bond of (**TPB**)Fe(L) complexes to form corresponding iron-borohydrido-hydride complexes of the type (**TPB**)(μ–H)Fe(L)(H). Like the nickel system reported previously, olefin hydrogenation catalysis is accessible, albeit much slower, thereby facilitating detailed studies. As discussed below, other E–H bonds are also activated by the ferraboratanes described, including the terminal C–H bonds of arylacetylenes and the C–H bonds of formaldehyde.

2.3 Results and Discussion

2.3.1 Reversible H_2 Addition

Exposing the previously reported (**TPB**)Fe(N_2) complex[24] in d_6-benzene to H_2 (1.2 equiv) at room temperature results in H_2 addition across the Fe–B bond to give a yellow solution of the six coordinate borohydride-hydride-N_2 complex (**TPB**)(μ–H)Fe(N_2)(H) (Scheme 2.2). The

XRD structure of (**TPB**)(μ–H)Fe(N_2)(H) shows that the Fe–B distance is significantly elongated relative to (**TPB**)Fe(N_2) (2.604(3) Å in (**TPB**)(μ–H)Fe(N_2)(H) (Figure 2.1) versus the calculated distance of 2.2 Å in (**TPB**)Fe(N_2)[25]. A terminal hydride ligand and a bridging hydride ligand located between the B and Fe atoms can be assigned from the electron density

Scheme 2.2 H−H and E−H bond activations across Fe−B bonds.

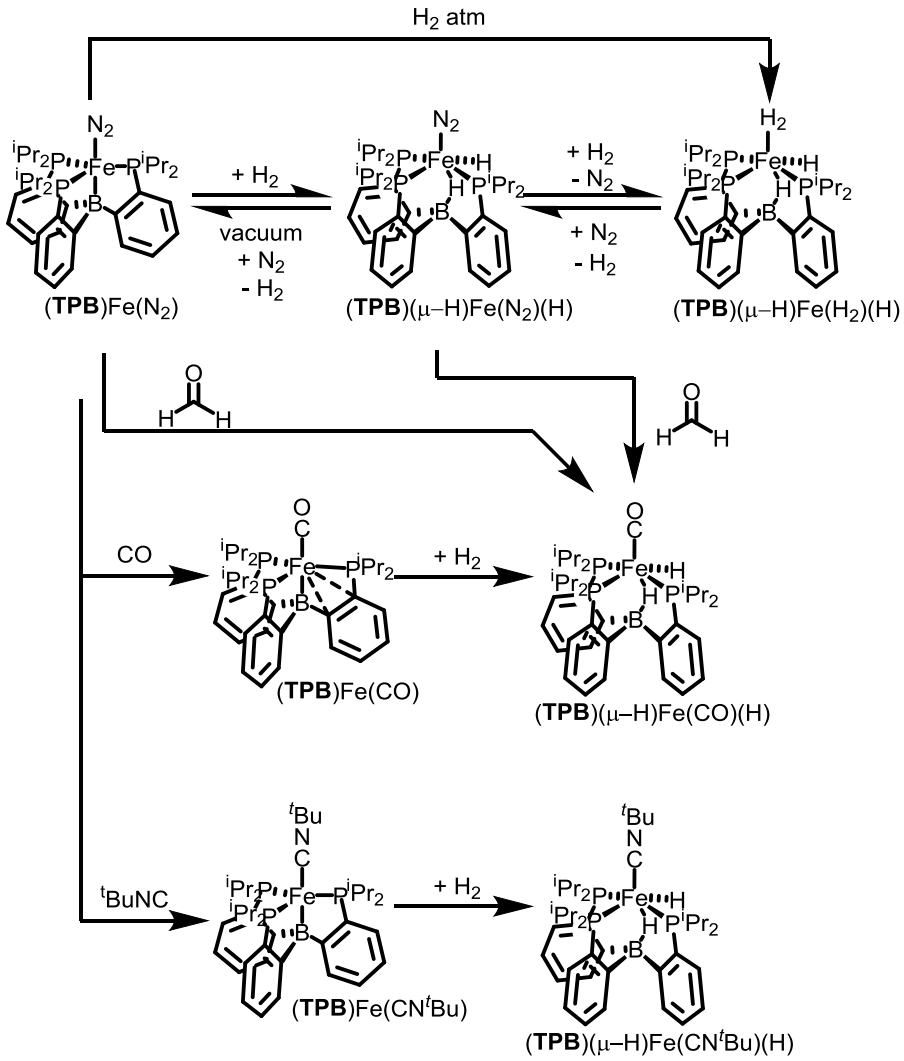

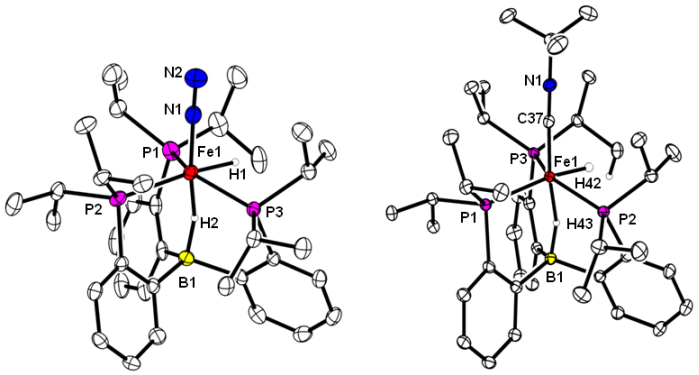

Figure 2.1 XRD structures of (**TPB**)(μ–H)Fe(N_2)(H) and (**TPB**)(μ–H)Fe(CN^tBu)(H). Ellipsoids shown at 50% probability. Selected bond distances (Å): (left) (**TPB**)(μ–H)Fe(N_2)(H), Fe1–H1 = 1.42(2), Fe1–H2 = 1.49(2), B1–H2 = 1.17(2), Fe1–B1 = 2.604(3); (right) (**TPB**)(μ–H)Fe(CN^tBu)(H), Fe1–H42 = 1.35(2), Fe1–H43 = 1.52(2), B1–H43 = 1.20(2), Fe1–B1 = 2.673(2).

difference map. This structure also prevails in solution. In the ^{1}H NMR spectrum (d_6-benzene), the terminal hydride ligand on iron is observed as a triplet-of-doublets at -9.6 ppm, and the bridging hydride is observed as a broad singlet at -30.4 ppm. Replacing H_2 with D_2 in the reaction gives the corresponding isotopologue (**TPB**)(μ–D)Fe(N_2)(D). Along with the expected deuteride signals in the ^{2}H NMR spectrum, deuterium signals from the methine and terminal methyl positions of the isopropyl groups of the TPB ligand are observed. This observation establishes that facile scrambling of the hydridic ligands into the TPB isopropyl groups occurs, presumably via a reversible C–H metalation process. The dinitrogen ligand (ν_{NN} = 2070 cm^{-1}) in (**TPB**)(μ–H)Fe(N_2)(H) is labile, and it can be substituted under excess H_2 to give the dihydrogen analogue (**TPB**)(μ–H)Fe(H_2)(H) (Scheme 2.2). Exposing (**TPB**)Fe(N_2) to excess H_2 (1 atm) also generates (**TPB**)(μ–H)Fe(H_2)(H). Its XRD structure again confirms

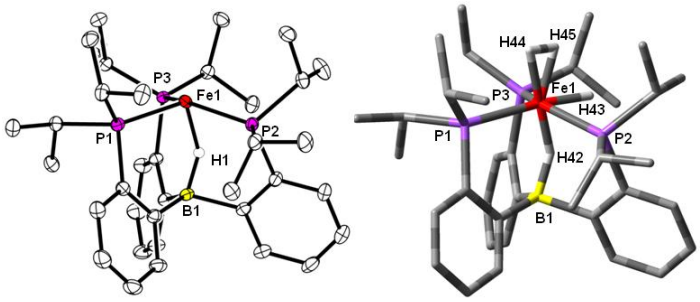

Figure 2.2 XRD and DFT optimized structures of (**TPB**)(μ–H)Fe(H_2)(H). Ellipsoids shown at 50% probability. Selected bond distances (Å) and angles (°): (left) XRD, Fe1–H42 = 1.56(2), B1–H42 = 1.21(2), Fe1–B1, 2.63(2), P2–Fe–P3 = 136.54(2); (right) DFT predicted, Fe1–H42 = 1.51, Fe1–H43 = 1.50, Fe1–H44 = 1.62, Fe1–H45 = 1.59, B1–H42 = 1.24, Fe1–B1 = 2.63, H44–H45 = 0.84, P2–Fe1–P3 = 140.63.

the presence of a bridging hydride (Figure 2.2). Although electron density can be located in the difference map between a widened P–Fe–P angle (136.54(2)°) and in the apical position *trans* to the borohydride unit, the data do not allow us to reliably distinguish between classical and non-classical hydrides. We therefore turned to NMR spectroscopy to aid in the formulation of (**TPB**)(μ–H)Fe(H_2)(H).

The 20 °C ^{1}H NMR spectrum (d_8-toluene) of (**TPB**)(μ–H)Fe(H_2)(H) (Figure 2.3) shows a broad singlet resonance at -15.1 ppm, indicative of hydridic protons. A broad deuteride signal is observed in the ^{2}H NMR spectrum when D_2 is used in place of H_2, and, like in (**TPB**)(μ–H)Fe(N_2)(H), deuterium signals are also observed in the methyl and methine positions of the isopropyl groups of the TPB ligand. Cooling a d_8-toluene solution of (**TPB**)(μ–H)Fe(H_2)(H) under an H_2 atmosphere to -20 °C leads to sharpening of the resonance at -15.1 ppm, which integrates to three protons (3H). A second, broad hydridic resonance integrating to one proton

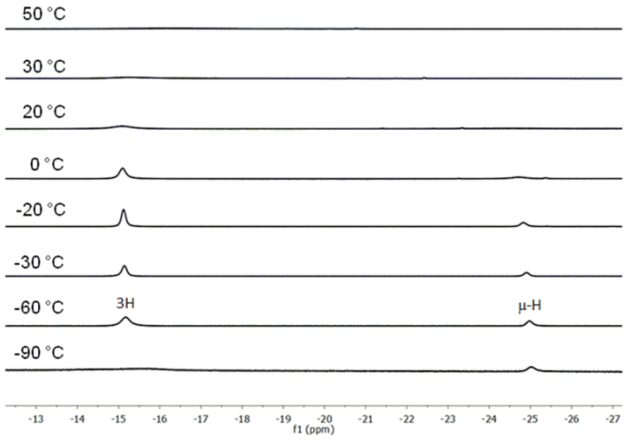

Figure 2.3 ^{1}H VT-NMR spectra of (**TPB**)(μ–H)Fe(H_2)(H) in d_8-toluene under 1 atm of H_2.

is also observed at -24.9 ppm, and in analogy to (**TPB**)(μ–H)Fe(N_2)(H), this resonance is assigned to the bridging-borohydride (μ–H). Cooling the temperature down to -90 °C leads to broadening of the 3H resonance without reaching decoalescence, suggesting that exchange of three hydrogenic ligands is fast on the NMR timescale. Compound (**TPB**)(μ–H)Fe(H_2)(H) can be heated to 50 °C before significant sample decomposition is observed (*vide infra*). At 50 °C, the 3H and μ–H signals both broaden into the baseline, suggesting that exchange of all four hydrogens is facile at this temperature.

To further assign the 3H unit in (**TPB**)(μ–H)Fe(H_2)(H) (i.e., dihydrogen-hydride versus trihydride), we turned to minimal longitudinal relaxation (T_{1min}) measurements.[i,27-29] The T_{1min} is 35 ms at -32 °C for the 3H resonance, which suggests that the 3H unit is best described as

[i] The H–D coupling constant (J_{H-D}) is also in principle an excellent distinguishing characteristic between the η^2-dihydrogen and dihydride ligands. Unfortunately, H–D coupling cannot be resolved in (**TPB**)(μ–H)Fe(H_2)(H), likely due to fast exchange within the H_nD_{3-n} unit and H/D scrambling into the methine and terminal methyl positons on the isopropyl groups of the TPB ligand.

dihydrogen-hydride. This interpretation is additionally supported by DFT calculations (RB3LYP/6-31G(d)) that identify a dihydrogen-hydride structure (Figure 2.2 and Appendix 1) as the lowest energy isomer of (**TPB**)(μ–H)Fe(H_2)(H). A stereoisomer in which the H_2 ligand occupies the equatorial position and the hydride ligand is in the axial position *trans* to boron is calculated to be 6.1 kcal/mol higher in energy. This geometric preference parallels that of the well-characterized iron-dihydrogen-dihydride complex *mer*-Fe(H_2)($H)_2$($PEt_2Ph)_3$.[30] The transition state for conversion of (**TPB**)(μ–H)Fe(H_2)(H) into this higher energy stereoisomer involving H–H scission is calculated to be 6.7 kcal/mol above the most stable isomer and is in line with the observed exchange behavior on the NMR timescale.

Analogous (**TPB**)(μ–H)Fe(L)(H) complexes (L = CN^tBu or CO) can be synthesized (Scheme 2.2, Figure 2.1). To explore the effect of the apical ligand L on the H–H bond activation process, (**TPB**)Fe(L) complexes were prepared. The previously reported carbonyl complex (**TPB**)Fe(CO) displays an η^3-interaction with a P–C_{Ar}–C_{Ar} unit of the TPB ligand,[24] whereas isocyanide adduct (**TPB**)Fe(CN^tBu), whose structure has been determined, does not: its Fe center is rigorously 5-coordinate. Complex (**TPB**)Fe(CO) is diamagnetic, whereas (**TPB**)Fe(CN^tBu) gives rise to a solution magnetic susceptibility (μ_{eff} = 1.7 μ_B) at room temperature in C_6D_6. The temperature dependence of the solution susceptibility suggests an S = 0 ground state with a thermally accessible S = 1 state. No reaction occurs between (**TPB**)Fe(CN^tBu) or the previously reported (**TPB**)Fe(CO) with H_2 (1 atm) at room temperature over a period hours. Compound (**TPB**)Fe(CN^tBu) is fully consumed by H_2 (1 atm) over the course of 3 days at 40 °C to generate (**TPB**)(μ–H)Fe(CN^tBu)(H), while compound

(**TPB**)Fe(CO) is fully consumed by H_2 (1 atm) over the course of 5 days at 80 °C to give (**TPB**)(μ–H)Fe(CO)(H). The increase in temperature and reaction time compared to the facile room temperature reaction between (**TPB**)Fe(N_2) and H_2 is consistent with a scenario in which H_2 substitution for L occurs prior to H_2 addition across the Fe–B bond. Complex (**TPB**)(μ–H)Fe(CO)(H) can be alternatively synthesized from (**TPB**)Fe(N_2) or (**TPB**)(μ–H)Fe(N_2)(H) and formaldehyde (Scheme 2.2).

Dihydrogen addition across the Fe–B bond of (**TPB**)Fe(N_2) is reversible. Conversion of (**TPB**)(μ–H)Fe(H_2)(H) to (**TPB**)(μ–H)Fe(N_2)(H) and subsequently back to (**TPB**)Fe(N_2) can be effected by exposing (**TPB**)(μ–H)Fe(H_2)(H) to dynamic vacuum and then N_2, or by repeated freeze-pump-thaw-N_2 cycles. Reformation of the Fe–B bond can also occur through hydride transfer to unsaturated substrates (*vide infra*). Dihydrogen elimination from (**TPB**)(μ–H)Fe(CN^{t}Bu)(H) and (**TPB**)(μ–H)Fe(CO)(H) does not occur when treated similarly.

Worth underscoring is that cleavage of the Fe–B bond in the present ferraboratrane system is distinct from the H_2 chemistry observed for a structurally related (**SiP$^{iPr}_3$**)Fe silatrane system (SiP$^{iPr}_3$ = [Si(*o*-$C_6H_4P^iPr_2)_3$]$^-$,) we have introduced elsewhere.[31-32] For instance, the reaction between (**SiP$^{iPr}_3$**)Fe(N_2) and H_2 affords (**SiP$^{iPr}_3$**)Fe(H_2), and that between [(**SiP$^{iPr}_3$**)Fe(N_2)]$^+$ and H_2 affords [(**SiP$^{iPr}_3$**)Fe(H_2)]$^+$. No disruption of the Fe–Si bond is observed in either case, even if for instance isolated [(**SiP$^{iPr}_3$**)Fe(N_2)]$^+$ or [(**SiP$^{iPr}_3$**)Fe(H_2)]$^+$ is exposed to excess H_2. Ligand substitution instead occurs. This sharply contrasts isoelectronic (**TPB**)Fe(N_2), where H_2 addition readily affords the cleavage product (**TPB**)(μ–H)Fe(N_2)(H) or (**TPB**)(μ–H)Fe(H_2)(H). We also find (this report, Scheme 2.3) that hydrogenolysis of the iron(II) methyl complex

(**SiP**$^{\mathbf{iPr}}_{\mathbf{3}}$)Fe(Me)occurs slowly at 60 °C to give an H_2/H product, but once again without disruption of the Fe–Si bond. Addition of exogenous donor ligands such as H_2, N_2 and CO effects substitution of the coordinated H_2 ligand, but the Fe–Si bond is maintained. One factor contributing to the difference between the two systems is likely the more flexible Fe–B bond in the (**TPB**)Fe system, as reflected in the variable Fe–B bond distances (varying by *ca.* 0.5 Å)[25] versus more rigid Fe–Si bond distances (varying by *ca.* 0.2 Å)[31-33] in (**SiP**$^{\mathbf{iPr}}_{\mathbf{3}}$)Fe that have been observed over several formal iron oxidation states. The rigidity of the Fe–Si interaction presumably reflects an appreciably stronger Fe–Si bond relative to Fe–B. One can additionally consider the relative Lewis acidity of the Ar_3B versus the Ar_3Si^+ subunit[33] in these respective systems, and their propensity to serve as H^- acceptors, but one might then predict the Ar_3Si^+ to be the better acceptor, in contrast to the experimental observations. Indeed, this latter point may be the reason the Fe–Si interaction is stronger than the Fe–B interaction.

Scheme 2.3 H_2 chemistry of the related (**SiP**$^{\mathbf{iPr}}_{\mathbf{3}}$)Fe silatrane system.

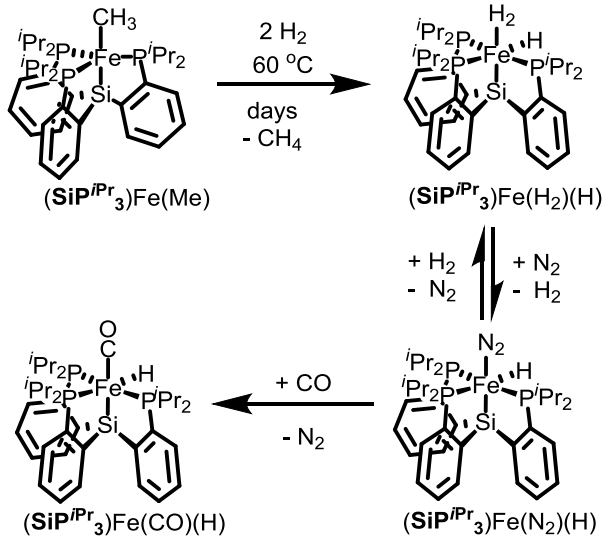

2.3.2 Reaction with Unsaturated Substrates

The ability of the (**TPB**)Fe scaffold to reversibly cleave H_2 prompted us to study if the transfer of hydrogen from (**TPB**)(μ–H)Fe(L)(H) to substrates is possible. The reaction of (**TPB**)Fe(N_2) with ethylene, styrene, and arylacetylenes was therefore probed. A degassed d_6-

Scheme 2.4 Ethylene coordination and arylacetylene C–H bond activation by (**TPB**)Fe(N_2).

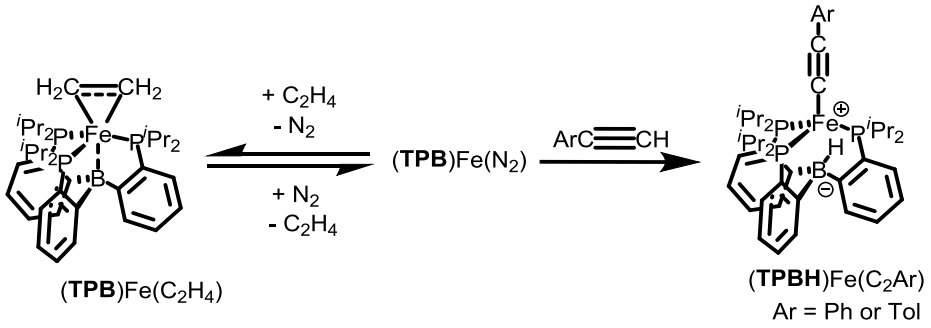

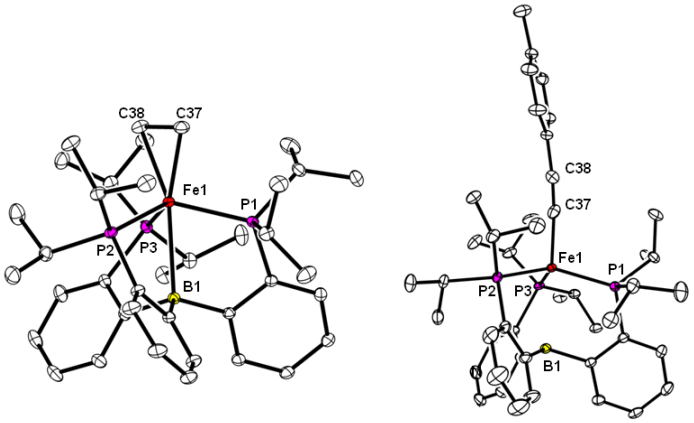

Figure 2.4 XRD structures of (**TPB**)Fe(C_2H_4) and (**TPBH**)Fe(C_2Tol). Ellipsoids shown at 50% probability. Selected bond distances (Å) and angles (°): (right) (**TPB**)Fe(C_2H_4) (average for two molecules in the asymmetric unit cell), Fe1–B1 = 2.491(1), Fe1–C37 = 2.103(1), Fe1–C38 = 2.113(1), C37–C38 = 1.397(2), ∑(P–Fe–P) = 338.76(3); (left) (**TPBH**)Fe(C_2Tol) (average for two molecules in the asymmetric unit cell), Fe1–B1 = 2.761(2), Fe1–C37 = 1.918(2) C37–C38 = 1.169(3), ∑(P–Fe–P) = 345.07(2).

benzene solution of (**TPB**)Fe(N_2) reacts with ethylene to give a light brown solution of the paramagnetic iron-ethylene adduct (**TPB**)Fe(C_2H_4) (μ_{eff} = 3.2 μ_B, S = 1) (Scheme 2.4). Brown XRD quality crystals of (**TPB**)Fe(C_2H_4) can be grown under an atmosphere of ethylene at 0 °C (Figure 2.4). Two molecules of (**TPB**)Fe(C_2H_4) were found in the asymmetric unit cell. The iron center is bound η^2 to ethylene (($Fe–C)_{avg}$ = 2.108(1) Å) and lies above the plane defined by the phosphine donors by an average distance of 0.641 Å, with a corresponding elongation of the average Fe–B distance to 2.491(2) Å (compared to 2.2 Å in (**TPB**)Fe(N_2)). The average C–C bond distance (($C–C)_{avg}$ = 1.397(2) Å) of the η^2-coordinated ethylene molecule is significantly elongated from that in free ethylene (1.337 Å).[34] The data are consistent with π-backbonding from iron to ethylene, which confers significant ferracyclopropane character to (**TPB**)Fe(C_2H_4).[35] Storing (**TPB**)Fe(C_2H_4) for two days under an atmosphere of N_2 fully regenerates (**TPB**)Fe(N_2).

Compound (**TPB**)Fe(N_2) does not afford a detectable styrene adduct but reacts with both phenyl- and tolylacetylene with formal hydride transfer from the terminal C(sp)–H of the arylacetylene to the boron, forming S = 2 iron-borohydrido-arylacetylide complexes (**TPBH**)Fe(C_2Ar) (Ar = Ph, μ_{eff} = 5.1 μ_B; Ar = Tol, μ_{eff} = 5.2 μ_B) (Scheme 2.4). Two molecules of (**TPBH**)Fe(C_2Tol) are found in the asymmetric unit, and the XRD structure shows the presence of a tolylacetylide ligand coordinated to a pyramidalized iron center (Figure 2.4). While the hydride on the boron cannot be reliably located by XRD, the IR spectra for both (**TPBH**)Fe(C_2Ph) and (**TPBH**)Fe(C_2Tol) show B–H stretches at 2490 cm^{-1} and 2500 cm^{-1}, respectively, most consistent with a non-bridging B–H unit. The vibrational bands shift

to 1826 cm^{-1} (predicted 1834 cm^{-1}) for (**TPBH**)Fe(C_2Ph) and 1824 cm^{-1} (predicted 1841 cm^{-1}) for (**TPBH**)Fe(C_2Tol) upon labeling with the monodeuterated arylacetylene (ArC≡CD).

The activation of the arylacetylene C(sp)–H bond by (**TPB**)Fe(N_2) is reversible. Mixing a d_6-benzene solution of (**TPBH**)Fe(C_2Ph) with tolylacetylene (4 equiv) and, conversely, mixing a d_6-benzene solution of (**TPBH**)Fe(C_2Tol) with phenylacetylene (4 equiv) both result in a mixture of (**TPBH**)Fe(C_2Ph) and (**TPBH**)Fe(C_2Tol) (Scheme 2.5). The corresponding exchange reactions with B–D labelled isotopologues of (**TPBD**)Fe(C_2Ph) or (**TPBD**)Fe(C_2Ar) and a different all-protio arylacetylene (Ar'C≡CH) result in the exclusive formation of free ArC≡CD, indicating that the arylacetylene unit is reductively eliminated from the iron-borohydrido-arylacetylide complexes prior to activation of an incoming acetylene substrate, presumably by reversible hydride transfer from the boron to the arylacetylide to form intermediate π-adducts akin to (**TPB**)Fe(C_2H_4) (Scheme 2.5).

Scheme 2.5 Reversible arylacetylene C–H bond activation.

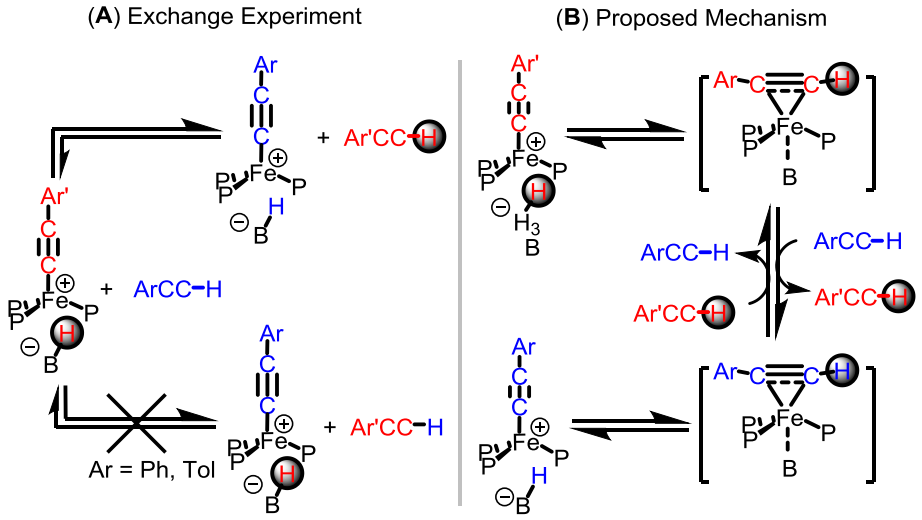

See Scheme 2.2 for the detailed ligand representation.

2.3.3 Stoichiometric Hydrogenations

We also explored whether the transfer of hydrogen from (**TPB**)(μ–H)Fe(L)(H) species to unsaturated substrates might be possible. Exposing (**TPB**)Fe(C_2H_4) to excess H_2 (1 atm) results in complete conversion of ethylene to ethane and (**TPB**)(μ–H)Fe(H_2)(H) as the iron-containing product (Scheme 2.6i) in less than 12 h. A paramagnetic intermediate (**A**) and (**TPB**)Fe(C_2H_4) can be observed by *in situ* ^{1}H NMR spectroscopy. The same paramagnetic intermediate **A** and (**TPB**)Fe(C_2H_4) can also be observed by *in situ* ^{1}H NMR spectroscopy if the same reaction is run under a mixture ethylene (1 atm) and H_2 (1 atm). The IR spectrum of the reaction mixture shows a diagnostic terminal B–H vibration at 2470 cm^{-1} that is attributed to **A**. Akin to the iron-borohydrido-alkynyl complexes (**TPBH**)Fe(C_2Ar), **A** is assigned to the iron-borohydrido-ethyl complex (Scheme 2.6i).[36] Using D_2 in place of H_2 in the ethylene hydrogenation reaction and monitoring leads to the observation of signals for both B–D and

Scheme 2.6 Stoichiometric hydrogenation reactions.

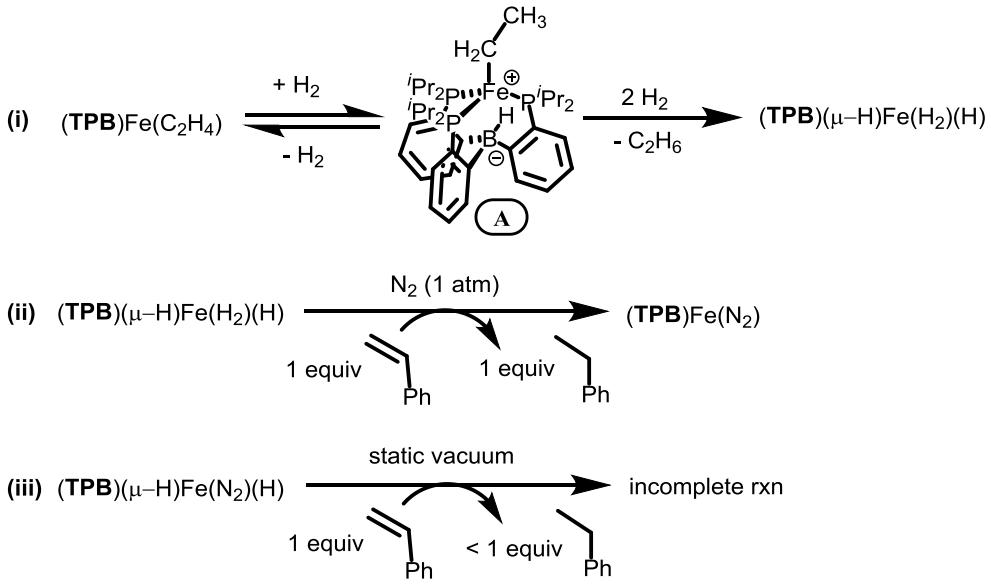

B–H stretches in the IR spectrum, which is consistent with facile insertion/β-hydride elimination processes prior to ethane elimination from **A**. We note the similarity of **A** (and (**TPBH**)Fe(C_2Ar)) to the well-characterized zwitterionic, *tris*(phosphino)borate-iron-ethyl complex (**PhBP$^{iPr}_3$**)Fe(Et) (PhBP$^{iPr}_3$ = [PhB($CH_2P^iPr_2$)$_3$]$^-$) that was observed as an intermediate in ethylene hydrogenation with the previously reported iron (**PhBP$^{iPr}_3$**)Fe system.[3e]

Complexes (**TPB**)Fe(N_2), (**TPB**)(μ–H)Fe(N_2)(H), and (**TPB**)(μ–H)Fe(H_2)(H) hydrogenate both phenylacetylene (1 equiv) and styrene (1 equiv) to ethylbenzene (1 atm H_2) with (**TPB**)(μ–H)Fe(H_2)(H) as the observable iron-containing product. The *in situ* ^{1}H NMR spectrum of styrene hydrogenation reactions using (**TPB**)Fe(N_2), (**TPB**)(μ–H)Fe(N_2)(H), or (**TPB**)(μ–H)Fe(H_2)(H) show styrene, ethylbenzene, and (**TPB**)(μ–H)Fe(H_2)(H) in solution during the reaction course. Furthermore, for styrene hydrogenation with D_2 the ^{2}H NMR spectrum and GC-MS data of the reaction mixture show incorporation of deuterium onto both olefinic carbon atoms of free styrene, indicating that styrene coordination to the iron-center and insertion/β-hydride elimination processes are reversible.

Under stoichiometric conditions, the addition of 1 equiv of styrene to a solution of (**TPB**)(μ–H)Fe(N_2)(H) in d_6-benzene and under N_2 (1 atm) cleanly generates 1 equiv of ethylbenzene and (**TPB**)Fe(N_2) (Scheme 2.6ii). In contrast, running the same reaction under a static vacuum yields a mixture of styrene, ethylbenzene, (**TPB**)Fe(N_2), and (**TPB**)(μ–H)Fe(N_2)(H) (Scheme 2.6iii). These observations suggest that excess H_2 or N_2 is

required for the hydrogenations to proceed to completion. Moreover, the bridging hydride appears competent for transfer to a substrate.

Substrates including *trans*-stilbene, N-benzylideneaniline, acetone, and acetophenone were not hydrogenated under similar conditions. Compounds (**TPB**)(μ–H)Fe(CN^{t}Bu)(H) and (**TPB**)(μ–H)Fe(CO)(H) also do not hydrogenate ethylene, styrene, or phenylacetylene under the same conditions.

2.3.4 Catalytic Hydrogenations

Under the catalytic conditions of 0.01 M (**TPB**)Fe(N_2), 1 atm of H_2, and 30 equiv of the substrate in d_6-benzene at room temperature, ethylene, styrene, and phenylacetylene are hydrogenated to ethane and ethylbenzene, respectively (Table 2.1). Compounds (**TPB**)(μ–H)Fe(N_2)(H) and (**TPB**)(μ–H)Fe(H_2)(H) can also be used as precatalysts. Ambient laboratory light does not affect the reaction, and the catalysis is not inhibited by elemental mercury; it appears to be a homogeneous process. Norbornene is hydrogenated to norbornane, and with an atmosphere of D_2 in place of H_2 the *cis*-addition product *exo*,*exo*-2,3-d_2-norbornane[37] is exclusively observed, indicating the syn-addition of hydrogen and arguing against radical processes.

The hydrogenation catalysis was monitored by ^{1}H NMR spectroscopy with ferrocene as an internal integration standard. As with stoichiometric ethylene hydrogenation, the *in situ* ^{1}H NMR spectra of the catalytic ethylene hydrogenation reaction indicate the presence of the ethylene adduct (**TPB**)Fe(C_2H_4) and the putative ethyl-borohydride intermediate **A** as the iron-containing species during the course of the reaction. Complex (**TPB**)(μ–H)Fe(H_2)(H) is the

Table 2.1 Catalytic hydrogenations by (**TPB**)Fe(N_2) with H_2.

Precatalyst	Substrate	Product	TOF (h^{-1})[c]
(**TPB**)Fe(N_2)	Ethylene[a]	Ethane	15
(**TPB**)Fe(N_2)	Styrene[a]	Ethylbenzene	0.27
(**TPB**)Fe(N_2)	Phenylacetylene[b]	Ethylbenzene	0.16

Conditions: Room temperature, 0.01 M (**TPB**)Fe(N_2), 1 atm H_2, and 0.01 M ferrocene as an internal integration standard in d6-benzene. [a]0.3 M substrate, [b]0.29 M substrate. [c]As determined by ^{1}H NMR spectroscopy at > 95% product.

iron-containing product at the completion of the reaction. For styrene hydrogenation, styrene, ethylbenzene, and (**TPB**)(μ–H)Fe(H_2)(H) are observed during catalysis, and scrambling of deuterium into the vinylic positions of styrene is observed under D_2. In contrast, for phenylacetylene hydrogenation complex (**TPBH**)Fe(C_2Ph) is the only observed iron-species early in the reaction when the phenylacetylene concentration is high. As phenylacetylene is consumed, styrene and (**TPB**)(μ–H)Fe(H_2)(H) form, and ethylbenzene begins to develop slowly thereafter.

Attempts to increase the rate of catalysis by elevating the reaction temperature resulted in catalyst decomposition. The decomposition product (**D**) can be synthesized independently in near quantitative yields by heating (**TPB**)(μ–H)Fe(H_2)(H) (80 °C) under H_2 (1 atm) for 2 h. The XRD structure of **D** indicates that a B–C_{Ar} bond is cleaved from the TPB ligand fragment (Figure 2.5). This result offers the cautionary note that B–C_{Ar} bond cleavage to give metal-borohydride products is a viable catalyst decomposition pathway.

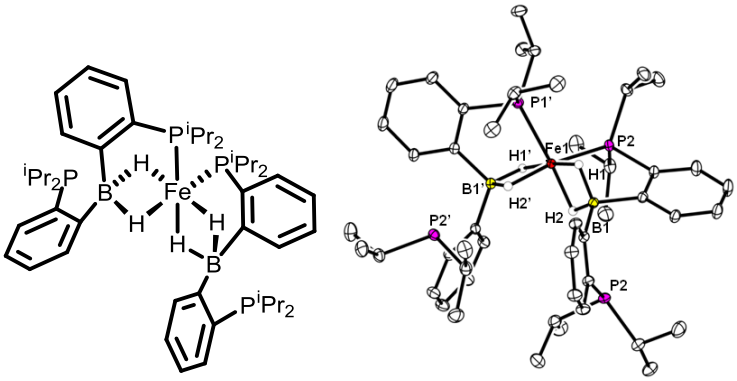

Figure 2.5 Decomposition product of the (**TPB**)Fe system. Chemical line representation (left) and XRD structure (right) of **D**. Ellipsoids shown at 50% probability. Selected bond distances (Å): Fe1–H1 = 1.59(1), Fe1–H2 = 1.63(1), Fe1–B1 = 2.0900(6), Fe1–P1 = 2.2481(2).

Based on the results from the stoichiometric and catalytic experiments, we propose a plausible mechanistic scenario to account for the observed catalytic styrene hydrogenation by (**TPB**)Fe(N_2) (Scheme 2.7A), and in doing so underscore interesting aspects of the mechanism that remain unanswered. Starting from precatalyst (**TPB**)Fe(N_2), addition of H_2 generates (**TPB**)(μ–H)Fe(H_2)(H), a species that can be observed by ^{1}H NMR spectroscopy during catalytic runs (resting state). Subsequent substitution of the apical H_2 ligand for styrene forms the unobserved iron-styrene-hydride-borohydride species **B**, and insertion into the terminal hydride affords the iron-alkyl intermediate **A'**. Intermediate **A'** is analogous to the ethyl species **A**, and is also related to the structurally characterized acetylide-borohydride complex **D**. Olefin coordination and insertion appears to be reversible, as labeling studies show deuterium is exchanged into the vinylic positions of *free* styrene under a D_2 atmosphere. Elimination of ethylbenzene in the presence of H_2 regenerates the catalyst resting state.

Scheme 2.7 Mechanism and alkane elimination pathways.

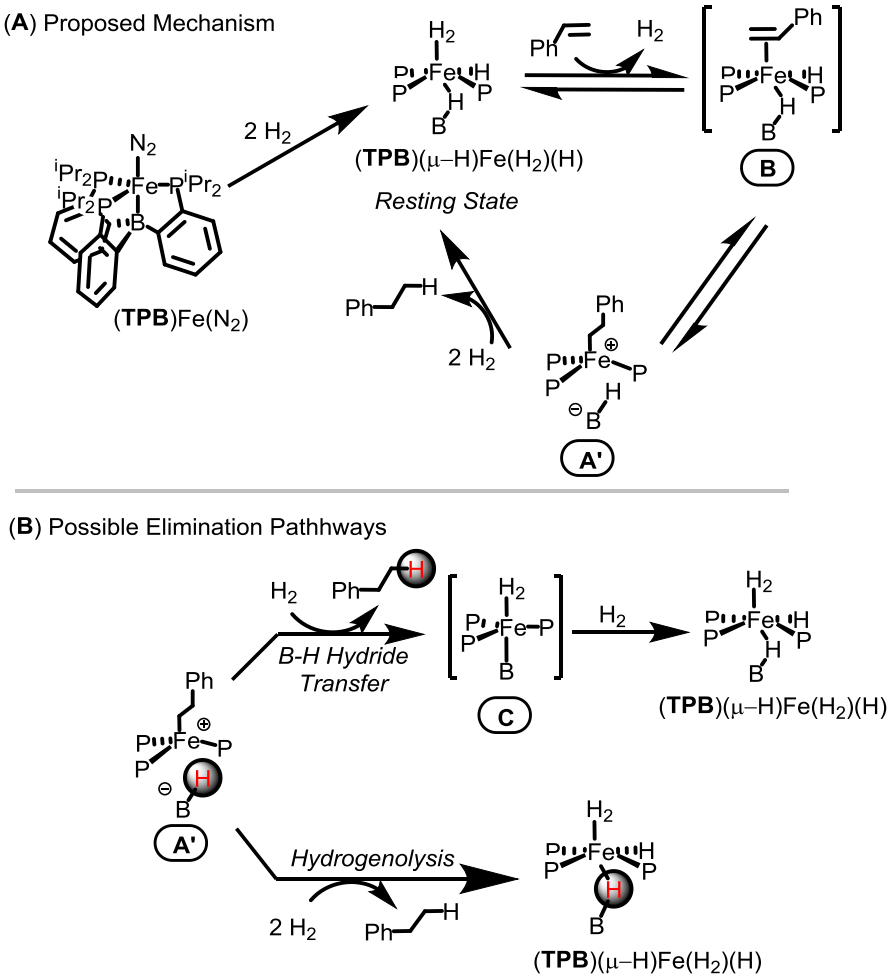

See Scheme 2.2 for the detailed ligand representation.

The conversion of (**TPB**)Fe(N_2) to (**TPB**)(μ–H)Fe(H_2)(H) likely proceeds via the H_2-adduct intermediate **C** depicted in Scheme 2.7B by H_2-for-N_2 ligand exchange. While we have not detected such a species in the present (**TPB**)Fe system, the cobalt analogue (**TPB**)Co(H_2) can be isolated and has been thoroughly characterized (see Chapter 3),[38] as has the isoelectronic iron complex [(**SiP$^{iPr}_3$**)Fe(H_2)]$^+$.[31] N_2/H_2 exchange is facile in these well-defined Co and Fe systems, and by extension we infer that it would also be facile for (**TPB**)Fe(N_2) to afford

(**TPB**)Fe(H_2) **C** before additional reactions ensue. Since H_2 reacts with (**TPB**)Fe(N_2), but not with (**TPB**)(μ–H)Fe(CN^{t}Bu)(H) and (**TPB**)(μ–H)Fe(CO)(H) at room temperature, the facile H_2 substitution for N_2 most likely occurs prior to H–H bond cleavage. While this scenario is consistent with the data available, it is not demanded by the available data. For instance, it is alternatively possible that styrene substitution for the N_2 ligand in (**TPB**)Fe(N_2) precedes H_2 addition to form intermediate **B**. No direct evidence rules out this possibility. We prefer suggesting that the H_2/dihydride species (**TPB**)(μ–H)Fe(H_2)(H) precedes styrene binding because of the observation that H_2 addition/activation by other (**TPB**)Fe(L) adducts, for example (**TPB**)Fe(CN^{t}Bu) and (**TPB**)Fe(CO), is very slow, and also because N_2, and presumably therefore also H_2, displaces ethylene from (**TPB**)Fe(C_2H_4) in solution (regenerating (**TPB**)Fe(N_2) or (**TPB**)Fe(H_2)).

The final ethylbenzene elimination step can be envisioned to occur through two plausible routes (Scheme 2.7B). One such pathway involves a reductive elimination step where hydride transfer directly from the borohydride subunit generates the alkane product to form (**TPB**)(μ–H)Fe(H_2)(H), likely via the dihydrogen adduct intermediate **C**. The other pathway proceeds through alkane elimination by hydrogenolysis of the phenylethyl group without hydride transfer from the borohydride subunit.

While the available data do not firmly distinguish between the two product elimination pathways shown in Scheme 2.7B, the stoichiometric hydrogenation studies described above show that 1 equiv of styrene is completely hydrogenated to ethylbenzene by (**TPB**)(μ–H)Fe(N_2)(H) under an N_2 atm (Scheme 2.6ii). This observation implies that

(**TPB**)(μ–H)Fe(N_2)(H) can serve as the source of the two H-atom equivalents delivered to styrene. From complex (**TPB**)(μ–H)Fe(N_2)(H), substitution of the apical N_2 ligand for styrene in (**TPB**)(μ–H)Fe(N_2)(H) would generate the styrene adduct intermediate **B**. Subsequent insertion of the bound styrene into the *cis* Fe–H would afford intermediate **A'**, which, in the absence of H_2 at least, eliminates ethylbenzene concomitant with N_2 binding to reform (**TPB**)Fe(N_2). The presence of exogenous N_2 (or alternatively H_2) facilitates the generation of ethylbenzene. As noted in Scheme 2.6iii, the stoichiometric reaction under static vacuum between (**TPB**)(μ–H)Fe(N_2)(H) and styrene is quite slow compared with the same reaction under N_2 (Scheme 2.6ii). This observation can be explained by presuming the conversion of intermediate **A'** to (**TPB**)Fe(N_2) requires N_2 association prior to elimination to generate ethylbenzene.

2.4 Conclusions

In summary, the Fe–B bond in ferraboratranes (**TPB**)Fe(L) (where L = N_2, CN^tBu, or CO) can facilitate heterolytic cleavage of H_2 and of the C(sp)–H and C(sp^2)–H bonds of arylacetylenes and formaldehyde, respectively, resulting in Fe–B bond rupture and formal hydride transfer to the boron of the ligand scaffold. The formal hydride transfer from the C(sp)–H of arylacetylenes to give iron-acetylide complexes is distinct from traditional syntheses of metal-acetylide complexes in that a hydride equivalent is formally abstracted by the Lewis acidic borane unit in (**TPB**)Fe(N_2) from a C(sp)–H hydrogen[39-41]

Dihydrogen addition across the Fe–B bond is reversible, and the boron is also capable of shuttling the hydride equivalent derived from H_2 to unsaturated substrates under stoichiometric

hydrogenation conditions. The hydrogen chemistry of this (**TPB**)Fe(N_2) system contrasts with the related nickel[42] and cobalt[38] complexes of TPB, where the metal-boron bond remains intact under an H_2 atmosphere.

An understanding of the factors that govern metal-boron bond cleavage will aid in the development of cooperative catalytic reactions in metallaboratranes. The direct role, if any, of the borane ligand in assisting the H_2 cleavage step is an interesting question in this context for the present iron and recently reported diphosphine-borane-iron systems,[43] and also conceptually related to the nickel system.[22] Determining whether there is a cooperative interaction between the coordinated H_2 ligand, the iron center, and the borane subunit en route to H–H cleavage (and its microscopic reverse) in the (**TPB**)Fe system, akin to H–H cleavage by frustrated Lewis pairs[20] and by ($^{\mathbf{Mes}}$**DPB**$^{\mathbf{Ph}}$)Ni,[44] calls for detailed theoretical studies.

2.5 Experimental

2.5.1 General Considerations

All manipulations were carried out using standard glovebox or Schlenk techniques under an N_2 atmosphere. Unless otherwise noted, solvents were deoxygenated and dried by thoroughly sparging with N_2 gas followed by passage through an activated alumina column in the solvent purification system by SG Water, USA LLC. Deuterated solvents and D_2 gas were purchased from Cambridge Isotope Laboratories, INC. The deuterated solvents were degassed and dried over activated 3 Å sieves prior to use. Unless otherwise noted, all compounds were purchased commercially and used without further purification. TPB,[26] (**SiP**$^{\mathbf{iPr}}_{\mathbf{3}}$)Fe(Me),[32]

(**SiP$^{iPr}_3$**)Fe(N_2)(H),[31] and monodeuterated phenyl- and tolylacetylene (PhC_2D and $TolC_2D$) [45] were synthesized by literature procedures. Elemental analyses were performed by Midwest Microlab, LLC., Indianapolis, IN.

NMR spectra were recorded on Varian 300 MHz, 400 MHz, and 500MHz spectrometers. ^1H and ^{13}C chemical shifts are reported in ppm relative to residual solvent as internal standards. ^{31}P and ^{11}B chemical shifts are reported in ppm relative to 85% aqueous H_3PO_4 and $BF_3{\cdot}Et_2O$, respectively. Multiplicities are indicated by br (broad), s (singlet), d (doublet), t (triplet), quart (quartet), quin (quintet), m (multiplet), d-d (doublet-of-doublets), and t-d (triplet-of-doublets).

FT-IR measurements were performed on samples prepared as KBr pellets or in solution using a Bio-Rad Excalibur FTS 300 spectrometer with Varian Resolutions Pro software at 4 cm^{-1} resolution. The ATR-IR measurements were measured on a thin film of the complex obtained from evaporating a drop of the solution on the probe surface of a Bruker APLHA ATR-IR Spectrometer (Platinum Sampling Module, diamond, OPUS software package) at 2 cm^{-1} resolution. IR intensities indicated by s (strong), m (medium), and w (weak).

X-ray Crystallography. X-ray diffraction was measured on the Bruker Kappa Apex II diffractometer with Mo Kα radiation. Structures were solved using the SHELXS software and refined against F^2 on all data sets by full matrix least squares with SHELXL. The crystals were mounted on a glass fiber with Paratone oil.

Computational Methods. Geometry optimizations were performed using the Gaussian03 package. B3LYP exchange-correlation functional was employed with a 6-31G(d) basis set. The GDIIS algorithm was used. A full frequency calculation was performed on each structure

to ensure that they were the true minima. A single negative vibrational frequency was observed for the transition state between (**TPB**)(μ–H)Fe(H_2)(H) and its equatorial-H_2 isomer, confirming that this structure was the transition state.

HD Gas Generation. D_2O (1mL) was added to an evacuated, cooled sample (-78 °C) of solid lithium aluminum hydride (316 mg, 8.2 mmol) in a Schlenk flask. An evacuated Schlenk line was filled with the resulting HD gas (*ca*. 1 atm) as the Schlenk flask was warmed to room temperature. A J-Young NMR tube containing a freeze-pump-thawed solution of the respective complex was exposed to the HD gas.

2.5.2 Synthetic Protocols

Synthesis of (TPB)(μ–H)Fe(N_2)(H). A J-Young NMR tube containing a brown-red solution (**TPB**)Fe(N_2) (20.3 mg, 31.1 mmol) in C_6H_6 (0.8 mL) was subjected to freeze-pump-thaw cycles (3x) and, with the J-Young tube frozen with liquid nitrogen, exposed to H_2 (1.2 equiv). The solution was thawed and mixed, giving a yellow solution. An atmosphere of N_2 was subsequently introduced and the reaction was mixed for 2 h to yield (**TPB**)(μ–H)Fe(N_2)(H) (100% yield by ^{1}H NMR spectroscopy with a ferrocene integration standard). Alternatively, (**TPB**)(μ–H)Fe(N_2)(H) could be synthesized from (**TPB**)(μ–H)Fe(H_2)(H) by degassing a solution of (**TPB**)(μ–H)Fe(H_2)(H) of free H_2 by freeze-pump-thaw (3x), exposing it to an N_2 atmosphere, and mixing the solution overnight (100 % yield by ^{1}H NMR spectroscopy with a ferrocene integration standard). Yields could not be determined by mass because (**TPB**)(μ–H)Fe(N_2)(H) was unstable to prolonged exposure to dynamic vacuum. Yellow-orange XRD quality crystals were grown in a concentrated solution

of pentane:THF (10:1) at -30 °C. ^{1}H NMR (C_6D_6, 300 MHz): δ 7.9 (2H, d, $^{3}J_{H\text{-}H}$ = 6 Hz, Ar-*H*), δ 7.7 (1H, br s, Ar-*H*), δ 7.3 (3H, d, $^{3}J_{H\text{-}H}$ = 6 Hz, Ar-*H*), δ 7.0 (3H, t, $^{3}J_{H\text{-}H}$ = 9 Hz, Ar-*H*), δ 2.7 (4H, d, $^{2}J_{P\text{-}H}$ = 18 Hz, PC*H*), δ 2.4 (2H, br s, PC*H*), δ 1.4 (6H, d, $^{3}J_{H\text{-}H}$ = 6 Hz, CH_3), δ 1.3 (12H, br s, CH_3), δ 1.1 (6H, d-d, $^{3}J_{P\text{-}H}$ = 15 Hz, $^{3}J_{H\text{-}H}$ = 6 Hz, CH_3), δ 0.8 (6H, d, $^{3}J_{P\text{-}H}$ = 9 Hz, CH_3), δ -9.6 (1H, d-t, $^{2}J_{H\text{-}P\textit{cis}}$ = 81 Hz, $^{2}J_{H\text{-}P\textit{trans}}$ = 36 Hz, Fe-*H*), δ -30.4 (1H, s, Fe(μ-*H*)B). ^{2}H NMR (C_6H_6/C_6D_6, 76 MHz): δ -9.5 (1D, br s), δ -30.3 (1D, br s). ^{31}P NMR (C_6D_6, 121 MHz): δ 73.6 (2P, s), δ 64.2 (1P, s). ^{13}C NMR (C_6D_6, 125 MHz): δ 161.9 (s, C^{Ar}), δ 143.5 (s, C^{Ar}), δ 141.0 (s, C^{Ar}), δ 132.3 (s, C^{Ar}), δ 131.8 (s, C^{Ar}), δ 131.3 (s, C^{Ar}), δ 130.3 (s, C^{Ar}), δ 124.6 (s, C^{Ar}), δ 124.0 (s, C^{Ar}), δ 32.0 (s, P*C*H), δ 29.4 (s, P*C*H), δ 28.5 (s, P*C*H), δ 22.8 (s, *C*H_3), δ 20.1 (s, *C*H_3), δ 19.7 (s, *C*H_3), δ 18.9 (s, *C*H_3). ^{11}B NMR (C_6D_6, 128 MHz): δ 8.2 (br). IR (KBr, cm^{-1}): 2071 (s, N≡N), 1960 (w) 1934 (w). UV-vis (THF, nm {M^{-1} cm^{-1}}): 328 {shoulder, 500}, 280 {shoulder, 11250}. Anal.: Elemental analysis could not be obtained because of the instability of the compound to dynamic vacuum.

Synthesis of (TPB)(μ–H)Fe(H_2)(H). A J-Young NMR tube containing a brown-red solution (**TPB**)Fe(N_2) (21 mg, 31.1 mmol) in C_6D_6 (0.8 mL) was subjected to freeze-pump-thaw cycles (3x). Upon warming to room temperature, the sample was exposed to H_2 (1 atm), resulting in a clear yellow solution. The reaction was mixed for 24 h to give (**TPB**)(μ–H)Fe(H_2)(H) (100 % by ^{1}H NMR spectroscopy with a ferrocene integration standard). The yield could not be determined by weight because (**TPB**)(μ–H)Fe(H_2)(H) was unstable during prolonged exposure to dynamic vacuum. Yellow-orange XRD quality crystals were grown under 1 atm of H_2 in a concentrated solution of pentane:THF (10:1) at -78 °C. ^{1}H

NMR (C_6D_6, 300 MHz): δ 8.0 (3H, d, $^3J_{H\text{-}H}$ = 6 Hz, Ar-*H*), δ 7.3 (3H, t, $^3J_{H\text{-}H}$ = 9 Hz, Ar-*H*), δ 7.2 (3H, t, $^3J_{H\text{-}H}$ = 9 Hz, Ar-*H*), δ 7.0 (3H, d, $^3J_{H\text{-}H}$ = 6 Hz, Ar-*H*), δ 4.47 (s, free H_2), δ 2.3 (6H, m, PC*H*), δ 1.0 (18H, d-d, $^3J_{H\text{-}P}$ = 15 Hz, $^3J_{H\text{-}H}$ = 6 Hz, CH_3), δ 0.8 (18H, d-d, $^3J_{H\text{-}P}$ = 15 Hz, $^3J_{H\text{-}H}$ = 6 Hz, CH_3), δ -15.1 (br s, 2H). T_{1min} (d_8-toluene): 35 ms (δ -15.1, -32 °C). ^{2}H NMR (C_6H_6/C_6D_6, 76 MHz): δ –15.4 (1D, br s). ^{31}P NMR (C_6D_6, 121 MHz): δ 90.0 (3P, s). ^{13}C NMR (C_6D_6, 125 MHz): δ 163.5 (s, C^{Ar}), δ 144.6 (s, C^{Ar}), δ 144.1 (s, C^{Ar}), δ 130.9 (d, $J_{P\text{-}C}$ = 23 Hz, C^{Ar}), δ 124.5 (s, C^{Ar}), δ 123.9 (s, C^{Ar}), δ 28.6 (s, P*C*H), δ 21.2 (s, *C*H_3), δ 19.9 (s, *C*H_3). ^{11}B NMR (C_6D_6, 128 MHz): δ 7.5 (br). IR (KBr, cm^{-1}): 2278 (w), 19618 (w), 1845 (w). UV-vis (THF, nm {M^{-1} cm^{-1}}): 377 {shoulder, 1532}, 275 {14532}. Anal.: Elemental analysis could not be obtained because of the instability of the compound to dynamic vacuum.

Synthesis of (TPB)Fe(CN^{t}Bu). *Tert*-butyl isocyanide (20 mg, 0.24 mmol) was added to a brown solution of (**TPB**)Fe(N_2) (40 mg, 59 μmol) in benzene (2 mL), causing an instantaneous darkening upon gentle shaking. The volatiles were removed by lyophilization and the residue was extracted with tetramethylsilane (2 mL). The resulting dark brown solution was slowly concentrated down to *ca*. 0.2 mL by vapor diffusion into hexamethyldisiloxane. Removal of the mother liquor by decantation, washing with cold tetramethylsilane (2 × 0.1 mL), and drying *in vacuo* afforded (**TPB**)Fe(CN^{t}Bu) as brown crystals (33 mg, 77 %). ^{1}H NMR (C_6D_6, 300 MHz): δ 11.2 (3H), δ 9.2 (3H), δ 8.6 (3H), δ 8.5 (9H), δ 6.4 (3H), δ 5.2 (9H), δ 3.7 (12H), δ 2.9 (9H), δ -1.5 (9H), δ -2.3 (3H). IR (KBr, cm^{-1}): 1972 (C≡N). UV-Vis (THF, nm {$cm^{-1}M^{-1}$}): 600 {shoulder, 428}, 910 {70}. μ_{eff} (C_6D_6, method of Evans, 20 °C): 1.7 μ_B. Anal.: Calc'd for $C_{41}H_{64}BFeNP_3$: C 67.50, H 8.70, N 1.92; found: C 67.20, H 8.54, N 1.72.

Synthesis of (TPB)(μ–H)Fe(CN^{t}Bu)(H). A heavy-walled Schlenk tube containing a yellow-brown solution of (**TPB**) Fe(CN^{t}Bu) (16.4 mg, 22.4 mmol) in C_6H_6 (10 mL) was subjected to freeze-pump-thaw cycles (3x). Upon warming to room temperature, the sample was exposed to H_2 (1 atm) for a few minutes. The Schlenk tube was sealed and heated under vigorous mixing at 40 ^{o}C for 85 h. Removal of the solvent *in vacuo*, extraction with C_6H_6, and lyophilization yielded a solid of (**TPB**)(μ–H)Fe(CN^{t}Bu)(H) (17.3 mg, 98 %). Room temperature evaporation of a solution of (**TPB**)(μ–H)Fe(CN^{t}Bu)(H) in a diethyl ether:pentane (2 mL to 1 mL) mixture yielded yellow crystals suitable for XRD analysis. ^{1}H NMR (C_6D_6, 300 MHz): δ 8.1 (1H, d, $^3J_{H\text{-}H}$ = 9 Hz, Ar-*H*), δ 7.4 (3H, d, $^3J_{H\text{-}H}$ = 9 Hz, Ar-*H*), δ 7.2 (3H, d, $^3J_{H\text{-}H}$ = 6 Hz, Ar-*H*), δ 7.1 (3H, d, $^3J_{H\text{-}H}$ = 9 Hz, Ar-*H*), δ 2.7 (2H, br s, PC*H*), δ 2.5 (2H, br s, PC*H*), δ 2.2 (2H, t, $^2J_{H\text{-}P}$ = 9 Hz, PC*H*), δ 1.3 (16H, m, CH_3), δ 1.1 (9H, s, C(CH_3)$_3$), δ 1.0 (6H, d, $^3J_{H\text{-}H}$ = 6 Hz, CH_3), δ 0.8 (6H, d-d, $^3J_{H\text{-}P}$ = 15 Hz, $^3J_{H\text{-}H}$ = 6 Hz, CH_3), δ 0.7 (6H, br s, CH_3), δ -11.7 (1H, t-d, $^2J_{H\text{-}P\textit{cis}}$ = 87 Hz, $^2J_{H\text{-}P\textit{trans}}$ = 27 Hz, Fe-*H*), δ -23.9 (1H, br s, Fe-(μ-*H*)-B). ^{13}C NMR (C_6D_6, 125 MHz): δ 176.9 (quart, $^2J_{C\text{-}P}$ = 8 Hz, *C*N^{t}Bu), δ 163.5 (br s, C^{Ar}), δ 163.0 (br s, C^{Ar}), δ 144.9 (m, C^{Ar}), δ 143.0 (d, $J_{C\text{-}P}$ = 20 Hz, C^{Ar}), δ 131.9 (d, $^2J_{C\text{-}P}$ = 7.5 Hz, C^{Ar}), δ 130.6 (d, $J_{C\text{-}P}$ = 3.2 H, C^{Ar}), δ 130.5 (d, $J_{C\text{-}P}$ = 2.5 H, C^{Ar}), δ 128.6 (s, C^{Ar}), δ 127.5 (s, C^{Ar}), δ 124.2 (s, C^{Ar}), δ 123.6 (s, C^{Ar}), δ 55.3 (s, *C*(CH$_3$)$_3$), δ 31.6 (s, P*C*H), δ 30.9 (s, P*C*H), δ 29.2 (m, P*C*H), δ 28.5 (d, $^2J_{C\text{-}P}$ = 7.5 Hz, P*C*H), δ 23.8 (s, *C*H$_3$), δ 20.4 (s, *C*H$_3$), δ 20.3 (m, *C*H$_3$), δ 20.2 (s, *C*H$_3$), δ 19.9 (s, *C*H$_3$), δ 19.7 (s, *C*H$_3$). ^{31}P NMR (C_6D_6, 121 MHz): δ 81.3 (2P, d, $^2J_{P\text{-}P}$ = 63 Hz), δ 72.4 (1P, s). IR (KBr, cm^{-1}): 2027 (s, C≡N), 1942 (w, Fe-H). UV-Vis (THF, nm {cm^{-1} M^{-1}}): 205 {5530}, 224 {15437}, 245 {17142}, 255 {16635}, 285 {4117}, 335 {shoulder, 2166},

400 {1830}. Anal: Calc'd for $C_{41}H_{66}BFeNP_3$: C 67.32, H 8.96, N 1.91; found: C 66.59, H 8.61, N 1.30.

Synthesis of (TPB)(μ−H)Fe(CO)(H) from (TPB)Fe(CO) and H_2. In a J-Young NMR tube, (**TPB**)Fe(CO) (6.0 mg, 8.9 μmol) was dissolved in C_6H_6 (0.7 mL) to give a brown-red solution. The solution was subjected to freeze-pump-thaw cycles (3x) and subsequently exposed to H_2 (1 atm) for *ca.* 5 min. The reaction was then heated at 80 ^oC for 5 days, during which time a clear yellow solution developed. Removal of the solvent *in vacuo*, extraction with C_6H_6, and lyophilization yielded a yellow solid of (**TPB**)(μ−H)Fe(CO)(H) (5.9 mg, 98 %). Room temperature evaporation of a solution of (**TPB**)(μ−H)Fe(CO)(H) in a diethyl ether:pentane (1 mL to 0.5 mL) mixture yielded yellow analytically pure (**TPB**)(μ−H)Fe(CO)(H). ^{1}H NMR (C_6D_6, 300 MHz): δ 8.1 (2H, d, $^3J_{H-H}$ = 6 Hz, Ar-*H*), δ 7.9 (1H, d, $^2J_{P-H}$ = 9 Hz, Ar-*H*), δ 7.2 (4H, m, Ar-*H*), δ 7.0 (4H, m, Ar-*H*), δ 2.6 (2H, t, $^2J_{H-P}$ = 3 Hz, PC*H*), δ 2.4 (2H, q, $^2J_{H-P}$ = 6 Hz, PC*H*), δ 2.2 (2H, t, $^2J_{H-P}$ = 6 Hz, PC*H*), δ 1.4 (6H, d, $^3J_{H-P}$ = 6 Hz, CH_3), δ 1.2 (12H, m, CH_3), δ 0.9 (6H, d, $^3J_{H-P}$ = 6 Hz, CH_3), δ 0.8 (6H, d-d, $^3J_{H-P}$ = 8 Hz, $^3J_{H-H}$ = 6 Hz, CH_3), δ 0.6 (6H, d, $^3J_{H-P}$ = 6 Hz, CH_3). δ -11.6 (1H, t-d, $^2J_{H-P\textit{cis}}$ = 81 Hz, $^2J_{H-P\textit{trans}}$ = 21 Hz, Fe-*H*), δ -20.0 (1H, br s, Fe-(μ-*H*)-B). ^{2}H NMR (C_6H_6, 76 Hz): δ -12.3 (1D, t, $^2J_{P-D}$ = 10 Hz), δ -20.8 (1D, br s). ^{13}C NMR (THF with 1 drop of C_6D_6, 125 MHz): δ 222.7 (br s, *C*O), δ 161.8 (br s, C^{Ar}), δ 142.9 (br s, $^1J_{C-P}$ = 19 Hz, C^{Ar}), δ 140.8 (br s, $^2J_{C-P}$ = 16 Hz, C^{Ar}), δ 131.0 (s, C^{Ar}), δ 129.8 (s, C^{Ar}), δ 128.5 (s, C^{Ar}), δ 128.0 (s, C^{Ar}), δ 124.0 (s, C^{Ar}), δ 123.4 (s, C^{Ar}), δ 30.8 (s, P*C*H), δ 28.3 (s, P*C*H), δ 27.7 (s, P*C*H), δ 22.3 (s, *C*H_3), δ 19.1 (s, *C*H_3), δ 18.8 (s, *C*H_3), δ 18.1 (s, *C*H_3). ^{31}P NMR (C_6D_6, 121 MHz): δ 83.4 (2P, d, $^2J_{P-H}$ = 21 Hz), δ 72.8 (1P,

s). IR (KBr, cm^{-1}): 1898 (s, C≡O), 1967 (w, Fe-H). UV-Vis (THF, nm {$cm^{-1}M^{-1}$}): 270 {4333}, 280 {4111}, 390 {1400}. Anal.: Calc'd for $C_{37}H_{56}BFeOP_3$: C 65.70, H 8.34; found: C 65.64, H 8.08.

Synthesis of (TPB)(μ–H)Fe(CO)(H) from Formaldehyde. Compound (**TPB**)Fe(N_2) (8 mg, 11.8 μmol) or (**TPB**)(μ–H)Fe(N_2)(H) (6 mg, 8.9 μmol) was mixed with excess paraformaldehyde in C_6H_6 for 3 h to give a turbid, light yellow solution. The excess paraformaldehyde was filtered away and the solution was pumped down to give (**TPB**)(μ–H)Fe(CO)(H) as a yellow solid (from (**TPB**)Fe(N_2), 8 mg, 100 %; from (**TPB**)(μ–H)Fe(N_2)(H), 7 mg, 100 %). Spectroscopic data is identical to those listed above.

Synthesis of (TPB)Fe(C_2H_4). A J-Young NMR tube containing an orange solution of (**TPB**)(μ–H)Fe(H_2)(H) (8.4 mg, 12.5 μmol) in C_6H_6 (0.8 mL) was subjected to freeze-pump-thaw cycles (3x) and exposed to ethylene gas (1 atm) for *ca*. 1 minute. Mixing immediately gave a brown solution of (**TPB**)Fe(C_2H_4). Removal of solvent *in vacuo* yielded a brown solid (8.3 mg, 99 %) of (**TPB**)Fe(C_2H_4). Dissolution of this solid under N_2 atmosphere gave mostly (**TPB**)Fe(C_2H_4) and small amounts of (**TPB**)Fe(N_2). Over time, (**TPB**)Fe(C_2H_4) in solution converted to (**TPB**)Fe(N_2). Crystals suitable for XRD were grown in a saturated, cold pentane:diethyl ether (2:1) solution under an ethylene atmosphere. ^{1}H NMR (C_6D_6, 300 MHz): δ 33.1 (1H), δ 28.8 (1H), δ 18.7 (4H), δ 13.3 (1H), δ 5.25 (s, free C_2H_4), δ 4.9 (3H), δ 4.1 (1H), δ 1.9 (2H), δ -3.0 (10H), δ -6.2 (11H), δ -9.2 (11H), δ -10.0 (3H). UV-Vis (THF, nm {$cm^{-1}M^{-1}$}): 309 {shoulder, 6032}, 553 {1804}, 938 {418}. μ_{eff} (C_6D_6, method of Evans, 20 °C): 3.2 μ_B

(*S* = 1). Anal.: Elemental analysis could not be obtained because of the instability of the compound to dynamic vacuum.

Synthesis of (TPBH)Fe(C_2Ph). Phenylacetylene (40.8 mg, 400 μmol) was added to a C_6H_6 solution (5 mL) of (**TPB**)(μ–H)Fe(H_2)(H) (9.0 mg, 13 μmol), immediately giving a gray solution. Removal of the solvent *in vacuo* yielded a black powder of (**TPBH**)Fe(C_2Ph) (10 mg, 100 %). ^{1}H NMR (C_6D_6, 300 MHz): δ 28.8 (3H), δ 13.1 (4H), δ 4.7 (18H), δ 2.6 (2H), δ 2.3 (4H), δ 1.2 (2H), δ -29.3 (1H), δ -30.9 (5H). μ_{eff} (C_6D_6, method of Evans, 20 °C): 5.1 μ_B (*S* = 2). UV-Vis (THF, nm {$cm^{-1}M^{-1}$}): 325 {20670}, 439 {1051}, 479 {971}, 522 {955}, 601 (br abs extending from 400 to 700 nm, 930}, 883 {1466}. IR (KBr, cm^{-1}): 2040 (s, C≡C), 2490 (m, B-H). Anal.: Calc'd for $C_{44}H_{60}FeP_3B$: C, 70.60; H, 8.08. Found: C, 70.39; H, 7.89.

Synthesis of (TPBD)Fe(C_2Ph). The B-D labeled isotopologue (**TPBD**)Fe(C_2Ph) was generated by the same method described for (**TPBH**)Fe(C_2Ph), except that PhC_2H was replaced with PhC_2D. The ^{1}H NMR spectrum was identical to (**TPBD**)Fe(C_2Ar). IR (thin film, cm^{-1}): 1826 (br m, B-D; predicted 1832).

Synthesis of (TPBH)Fe(C_2Tol). Tolylacetylene (16.1 mg, 138 μmol) was added to a C_6H_6 solution (5 mL) of **3** (22.9 mg, 33.0 μmol), immediately giving a gray solution. Removal of the solvent *in vacuo* yielded a black powder of (**TPBH**)Fe(C_2Tol) (24.0 mg 100 %). Black XRD quality crystals of (**TPBH**)Fe(C_2Tol) were grown by layering hexamethyldisiloxane on top of a concentrated THF solution of (**TPBH**)Fe(C_2Tol) and allowing the solution to sit overnight. ^{1}H NMR (C_6D_6, 300 MHz): δ 44.1 (1H), δ 29.4 (1H), δ 13.3 (1H), δ 4.6 (2H), δ 3.3 (1H), δ 2.7 (2H), δ 2.3 (4H), δ 1.8 (2H), δ -32.3 (1H). μ_{eff} (C_6D_6, method of Evans, 20 °C): 5.2 μ_B (*S* = 2).

UV-Vis (THF, nm {$cm^{-1}M^{-1}$}): 326 {24476}, 444 {1243}, 486 {1138}, 527 {shoulder, 975}, 624 (915}, 887 {1575}. IR (KBr, cm^{-1}): 2039 (s, C≡C), 2500 (m, B-H). Anal.: Calc'd for $C_{45}H_{62}FeP_3B$: C, 70.88; H, 8.20. Found: C, 70.44; H, 7.80.

Synthesis of (TPBD)Fe(C_2Tol). The B-D labeled isotopologue (**TPBD**)Fe(C_2Tol) was generated by the same method described for (**TPBH**)Fe(C_2Tol), except that TolC_2H was replaced with TolC_2D. The ^{1}H NMR spectrum was identical to (**TPBH**)Fe(C_2Tol). IR (thin film, cm^{-1}): 1824 (br m, B-D; predicted 1841).

Synthesis of D. A yellow, C_6H_6 solution of (**TPB**)Fe(N_2) (18.2 mg, 27 μmol) was heated in a J-Young NMR tube under H_2 (1 atm) at 80 °C for 2 h, giving a turbid red-purple solution. The solvent was removed *in vacuo*, and the dark crude material was redissolved in hexamethyldisiloxane (3 mL) and filtered through a glass frit to remove a black solid (presumably iron metal). Removal of the solvent *in vacuo* gave a purple solid that is a mixture of **D** (1 equiv) and diisopropyl-phosphino-benzene ($^{i\text{Pr}2}$PPh, 1 equiv). Orange XRD quality crystals of **D** can be grown from slow evaporation of a concentrated hexamethyldisiloxane solution of **11** at room temperature (5.1 mg, 18 %). Dissolution of these crystals by heating in benzene or THF results in decomposition. Therefore, spectral data is reported on the mixture of **D** with $^{i\text{Pr}2}$PPh. Compound **D** appears to be fluxional at RT. ^{1}H NMR (C_6D_6, 300 MHz): δ 8.4 (4H, s, Ar-*H*), δ 7.6 (4H, s, Ar-*H*), δ 7.5 (3H, d, $^2J_{H\text{-}P}$ = 6 Hz, Ar-*H*), δ 2.7 (1H, d, $^2J_{H\text{-}P}$ = 6 Hz, PC*H*), δ 2.5 (1H, s, PC*H*), δ 1.9 (1H, quart, $^3J_{H\text{-}H}$ = 6 Hz, PC*H*), δ 1.3 (6H, d-d, $^3J_{P\text{-}H}$ = 4 Hz, $^3J_{H\text{-}H}$ = 2 Hz, CH_3), δ 1.2 (6H, d, $^3J_{H\text{-}H}$ = 3 Hz, CH_3), δ 1.1 (6H, quart, $^3J_{P\text{-}H}$ = 4 Hz, $^3J_{H\text{-}H}$ = 2 Hz, CH_3), 0.9 (12H, m, CH_3), -17.0 (0.25H, t, $^2J_{H\text{-}P}$ = 36 Hz, B-*H*). ^{13}C NMR (C_6D_6, 125

MHz): δ 157.4 (br s, C^{Ar}), δ 144.2 (br s, C^{Ar}), δ 134.9 (d, $^{2}J_{C\text{-}P}$ = 19 Hz, C^{Ar}), δ 130.5 (s, C^{Ar}), δ 129.3 (s, C^{Ar}), δ 125.7 (d, $^{2}J_{C\text{-}P}$ = 23 Hz, C^{Ar}), δ 25.5 (br s, P*C*H), δ 24.9 (br s, P*C*H), δ 24.4 (br s, P*C*H), δ 23.7 (br s, P*C*H), δ 23.1 (br s, P*C*H), δ 20.0 (m, *C*H_3), δ 19.4 (m, *C*H_3), δ 18.2 (m, *C*H_3). ^{31}P NMR (C_6D_6, 121 MHz): δ 99.1 (4P, s), δ 9.5 (2P, s). ^{11}B NMR (C_6D_6, 128 MHz): δ 41.0 (br). UV-Vis (THF, nm {$cm^{-1}M^{-1}$}): 264 {shoulder, 31650}, 520 {826}. IR (KBr, cm^{-1}): 2088 (s, B-H), 1838 (m, B-H). Anal.: Calc'd for $C_{51}H_{86}FeP_4B_2Si$ (i.e., **11** + Me_3SiH): C, 65.96; H, 9.33. Found: C, 65.70; H, 9.16.

Synthesis of (SiP$^{iPr}_3$)Fe(H_2)(H). In a 100 mL Schlenk tube a red solution of (**SiP$^{iPr}_3$**)Fe(Me) (1.05 g, 1.547 mmol) in C_6H_6 (50 mL) was degassed by freeze-pump-thaw (3x). H_2 gas (1 atm) was charged into the reaction mixture. The reaction was heated at 60 °C for over a week. The reaction solution was then quickly filtered through Celite and volatiles were removed *in vacuo* to give a light yellow powder. The solid was collected on a glass-frit and washed with pentane (3 mL x 2). The resulting product **(SiP$^{iPr}_3$)Fe(H_2)(H)** (950 mg, 1.425 mmol, 92%) was obtained as a light yellow powder after drying under vacuum. ^{1}H NMR (C_6D_6, 300 MHz): δ 8.3 (3H, d, $^{3}J_{H\text{-}P}$ = 6.8 Hz, Ar-*H*), δ 7.3 (3H, m, Ar-*H*), δ 7.2 (3H, t, $^{3}J_{H\text{-}H}$ = 7.2 Hz, Ar-*H*), δ 7.1 (3H, t, $^{3}J_{H\text{-}H}$ = 7 Hz, Ar-*H*), δ 4.5 (s, free H_2), δ 2.2 (6H, m, PC*H*), δ 1.0 (18H, m, CH_3), δ 0.8 (18H, br s, CH_3), δ 0.16 (s, free CH_4), δ –10.0 (3H, quin, $^{2}J_{P\text{-}H}$ = 18.4 Hz, Fe-*H*). T_{1min} (d_8-toluene): 32 ms (δ -10.0, -30 °C). ^{31}P NMR (C_6D_6, 121 MHz): δ 100 (br); (d_8-Tol, 121 MHz, -80 °C): δ 117.9 (d, $^{3}J_{P\text{-}P}$ = 43.5 Hz), δ 94.7 (bs), δ 84.7 (d, $^{3}J_{P\text{-}P}$ = 43.5 Hz). ^{13}C NMR (THF with 1 drop of C_6D_6, 125 MHz): δ 157.3 (d, $J_{C\text{-}P}$ = 22.5 Hz, C^{Ar}), δ 150.5 (d, $J_{C\text{-}P}$ = 21.3 Hz, C^{Ar}), δ 130.1 (d, $J_{C\text{-}P}$ = 9.3 Hz, C^{Ar}), δ 128.6 (s, C^{Ar}), δ 127.4 (s C^{Ar}), δ 126.0 (d, $J_{C\text{-}P}$ = 2.5 Hz,

C^{Ar}), δ 29.0 (br s, P*C*H), δ 20.4 (br s, *C*H_3), δ 19.2 (br s, *C*H_3), UV-Vis (THF, nm {$cm^{-1}M^{-1}$}): 353 {3040}. IR (KBr pellet; cm^{-1}): 1941 (w, Fe-H). Anal.: Elemental analysis could not be obtained because of the instability of the compound under prolonged exposure to N_2.

Isotopomers of (SiP$^{iPr}_3$)Fe(H_2)(H): (SiP$^{iPr}_3$)Fe(H_2)(H), (SiP$^{iPr}_3$)Fe(HD)(H), (SiP$^{iPr}_3$)Fe(H_2)(D), (SiP$^{iPr}_3$)Fe(D_2)(H), (SiP$^{iPr}_3$)Fe(HD)(D), and (SiP$^{iPr}_3$)Fe(D_2)(D). HD gas was generated by the method described above and charged into a J-young tube containing a degassed solution of (**SiP$^{iPr}_3$)**Fe(Me) in C_6D_6. The solution was heated at 60 ^oC for over a week. Monitoring the progress of the reaction by ^1H NMR revealed the gradual disappearance of (**SiP$^{iPr}_3$)**Fe(Me) and formation of diamagnetic isotopomers (**SiP$^{iPr}_3$)**Fe(H_2)(H). Spectroscopic features in the ^1H NMR spectrum were identical to (**SiP$^{iPr}_3$)**Fe(H_2)(H) except for the hydridic proton resonances, where isotopologues were observed. $^1H\{^{31}P\}$ NMR (C_6D_6, 300 MHz): δ -10.0 (3H, quart, $^2J_{P\text{-}H}$ = 18.4 Hz, H_3), δ -10.0 (t, $^1J_{H\text{-}D}$ = 9.5 Hz, H_2D), δ -10.2 (quin, $^1J_{H\text{-}D}$ = 9.3 Hz, HD_2).

Synthesis of (SiP$^{iPr}_3$)Fe(CO)(H). In a 50 mL Schlenk tube a yellow solution of (**SiP$^{iPr}_3$)**Fe(H_2)(H) (330 mg, 0.495 mmol) in C_6H_6 (20 mL) was subjected to freeze-pump-thaw cycles (3x). The solution was charged with CO (1 atm). The reaction was mixed overnight at RT and then for 1 h at 60 ^oC, resulting in a light yellow solution. After completion, the solution was degassed by freeze-pump-thaw (3x). The solution was filtered through Celite, and the volatiles were removed *in vacuo* to give a light yellow powder. The solid was collected on a glass-frit and washed with pentane (5 mL x 3). Removal of the solvent *in vacuo* yields (**SiP$^{iPr}_3$)**Fe(CO)(H) (266 mg, 0.384 mmol, 78 %) as a light yellow powder. Crystals suitable

for X-ray diffraction were obtained by RT evaporation of a pentane solution of (**SiP$^{iPr}_3$**)Fe(CO)(H). ^{1}H NMR (d_8-toluene, 300 MHz): δ 8.2 (2H, d, $^3J_{H-H}$ = 7.2 Hz), δ 8.1 (1H, d, $^3J_{H-H}$ = 7.2 Hz), δ 7.3 (3H, m), δ 7. 2 (3H, m), δ 7.1 (3H, m), δ 2.7 (2H, m), δ 2.4 (2H, m), δ 2.2 (2H, m), δ 1.5 (6H, d-d, $^3J_{H-P}$ = 15.2 Hz, $^3J_{H-P}$ = 6.8 Hz), δ 1.3 (6H, m), δ 1.1 (6H, d-d, $^3J_{H-P}$ = 12.6 Hz, $^3J_{H-H}$ = 6.6 Hz), δ 0.8 (12H, m), δ 0.5 (6H, s), δ -14.9 (1H, t-d, $^3J_{H-Pcis}$ = 81.0 Hz, $^3J_{H-Ptrans}$ = 14.1 Hz). ^{31}P NMR (C_6D_6, 121 MHz, RT): δ 88.0 (br), δ 90.0 (s); (d_8-toluene, 121 MHz, –80 °C): δ 109.9 (t, $^3J_{P-P}$ = 65 Hz, $^3J_{P-H}$ = 80 Hz), δ 90.0 (s), δ 77.9 (t, $^3J_{P-P}$ = 65 Hz, $^3J_{P-H}$ = 80 Hz). ^{13}C NMR (THF with 1 drop of C_6D_6, 125 MHz): δ 223.0 (d, $^2J_{C-P}$ = 6.3 Hz, *C*O), δ 157.2 (d, J_{C-P} = 8.8 Hz, C^{Ar}), δ 155.2 (d, J_{C-P} = 10.6 Hz, C^{Ar}), δ 150.5 (d, J_{C-P} = 11.3 Hz, C^{Ar}), δ 150.2 (d, J_{C-P} = 8.8 Hz, C^{Ar}), δ 148.6 (d, J_{C-P} = 18.1 Hz, C^{Ar}), δ 132.4 (d, J_{C-P} = 9.4 Hz, C^{Ar}), δ 131.9 (d, J_{C-P} = 8.8 Hz, C^{Ar}), δ 130.9 (s, C^{Ar}), δ 128.3 (s, C^{Ar}), δ 128.5 (s, C^{Ar}), δ 127.1 (s, C^{Ar}), δ 126.8 (s, C^{Ar}), δ 126.4 (s, C^{Ar}), δ 125.8 (s, C^{Ar}), δ 124.7 (s, C^{Ar}), δ 32.4 (s, P*C*H), δ 30.7 (s, P*C*H), δ 30.0 (s, P*C*H), δ 29.6 (s, P*C*H), δ 28.7 (s, P*C*H), δ 22.8 (s, *C*H$_3$), δ 22.1 (s, *C*H$_3$), δ 20.2 (s, *C*H$_3$), δ 19.5 (s, *C*H$_3$), δ 19.2 (s, *C*H$_3$), δ 19.1 (s, *C*H$_3$), δ 18.9 (s, *C*H$_3$), δ 18.0 (s, *C*H$_3$). UV-Vis (THF, nm {cm^{-1}M^{-1}}): 340 {2,050}, 400 {1,500}. IR (KBr pellet; cm^{-1}): 1882 (s, C≡O), 1944 (m, Fe-H). Anal.: Calc'd for $C_{37}H_{57}FeOP_3Si$: C, 64.16; H, 8.00. Found: C, 64.15; H, 8.13.

Synthesis of (SiP$^{iPr}_3$)Fe(^{13}CO)(H). In a J-Young NMR tube an orange C_6D_6 solution of (**SiP$^{iPr}_3$**)Fe(H_2)(H) was degassed by three freeze-pump-thaw (3x). Subsequently, ^{13}CO (1 atm) was added and the reaction was allowed to mix overnight at RT. The ^{1}H NMR spectrum was identical to (**SiP$^{iPr}_3$**)Fe(CO)(H). IR (KBr; cm^{-1}): 1836 (s, ^{13}C≡O).

Generation of (TPBH)Fe(Et) (A). Compound **A** was observed as an intermediate of catalytic ethylene hydrogenation under the reaction conditions described below ("Catalytic hydrogen studies"). Complex **A** can also be generated starting from complex (**TPB**)Fe(C_2H_4)**.** The procedure described below is more amendable to observing **A** spectroscopically. A dark yellow C_6D_6 solution (0.5 mL) of (**TPB**)Fe(C_2H_4) (2.8 mg, 4.2 μmol) under ethylene (1 atm) in a J-Young tube was frozen (-196 °C) and H_2 was added (1 atm). The reaction was thawed and quickly mixed only *immediately* prior to measuring the ^{1}H NMR spectrum, revealing a mixture of (**TPB**)Fe(C_2H_4) and **A**. Further mixing of the solution for *ca*. 45 min yielded a purple solution of **A** with a small residual amount of (**TPB**)Fe(C_2H_4) by ^{1}H NMR spectroscopy. Free C_2H_4, C_2H_6, and H_2 were also observed in the ^{1}H NMR spectrum. Compound **A** could not be isolated as a solid due to its instability. For example, an ATR-IR spectrum of a thin film of the reaction mixture obtained by solvent evaporation under an N_2 atmosphere over a period less than 30 sec gave vibrational bands diagnostic of (**TPB**)Fe(N_2), (**TPB**)(μ–H)Fe(N_2)(H), and **A**. ^{1}H NMR (C_6D_6, 300 MHz): δ 17.3 (1H), δ 6.6 (1H), δ 5.26 (s, free C_2H_4), δ 4.4 (1H), δ 4.47 (br s, free H_2), δ 3.3 (2H), 0.80 (s, free C_2H_6), δ -1.9 (8H), δ -5.5 (6H). IR (thin film; cm^{-1}): 2470 (br s, B–H of **A**), 2069 (m, N≡N of (**TPB**)(μ–H)Fe(N_2)(H)), 2009 (s, N≡N of (**TPB**)Fe(N_2)). UV-Vis, obtained 45 min after exposing **A** under 1 atm of ethylene to 1 atm of H_2 (THF, nm {$cm^{-1}M^{-1}$}): 325 {20670}, 439 {1051}, 479 {971}, 522 {955}, 601 (br abs extending from 400 to 600 nm, 930}, 883 {1466}. Magnetic data could not be obtained due to the presence of multiple iron species in the reaction mixture. Anal.: Elemental analysis could not be obtained because of the instability of the compound to dynamic vacuum.

Catalytic hydrogenation studies. Compound (**TPB**)Fe(N_2) (0.045 g, 0.07 mmol) and ferrocene (0.012 g, 0.07 mmol) were dissolved in 1.5 mL of C_6D_6, giving a 0.045 M precatalyst stock solution. Ferrocene was used as an internal ^{1}H NMR integration standard, and it did not affect the rates of hydrogenation. For a catalytic run, 0.1 mL of the stock solution was taken and mixed with 0.35 mL of C_6D_6, and 30 equiv of substrate in a J-Young NMR tube (3.2 mL capacity). For styrene hydrogenation, this equates to 0.01 M (**TPB**)Fe(N_2) and 0.3 M styrene. For phenylacetylene hydrogenation, this equates to 0.01 M (**TPB**)Fe(N_2) and 0.29 M phenylacetylene. For ethylene hydrogenation, this equates to 0.01 M (**TPB**)Fe(N_2) and 0.30 M ethylene. The sample in the J-Young NMR tube was subsequently degassed by freeze-pump-thaw cycles (3x) and backfilled with 1 atm H_2 (0.11 mmol). The J-Young NMR tube was continually rotated (12 min^{-1}) to ensure adequate mass transfer. The tube was periodically refilled with H_2 to maintain 1 atm of H_2. All reactions were monitored periodically by ^{1}H NMR spectroscopy until >95% completion. All reactions resulted in clean conversion of the substrate to the corresponding product. Catalytic runs in the presence of a drop of mercury or in the absence of ambient laboratory light had no affect on the reactions. Catalytic hydrogenations could also be cleanly effected by pre-generating (**TPB**)(μ–H)Fe(N_2)(H) or (**TPB**)(μ–H)Fe(H_2)(H) before the addition of the substrate.

2.6 Cited References

(1) Hartwig, J. F. *Organotransition Metal Chemistry: From Bonding to Catalysis*; 1st ed.; University Science Books: Sausalito, California, 2010.

(2) Bullock, R. M. *Catalysis without Precious Metals*; Wiley-VCH Verlag GmbH & Co. KGaA: Weinheim, Germany, 2010.

(3) For representative examples of mid-to-late first row transition metal catalysts that perform two-electron transformations see: (a) Bolm, C.; Legros, J.; Le Paih, J.; Zani, L. *Chem. Rev.* **2004,** *104,* 6217-6254; (b) Hu, X. *Chem. Sci.* **2011,** *2,* 1867-1886; (c) Q. Knijnenburg, Q.; Horton, A. D.; van der Heijden, H.; Kooistra, T. M.; Hetterscheid, D. G. H.; Smits, J. M. M.; de Briun, B.; Budzelaar, P. H. M.; Gal, A. W. *J. Mol. Catal. A: Chem* **2005,** *232,* 151-159; (d) Tondreau, A. M. Atienza, C. C. H.; Weller, K. J.; Nye, S. A.; Lewis, K. M.; Delis, J. G. P.; Chirik, P. J. *Science* **2012,** *335,* 567-570; (e) Daida, E. J.; Peters, J. C. *Inorg. Chem.* **2004,** *43,* 7474-7585; (f) Federsel, C.; Boddien, A.; Jackstell, R.; Jennerjahn, R.; Dyson, P. J.; Scopelliti, R.; Laurenczy, G.; Beller, M. *Angew. Chem. Int. Ed.* **2010,** *49,* 9777-9780.

(4) Noyori, R.; Yamakawa, M.; Hashiguchi, S. *J. Org. Chem.* **2001**, *66,* 7931-7944.

(5) Morris, R. H. *Chem. Soc. Rev.* **2009**, *38,* 2282-2291.

(6) Chakraborty, S.; Guan, H. *Dalton Trans.* **2010**, *39,* 7427-7436.

(7) Casey, C. P.; Guan, H. *J. Am. Chem. Soc.* **2007**, *129,* 5816-5817.

(8) Sui-Seng, C.; Freutel, F.; Lough, A. J.; Morris, R. H. *Angew. Chem. Int. Ed.* **2008**, *47,* 940-943.

(9) Langer, R.; Leitus, G.; Ben-David, Y.; Milstein, D. *Angew. Chem. Int. Ed.* **2011**, *50*, 2120-2124.

(10) For discussions on the M–B bonding situation: (a) Sircoglou, M.; Bontemps, S.; Mercy, M.; Saffon, N.; Takahashi, M.; Bouhadir, G.; Maron, L.; Bourissou, D. *Angew. Chem., Int. Ed.* **2007,** *46*, 8583-8586; (b) Amgoune, A.; Bourissou, D. *Chem. Comm.* **2011,** *47*, 859-871; (c) Hill, A. F. *Organometallics* **2006,** *25*, 4741-4743; (d) Parkin, G. *Organometallics* **2006,** *25*, 4744-4747.

(11) Owen, G. R. *Chem. Soc. Rev.* **2012**, *41*, 3535-3546.

(12) Tsoureas, N.; Owen, G. R.; Hamilton, A.; Orpen, A. G. *Dalton Trans.* **2008**, 6039-6044.

(13) Crossley, I. R.; Foreman, M. R. S. J.; Hill, A. F.; Owen, G. R.; White, A. J. P.; Williams, D. J.; Willis, A. C. *Organometallics* **2008**, *27*, 381-386.

(14) Crossley, I. R.; Foreman, M. R. S. J.; Hill, A. F.; White, A. J. P.; Williams, D. J. *Chem. Commun.* **2005**, 221-223.

(15) Crossley, I. R.; Hill, A. F.; Willis, A. C. *Organometallics* **2007**, *26*, 3891-3895.

(16) Crossley, I. R.; Hill, A. F. *Dalton Trans.* **2008**, 201-203.

(17) Crossley, I. R.; Hill, A. F.; Willis, A. C. *Organometallics* **2008**, *27*, 312-315.

(18) Hill, A. F.; Smith, M. K.; Wagler, J. *Organometallics* **2008**, *27*, 2137-2140.

(19) Crossley, I. R.; Hill, A. F.; Willis, A. C. *Organometallics* **2009**, *29*, 326-336.

(20) Stephan, D. W.; Erker, G. *Angew. Chem. Int. Ed.* **2010**, *49*, 46-76.

(21) Tsoureas, N.; Kuo, Y.-Y.; Haddow, M. F.; Owen, G. R. *Chem. Commun.* **2011**, *47*, 484-486.

(22) Harman, W. H.; Peters, J. C. *J. Am. Chem. Soc.* **2012**, *134*, 5080-5082.

(23) Kameo, H.; Nakazawa, H. *Organometallics* **2012**, *31*, 7476-7484.

(24) Moret, M.-E.; Peters, J. C. *Angew. Chem. Int. Ed.* **2011**, *50*, 2063-2067.

(25) Moret, M.-E.; Peters, J. C. *J. Am. Chem. Soc.* **2011**, *133*, 18118-18121.

(26) Bontemps, S.; Bouhadir, G.; Dyer, P. W.; Miqueu, K.; Bourissou, D. *Inorg. Chem.* **2007**, *46*, 5149-5151.

(27) Desrosiers, P. J.; Cai, L.; Lin, Z.; Richards, R.; Halpern, J. *J. Am. Chem. Soc.* **1991**, *113*, 4173-4184.

(28) Kubas, G. J. *Chem. Rev.* **2007**, *107*, 4152-4205.

(29) Morris, R. H. *Coord. Chem. Rev.* **2008**, *252*, 2381-2394.

(30) Van der Sluys, L. S.; Eckert, J.; Eisenstein, O.; Hall, J. H.; Huffman, J. C.; Jackson, S. A.; Koetzle, T. F.; Kubas, G. J.; Vergamini, P. J.; Caulton, K. G. *J. Am. Chem. Soc.* **1990**, *112*, 4831-4841.

(31) Lee, Y.; Kinney, R. A.; Hoffman, B. M.; Peters, J. C. *J. Am. Chem. Soc.* **2011**, *133*, 16366-16369.

(32) Lee, Y.; Mankad, N. P.; Peters, J. C. *Nature Chem.* **2010**, *2*, 558-565.

(33) Lee, Y.; Peters, J. C. *J. Am. Chem. Soc.* **2011**, *133*, 4438-4446.

(34) Bartell, L. S.; Roth, E. A.; Hollowell, C. D.; Kuchitsu, K.; Young, J. E. *J. Chem. Phys.* **1965**, *42*, 2683-2686.

(35) Select iron-ethylene complexes of ferracyclopropane character: (a) Zenneck, U.; Frank, W. *Angew. Chem., Int. Ed*. **1986,** *25*, 831-833; (b) Schneider, J. J.; Czap, N.; Blaser, D.; Boese,

R. *J. Am. Chem. Soc.* **1999,** *121,* 1409-1410; (c) Bennett, M. A.; Ditzel, E. J.; Hunter, A. D.; Khan, K.; Kopp, M. R.; Neumann, H.; Robertson, G. B.; Zeh, H. *J. Chem. Soc., Dalton Trans.* **2000,** 1733-1741; (d) Fürstner, A.; Martin, R.; Krause, H.; Seidel, G.; Goddard, R.; Lehmann, C. W. *J. Am. Chem. Soc.* **2008,** *130,* 8773-8787.

(36) A similar paramagnetic (*S* = 2) iron ethyl-hydro-tris(pyrazolyl)borate complex: Shirasawa, N.; Nguyet, T. T.; Hikichi, S.; Moro-oka, Y.; Akita, M. *Organometallics* ***2001,*** *20,* 3582-3598.

(37) Marchand, A. P.; Marchand, N. W. *Tetrahedron Lett.* **1971**, *12*, 1365-1368.

(38) Suess, D. L. M.; Tsay, C.; Peters, J. C. *J. Am. Chem. Soc.* **2012**, *134*, 14158-14164.

(39) Reinhard, N. *Coord. Chem. Rev.* **1982**, *47*, 89-124.

(40) Bianchini, C.; Laschi, F.; Masi, D.; Ottaviani, F. M.; Pastor, A.; Peruzzini, M.; Zanello, P.; Zanobini, F. *J. Am. Chem. Soc.* **1993**, *115*, 2723-2730.

(41) Field, L. D.; George, A. V.; Malouf, E. Y.; Slip, I. H. M.; Hambley, T. W. *Organometallics* **1991**, *10*, 3842.

(42) Tsay, C.; Peters, J. C. *Chem. Sci.* **2012**, *3*, 1313-1318.

(43) Suess, D. L. M.; Peters, J. C. *J. Am. Chem. Soc.* **2013**, *135*, 4938-4941.

(44) Harman, W. H.; Lin, T.-P.; Peters, J. C. *Angew. Chem. Int. Ed.* **2014**, *53*, 1081-1086.

(45) Rubina, M.; Gevorgyan, V. *J. Am. Chem. Soc*. **2001**, *123*, 11107-11108.

Chapter 3. Neutron Diffraction Structure of an $S = ½$ Co–H_2 Adduct

Reproduced in part with permission from
Gunderson, W. A.; Suess, D. L. M.; Fong, H.; Wang, X.; Hoffmann, C. M.; Cutsail, G. E. III, Peters, J. C.; Hoffman, B. M. *Journal of the American Chemical Society* **2014,** *136,* 14998-15009

3.1 Preface

This chapter describes the single crystal neutron diffraction structure of a cobalt-dihydrogen complex, (**TPB**)Co(H_2). The structure is presented in the context of frozen solution ENDOR studies on (**TPB**)Co(H_2), as well as the previously reported iron-dihydrogen complex (**SiP$^{iPr}_3$**)Fe(H_2).[1] The neutron structure clearly shows that (**TPB**)Co(H_2) is a nonclassical dihydrogen adduct, and that the H_2 ligand adopts two preferred orientations in the solid state. This is in contrast to the ENDOR data, which suggest that the H_2 ligand is freely rotating about the Co–H_2 axis.

I am a third author on an article published in *Journal of the American Chemical Society* that describes this work. The other authors are William A. Gunderson, George E. Cutsail III, and Brian M. Hoffman of Northwestern University, Xiaoping Wang and Christina M. Hoffmann of Oak Ridge National Laboratory (ORNL), and Daniel L. M. Suess and Jonas C. Peters of Caltech. Daniel Suess prepared the first set of (**TPB**)Co(H_2) and (**TPB**)Co(D_2) samples for the ENDOR experiments. I was responsible for writing the proposal to secure instrument time at ORNL for single crystal neutron diffraction, synthesizing and growing single crystals for neutron diffraction, and preparing two sets of samples of (**TPB**)Co(H_2), (**TPB**)Co(D_2), and (**TPB**)Co(HD) for ENDOR studies. Xiaoping Wang and I, with assistance from Helen He from ORNL, performed the neutron diffraction experiment and solved the structure, and the two of us along with Christina Hoffmann, Daniel Suess, Jonas Peters, and Brian Hoffman analyzed the neutron structure. William Gunderson and George Cutsail performed the ENDOR

experiments. William Gunderson, George Cutsail, and Brian Hoffman analyzed the ENDOR data.

In this chapter I made a distinction between the ENDOR studies and the neutron structure in order to better reflect my contribution to this topic. In this regard, I have summarized the ENDOR study in the introductory portion of this chapter (section 3.2.1) before presenting the neutron data in the Results and Discussion section 3.3.

3.2 Introduction

Since Kubas's discovery[2] that transition metals can bind dihydrogen (so-called "nonclassical" behavior in contrast to the formation of a "classical" dihydride), there has been extensive work on the structural and electronic features of a number of closed-shell dihydrogen complexes.[3] The binding properties of the dihydrogen ligand, the degree of H–H bond activation, and its propensity to oxidatively add to a metal center are critical features of intermediate steps in a number of important industrial and biological catalytic cycles. For example, an iron center in the cofactor of the molybdenum-containing nitrogenase enzyme is believed to be the site of N_2 binding.[4] It is proposed that prior to N_2 coordination at this iron center two protons are reduced to H_2 as an obligatory component of the catalytic cycle; however, the coordination chemistry and spectroscopic properties of putative intermediate iron-hydride(s) (or -dihydrogen) species remain of interest.[5] Furthermore, there has been great interest in using cobalt complexes as electrocatalytic proton reduction catalysts, but the putative Co^{II}–H_2 intermediate proposed in two of the three competing mechanistic hypotheses has never been observed.[6] Both these iron- and cobalt-dihydrogen intermediates are *open-shell*, which are not amenable to the standard NMR techniques used to characterize *closed-shell* metal-dihydrogen complexes. Whereas a number of diamagnetic closed-shell dihydrogen complexes have been characterized through combined neutron diffraction/scattering, X-ray diffraction (XRD), NMR, and IR studies, examples of open-shell dihydrogen adducts are rare.[7] Thus, the properties and reactivity of thoroughly characterized open-shell transition metal-

dihydrogen complexes are of significant interest in the context of both synthetic and biological chemistry.

Our group recently reported three open-shell metal-dihydrogen complexes. Based on their reactivity, similarities to isoelectronic N_2 and/or CO adducts, as well as spectroscopic and XRD data, these complexes were formulated as nonclassical dihydrogen adducts: S = ½ (**TPB**)Co(H_2)[8] (TPB = B(*o*-$C_6H_4P^iPr_2)_3$), S = ½ (**SiP$^{iPr}_3$**)Fe(H_2)[1] (SiP^{iPr}_3 = [Si(*o*-$C_6H_4P^iPr_2)_3$]$^-$), and S = 1 [(**SiP$^{iPr}_3$**)Fe(H_2)][BAr^F_4][1] (BAr^F_4 = [B(3,5-$(CF_3)_2$-$C_6H_3)_4$]$^-$) (Chart 3.1). Although the hydrogenic ligands in the high quality XRD structures of (**SiP$^{iPr}_3$**)Fe(H_2) and (**TPB**)Co(H_2) cannot be reliably assigned, residual electronic density situated *trans* to the E atom (E = B or Si) was observed in the respective electron density difference map. For the related [(**SiP$^{iPr}_3$**)Fe(H_2)][BAr^F_4], a solid state XRD structure has not been successfully obtained. A method for definitive assignment of the hydrogenic ligands is to use single crystal neutron diffraction.

Chart 3.1 Open-shell M–H_2 adducts of Fe and Co of interest.

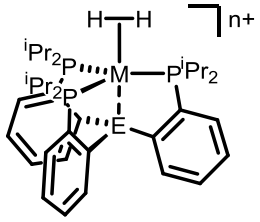

M	E	
Co	B	(**TPB**)Co(H_2)
Fe	Si	(**SiP$^{iPr}_3$**)Fe(H_2)
Fe	Si	[(**SiP$^{iPr}_3$**)Fe(H_2)]$^+$

XRD Structures

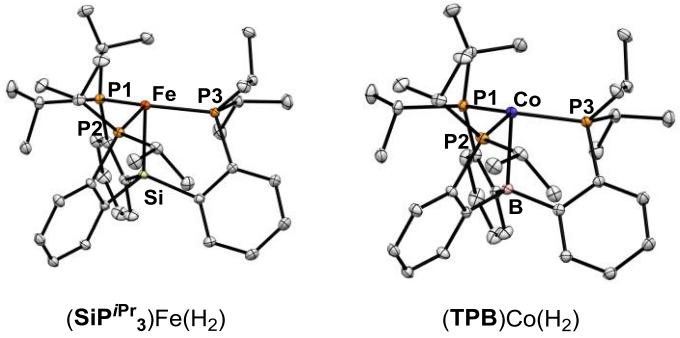

(**SiP$^{iPr}_3$**)Fe(H_2) (**TPB**)Co(H_2)

Neutron diffraction, which relies on the scattering cross section of nuclei rather than the scattering by electrons exploited by XRD, is ideal for determining the atomic distances between light atoms such as hydrogen. Single crystal neutron diffraction was critical in confirming the assignment of Kubas's nonclassical W−H_2 complex, $(CO)_3(PCy_3)_2W(H_2)$ (Figure 3.1),[9-10] and the technique has been used to characterize many other dihydrogen, dihydride, and polyhydride complexes since.[3,11] In the decades since Kubas's discovery, ^{1}H NMR spectroscopy[12-14] has been an important spectroscopic technique for characterizing and definitively assigning M−H_2 adducts, making neutron diffraction largely unnecessary. However, the NMR techniques are only amenable to diamagnetic species and not suitable for paramagnets such as (**TPB**)Co(H_2), (**SiP$^{iPr}_3$**)Fe(H_2), and [(**SiP$^{iPr}_3$**)Fe(H_2)][BAr$^F_4$]. Other pieces of data such as vibrational spectroscopy and reactivity, while informative, are not diagnostic. This leaves neutron diffraction as one of the few techniques for unequivocal assignment of M−H_2 adducts in paramagnetic complexes. Prior to this study, the neutron diffraction structure of a paramagnetic M−H_2 species had never been reported.

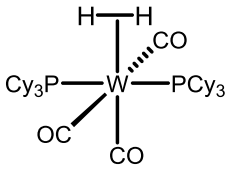

Figure 3.1 Nonclassical W−H_2 adduct $(CO)_3(PCy_3)_2W(H_2)$.

For non-integer spin species, ENDOR (electron nuclear double resonance) spectroscopy can also be used to study M−H_2 species. This is because ENDOR spectroscopy, which is a combined EPR-NMR technique, can resolve coupling between the unpaired electron and the

hydrogenic ligands, providing valuable information about the bonding and structure of these complexes.[15] For the S = ½ species (**SiP$^{iPr}_3$**)Fe(H_2) and (**TPB**)Co(H_2), this technique can therefore provide informative data on the nature of the hydrogenic ligand (H_2 versus dihydride), as well as on the dynamics of the hydrogenic ligand. Indeed, an ENDOR study on (**SiP$^{iPr}_3$**)Fe(H_2) by our collaborators in the Hoffman group at Northwestern University corroborated the assignment of (**SiP$^{iPr}_3$**)Fe(H_2) as a nonclassical H_2 adduct in frozen solution at 2 K.[1] Furthermore, the 2-D field-frequency ENDOR data suggested that the H_2 ligand tunnels/"hops" among localized states that are each parallel to the Fe–P bond vectors (see section 3.2.1).

ENDOR spectroscopy is complementary to single crystal neutron diffraction for the study of non-integer spin M−H_2 species. Whereas neutron diffraction probes static solid state molecular structures, ENDOR spectroscopy probes molecular structure and dynamics, such as the rotation of an H_2 ligand. In this study, our collaborators at Northwestern studied (**TPB**)Co(H_2) with ENDOR spectroscopy. The results show that the dihydrogen ligand is a free-rotor, with nearly unhindered rotation about the Co−H_2 axis in solution. This is in contrast to the localized H_2 orientations found in the solid state, single crystal neutron diffraction structure, and also differs from the tunneling behavior of the H_2 ligand in (**SiP$^{iPr}_3$**)Fe(H_2).

This chapter will first summarize the findings and conclusions from the ENDOR studies.[i] The single crystal neutron diffraction structure for (**TPB**)Co(H_2) will then be presented and discussed in the context of the ENDOR results. Neutron diffraction data for (**SiP$^{iPr}_3$**)Fe(H_2) has

[i] For a thorough discussion of the ENDOR results, including a quantum mechanical description of H_2 rotation, see ref 21.

also been collected, but due to the presence of a significant amount of impurities, conclusions regarding the H_2 ligand in this complex cannot be reliably drawn.

3.2.1 Collaborative ENDOR Studies

(**TPB**)Co(H_2) and (**SiP$^{iPr}_3$**)Fe(H_2) have the same orbitally degenerate ^{2}E ground state, both having triply occupied, degenerate $d_{xy}/d_{x^2-y^2}$ frontier orbitals (Figure 3.2). Yet the H_2 ligands in (**TPB**)Co(H_2) and (**SiP$^{iPr}_3$**)Fe(H_2) exhibit distinct behavior—the H_2 ligand undergoes nearly free rotation in (**TPB**)Co(H_2), whereas the H_2 ligand in (**SiP$^{iPr}_3$**)Fe(H_2) tunnels among local energy minima.[1] As the following discussion will show, these differences are attributed to i) structural distortions of the two complexes arising from the pseudo-Jahn-Teller effect, ii) π-backbonding, and iii) crystal-packing forces and/or the molecular environment.

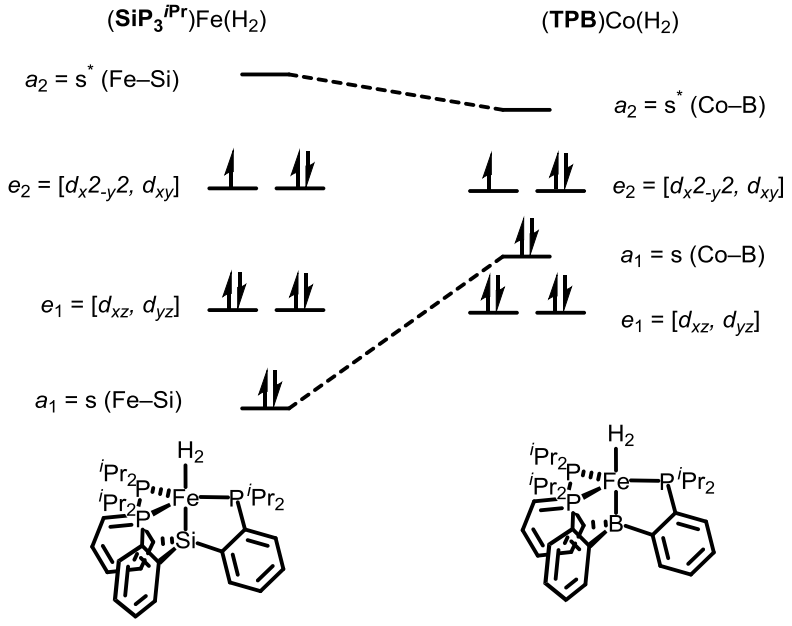

Figure 3.2 Frontier molecular orbital diagram for (**SiP$^{iPr}_3$**)Fe(H_2) and (**TPB**)Fe(H_2). The relative ordering of the fully-occupied orbitals may vary.

^{1}H and ^{2}H ENDOR spectra were collected at 2 K on frozen solution samples of (**TPB**)Co(H_2), (**TPB**)Co(D_2), and (**TPB**)Co(HD). The Q-band (35 GHz) pulsed ^{1}H ENDOR spectrum of (**TPB**)Co(H_2) is markedly different from the ^{1}H and ^{2}H ENDOR spectra of (**TPB**)Co(D_2) and (**TPB**)Co(HD) (Figure 3.3C). Whereas (**TPB**)Co(D_2) exhibits a hyperfine feature in the ^{2}H ENDOR spectrum that is due to coupling to the D_2 ligand, and (**TPB**)Co(HD) exhibits the same coupling associated with the HD ligand in both the ^{1}H and ^{2}H ENDOR spectra, the all $^{1}H_2$ isotopologue (**TPB**)Co(H_2) does not exhibit a hyperfine feature associated with coupling to the H_2 ligand. By appropriately adjusting for the different gyromagnetic ratios of ^{2}H and ^{1}H, the ^{2}H ENDOR signal corresponds to a hyperfine feature of A(^{1}H) = 20.8 MHz, which is the same hyperfine coupling frequency observed in the ^{1}H ENDOR spectrum for (**TPB**)Co(HD) (A(^{1}H) = 20.8 MHz).

The presence of ^{1}H ENDOR signals for the HD ligand in (**TPB**)Co(HD), the presence of ^{2}H ENDOR signals for the respective HD and D_2 ligands in (**TPB**)Co(HD) and (**TPB**)Co(D_2), but the absence of ^{1}H ENDOR signals for the H_2 ligand in (**TPB**)Co(H_2), are suggestive of exchange of the two H atoms of the H_2 ligand through rotation about the Co–H_2 axis in (**TPB**)Co(H_2). This exchange is subject to constraints on the nuclear wave function imposed by the Pauli exclusion principle.[16-17] For a homodiatomic molecule such as H_2, the Pauli exclusion principle requires that the total nuclear spin state (I_{tot}), which is a product of spatial rotational (*Rot*) and spin wave functions, must have definite parity with respect to exchange. For hydrogen (^{1}H), which is a ferimon (I = ½), the total nuclear wave function must be antisymmetric (AS) to exchange. For deuterium (^{2}H) which is a boson (I = 1), the total nuclear

wave function must be symmetric (S) to exchange. The *Rot* ground state for homodiatomic such as H_2 is symmetric to exchange (S in Figure 3.3A), and therefore, the spin functions of the ^{1}H in H_2 must be antisymmetric with antiparallel nuclear spins (i.e., I = ½ and -½) and I_{tot} = 0. This state does not have allowed ENDOR transitions, which is in agreement with the absence of ^{1}H ENDOR signals for (**TPB**)Co(H_2). For a homodiatomic such as D_2, the *Rot* ground state is also symmetric (S, Figure 3.3B). The total nuclear wave function for D_2 (I = 1 for ^{2}H) is I_{tot} = 0,1, or 2. Only I_{tot} = 2 is symmetric to exchange, and it therefore must be associated with the symmetric rotational ground state. This spin state does have allowed

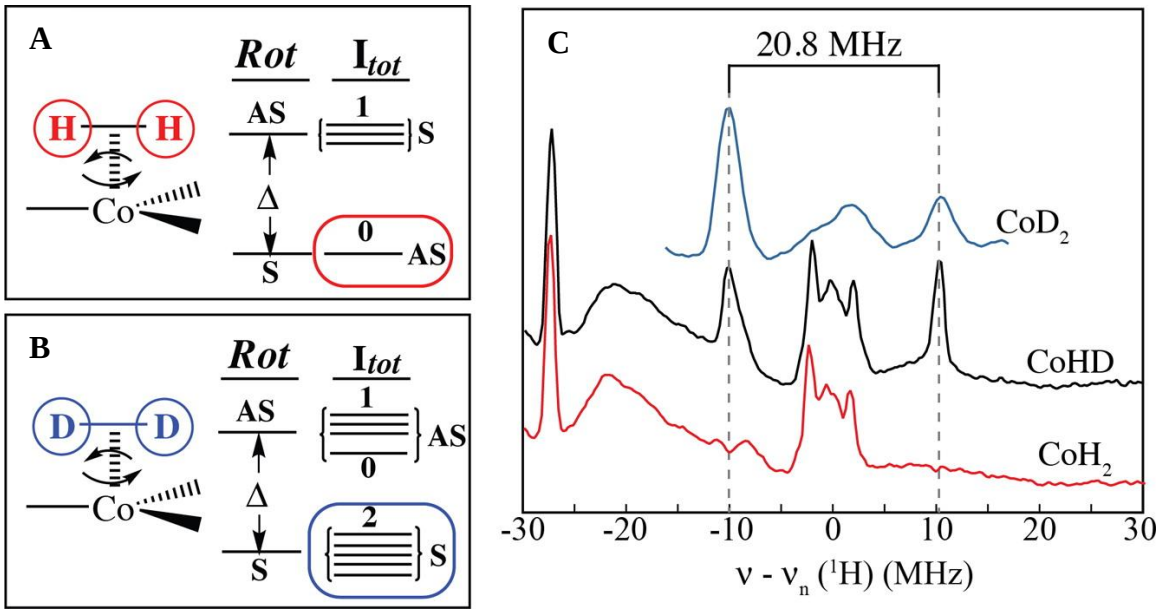

Figure 3.3 Q-band pulsed ENDOR spectra and rotational and nuclear spin states. (A) and (B) Spatial rotational (*Rot*) energy levels and corresponding total nuclear spin (I_{tot}) for (**TPB**)Co(H_2) and (**TPB**)Co(D_2), respectively. (C) ^{1}H ENDOR spectra for (**TPB**)Co(H_2) (red) and (**TPB**)Co(HD) (black), and ^{2}H ENDOR spectra for (**TPB**)Co(D_2) (blue) at 2 K . The ^{1}H hyperfine of 20.8 MHz is marked. The frequency scale of the ^{2}H (**TPB**)Co(D_2) spectra has been scaled to match the ^{1}H frequency.

ENDOR transitions, which is in agreement with the observation of ^{2}H ENDOR signals for (**TPB**)Co(D_2). Because ^{2}H and ^{1}H in HD are inequivalent, HD rotation in (**TPB**)Co(HD) is not subject to Pauli principle constraints; both ^{1}H and ^{2}H ENDOR transitions are allowed.

The excited *Rot* state (Figure 3.3A)of (**TPB**)Co(H_2) can exhibit an ^{1}H ENDOR response, because it must correspondingly have a symmetric nuclear spin state with $I_{tot} = 1$. However, the absence of a ^{1}H ENDOR signal at (**TPB**)Co(H_2) indicates that this state is negligibly occupied at 2 K and that the energy difference (Δ) between the ground and this first excited state must be greater than 7 cm^{-1}.

The quantum mechanical model for H_2 rotation in a three-fold symmetric complex such as (**TPB**)Co(H_2) predicts that the H_2 ligand will rotate about the M–H_2 axis nearly unhindered. This is because for H_2 rotation in a C_3 symmetric environment, the rotation occurs on a potential energy surface of C_6 symmetry (Figure 3.4B). In this symmetry, calculations show that the rotational barriers have little influence on H_2 rotation. This is in contrast to H_2 rotation about an axis with two-fold symmetry such as $(CO)_3(PCy_3)_2W(H_2)$ (Figure 3.4A), wherein the H_2 rotation is hindered by potential energy barriers and results in the preferential localization of the H_2 ligand.

An alternative way to explain the free rotation of the H_2 ligand in (**TPB**)Co(H_2) and hindered rotation in $(CO)_3(PCy_3)_2W(H_2)$ is to consider the effects of symmetry on π-backbonding to the π-acidic H_2 ligand. π-Backbonding can create a rotational barrier, and the H_2 ligand can favor a particular orientation(s). In $(CO)_3(PCy_3)_2W(H_2)$, the axes of the filled $(d\pi)^4$ of d_{xz} and d_{yz} are parallel to the W–E bond vectors (E = P or C). Because CO is a better

π-acceptor than PCy_3 (and H_2), the π-acidic H_2 ligand favors aligning parallel to the W–P bond vectors where it can better compete for π-backbonding with the slightly π-acidic phosphines. This is illustrated on the potential energy surface in Figure 3.4A, where H_2 favors alignment in parallel to the W–P bond vectors. The H atoms of the H_2 ligand tunnel among the two positions along the W–P bond vectors.[18-19] In C_3 symmetry, the electron density of the e_2 set of degenerate orbitals that participate in π-backbonding are cylindrically symmetric, and therefore π-backbonding cannot generate a rotational barrier. This leads to unhindered rotation of H_2 in (**TPB**)Co(H_2).

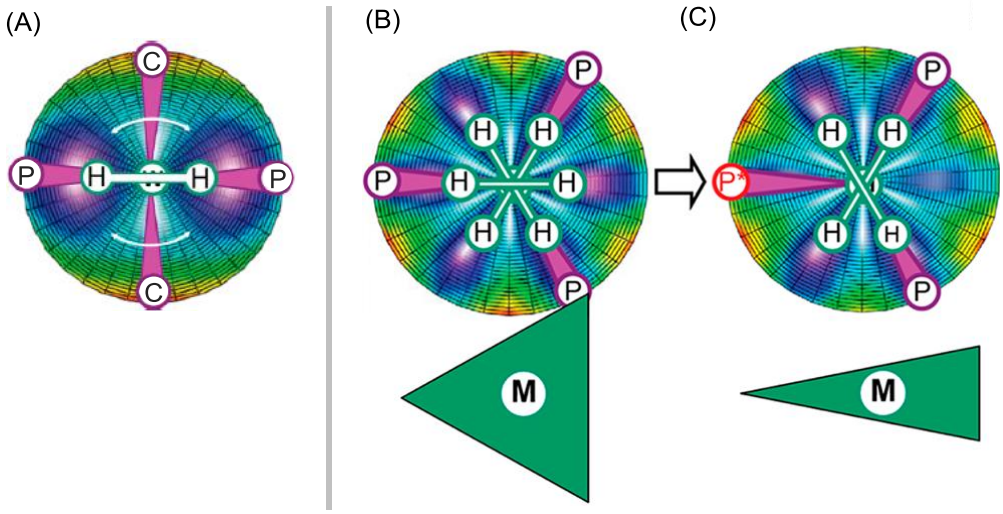

Figure 3.4 Potential energy surfaces for H_2 rotation. (A) H_2 rotation in C_2 symmetric $(CO)_3(PCy_3)_2W(H_2)$. (B) Representation of H_2 rotation on a C_6 potential energy surface, wherein the MP_3 plane forms an equilateral triangle, e.g., in (**TPB**)Co(H_2) in frozen solution. (C) Distortion of the MP_3 triangle to an acute isosceles triangle results in potential barrier along one M–P bond vector (red P*) and localization of the H_2 ligand along the two remaining M–P vectors, e.g., in the crystalline state of (**TPB**)Co(H_2) and in (**SiP$^{iPr}_3$**)Fe(H_2).

While the discussion above explains the ENDOR response and free rotor behavior of H_2 in (**TPB**)Co(H_2), it does not explain why (**SiP$^{iPr}_3$**)Fe(H_2) exhibits a ^{1}H ENDOR response, and why the H_2 ligand tunnels among energy minima in (**SiP$^{iPr}_3$**)Fe(H_2) rather that freely rotate. Both complexes have ^{2}E ground states that are subject to symmetry lowering structural distortions through vibronic coupling from the pseudo-Jahn-Teller effect.[20] An analysis of the g-tensors from the EPR spectra of (**SiP$^{iPr}_3$**)Fe(H_2) (**g** = [2.275, 2.064, 2.015]) and (**TPB**)Co(H_2) (**g** = [2.457, 2.123, 2.029]) through the lens of the pseudo-Jahn-Teller effect shows that (**SiP$^{iPr}_3$**)Fe(H_2) is subject to larger vibronic coupling than (**TPB**)Co(H_2).[21] This difference has a large effect on the structural distortions and, therefore, the degree to which H_2 can freely rotate.

The structural distortion, as shown in Figure 3.4, can be envisioned to occur through distortion of the C_3 symmetric MP_3 plane. In an idealized C_3 symmetry, the MP_3 plane can be thought of as an equilateral triangle. In the case of (**TPB**)Co(H_2), it is proposed that a *dynamic* Jahn-Teller effect would maintain free rotation of the H_2 ligand because the distortion of the MP_3 plane is "pseudo-rotating" around the symmetry axis.[20] The coupling of H_2 ligand to this dynamic distortion through π-backbonding would maintain free rotation of the H_2 ligand. In contrast, *static* Jahn-Teller distortion of the MP_3 plane in (**SiP$^{iPr}_3$**)Fe(H_2) generates a barrier to rotation. As the neutron structure will illustrate in section 3.3, one possible distortion results in an acute isosceles triangle for the MP_3 plane, which generates a potential energy surface that contains a single barrier to rotation along the M–P* bond vector (Figure 3.4C). In this scenario, free rotation of the H_2 ligand is quenched, and the energy surface contains two energy minima

for the H_2 ligand. Each of the energy minima are parallel to a M–P bond vector. The hindrance to free rotation of the H_2 ligand means that the ENDOR response is no longer subject to Pauli principle selection rules, thereby allowing for both ^1H and ^2H ENDOR responses, as was observed in (**SiP$^{iPr}_3$**)Fe(H_2).[1] The distortion of the MP_3 plane in (**SiP$^{iPr}_3$**)Fe(H_2) to an isosceles triangle can be seen in the solid state X-ray structure, which shows that the P1–Fe–P3 angle is contracted from the idealized 120 ° to 113 ° (see Table 3.1 in section 3.3.1).

This distortion of the MP_3 plane away from C_3 symmetry also affects the π-backbonding to H_2 from the cylindrically symmetric (in C_3 symmetry) e_2 set of orbitals. The distortion away from C_3 symmetry as described above orients one of the two dπ orbitals (either d_{xz} or d_{yz}) towards the "open" M–P* bond vector, enhancing π-backbonding to this P* donor arm. This outcome of this distortion and enhanced M–P* π-backbonding, according to calculations, forces the H_2 ligand along the two other M–P bond vectors (Figure 3.4C).

The stronger π-backbonding abilities for the iron complex compared to the cobalt complexes can also explain the differences in H_2 rotation between (**TPB**)Co(H_2) and (**SiP$^{iPr}_3$**)Fe(H_2). The differences in π-backbonding abilities can be seen in the previously reported (**SiP$^{iPr}_3$**)Fe(N_2)[22] and (**TPB**)Co(N_2)[8] complexes, which are isoelectronic to (**SiP$^{iPr}_3$**)Fe(H_2) and (**TPB**)Co(H_2), respectively. The substantial differences in the N–N stretching frequencies (2008 cm^{-1} for (**SiP$^{iPr}_3$**)Fe(N_2) versus 2089 cm^{-1} for (**TPB**)Co(N_2)) and N–N bond lengths (1.125 Å for (**SiP$^{iPr}_3$**)Fe(N_2) versus 1.062 Å for (**TPB**)Co(N_2)) indicate that the M–N_2 π-backbonding is greater, and thus the N–N bond more activated, in (**SiP$^{iPr}_3$**)Fe(N_2) than (**TPB**)Co(N_2). The

similar π-accepting abilities of N_2 and H_2[23] mean that these trends should extend to (**SiP$^{iPr}_3$**)Fe(H_2) and (**TPB**)Co(H_2) as well.

Thus, the structural distortion and greater π-backbonding abilities for the (**SiP$^{iPr}_3$**)Fe(H_2) complex compared to (**TPB**)Co(H_2) explain why the H_2 ligand in (**SiP$^{iPr}_3$**)Fe(H_2) tunnels/hops between potential energy minima, while the H_2 ligand in (**TPB**)Co(H_2) freely rotates in frozen solution at 2 K. To probe the structure of (**TPB**)Co(H_2) in the solid state, I collected the single crystal neutron diffraction structure of (**TPB**)Co(H_2). The neutron structure of (**TPB**)Co(H_2) confirms the intact H–H bond of the H_2 ligand and corroborates the conclusion that structural distortions quench free rotor behavior.

3.3 Results and Discussion

*3.3.1 Neutron Structure of (**TPB**)Co(H_2)*

The single crystal neutron diffraction structure of (**TPB**)Co(H_2) has been determined at 100 K, at which temperature any structural changes upon cooling in general have produced a limiting low-temperature structure that is appropriate for comparisons with the ENDOR measurement at still lower temperature. The high-resolution neutron structure of (**TPB**)Co(H_2) clearly resolves the presence of a side-on bound H_2 ligand to Co that is positioned *trans* to boron (Figure 3.5). Thus, the structure confirms the initial assignment,[8] and the assignment based on the ENDOR data discussed above, of (**TPB**)Co(H_2) as a cobalt-dihydrogen adduct

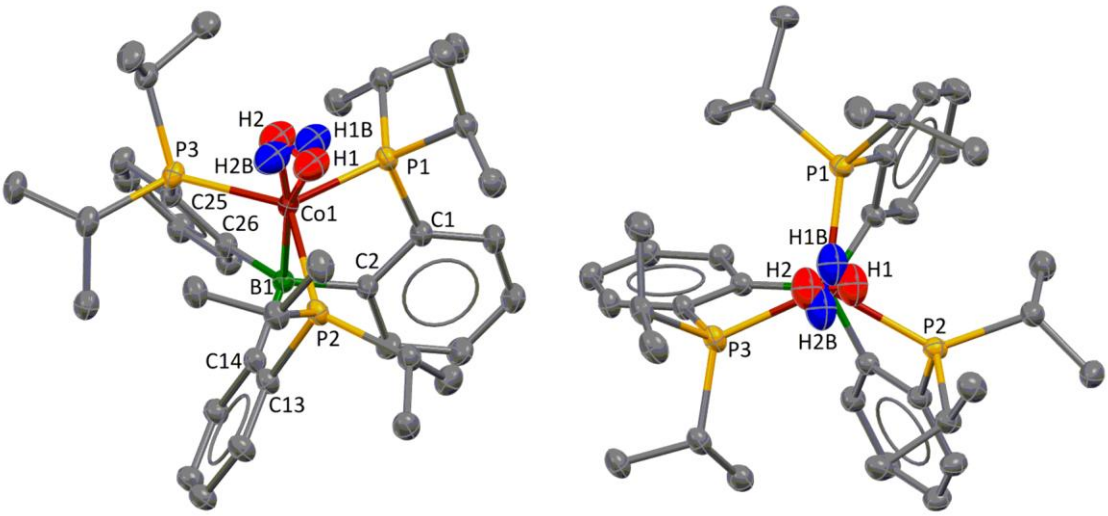

Figure 3.5. Single crystal neutron diffraction structure of (**TPB**)Co(H_2). (left) The disordered H_2 ligand is shown in red and blue for the major and minor components, respectively. (right) View down the Co1–B1 vector emphasizing the near parallel orientations of the disordered H_2 ligand with the B1-C26 (associated with the major component of the disordered H_2 ligand) and P1-Co1 bond (associated with the minor component of the disordered H_2 ligand). Ellipsoids are shown at the 50 % probability level. Hydrogen atoms on the isopropyl and phenyl groups are omitted for clarity.

rather than a cobalt-dihydride complex. The H_2 ligand is disordered over two positions—the major component of disorder has a 68.2 % site occupancy. A second component of the disordered H_2 was refined to a site occupancy of 25.2 %.[ii] The two orientations of the H_2 ligand can be described as each being associated with a Co–P bond vector, presumably a reflection of π-backbonding from filled d orbitals of Co to the empty σ* orbital of H_2,[3,24-25] although being somewhat skewed with respect to them, by *ca.* 21.2° and *ca.* 8° for the major

[ii] The remaining 6.8 % nuclear density was modeled as a bromide ligand at 2.383(13) Å away from the Co center, situated *trans* to B atom, and is attributed to residual Co–Br starting material.

and minor disordered components, respectively. The large degree of skewing of the major component of the H_2 ligand (H1 and H2) from the Co1–P3 places it in near parallel alignment with the B1-C26 bond vector (skewed by 5.7°). The H–H bond distances for both H_2 moieties are identical (0.834(6) and 0.83(2) Å) and elongated from the 0.74 Å bond length[3] of free H_2. These distances are similar to those found in other metal-dihydrogen complexes characterized by neutron diffraction (0.81 – 0.92 Å)[3,11,18] and closely match those for two iron-dihydrogen adducts (0.81 - 0.82 Å).[26-27]

Table 3.1 Selected bond angles and distances for (**SiP$^{iPr}_3$**)Fe(H_2) and (**TPB**)Co(H_2) determined by X-ray and neutron diffraction.

	X-ray		**Neutron**
	(**SiP$^{iPr}_3$**)Fe(H_2)[a]	(**TPB**)Co(H_2)[b]	(**TPB**)Co(H_2)
H1–H2 (Å)			0.834(6) / 0.83(2)[c]
M–H1 (Å)			1.659(4) / 1.672(7)[c]
M–H2 (Å)			1.664(4) / 1.671(7)[c]
M–P1 (Å)	2.2442(9)	2.2412(3)	2.241(3)
M–P2 (Å)	2.260(1)	2.2650(3)	2.280(3)
M–P3 (Å)	2.2631(1)	2.2750(3)	2.262(3)
M–E (Å)	2.254(1)	2.2800(1)	2.287(2)
H1–M–H2 (°)			29.03(11) / 28.91(14)[c]
P1–M–P3 (°)	113.31(3)	119.00(1)	119.40(12)
P1–M–P2 (°)	118.07(3)	110.97(1)	111.92(11)
P2–M–P3 (°)	122.36(4)	124.97(1)	123.93(11)

E = Si or B [a]See ref 1. [b]See ref 8. [c]Metrics for the major and minor components, respectively, of the disordered H_2 ligand.

The neutron structure shows a deviation of the P–Co–P angles away from the 120° of the idealized C_3 symmetry of the Co–P plane (Table 3.1), as was also observed in the X-ray diffraction structures of (**TPB**)Co(H_2) and the closely related complex, (**TPB**)Co(N_2)[8]: the P1–Co–P3 angle is more acute than the other two P–Co–P angles, leaving P2 as the unique P*-atom at the apex of the isosceles triangle (c.f. Figure 3.4). The same type of structural distortion was seen in the solid state X-ray diffraction structure of (**SiP$^{i\mathrm{Pr}}_3$**)Fe(H_2). The distortion can be attributed to Jahn-Teller distortion in the solid state as well as crystal packing and other inter- and intramolecular forces, as is illustrated in the electron density isosurface of the solid state structure of Co–H_2 (Figure 3.6).[28]

The isosurface shows that the disordered H_2 ligand is located in the blue-colored triangular cavity and is in close contact with three separate methyl hydrogen atoms from three isopropyl groups on the TPB ligand (Figure 3.6). The H_2 orientation with higher occupancy may be favored because it has longer H ··· H interactions between the H_2 ligand and hydrogen atoms of adjacent methyl groups: the closest H ··· H contacts from the neutron structure are 2.174(6) Å and 2.096(14) Å for the major and minor components of the H_2 ligand, respectively. These close contacts are likely not present in frozen solutions, where packing forces are not in play. Such crystal-packing influences on H_2 rotation have been discussed elsewhere.[iii,19]

A single crystal neutron diffraction experiment for (**SiP$^{i\mathrm{Pr}}_3$**)Fe(H_2) was also performed. However, the neutron structure exhibited significant disorder arising from multiple impurities

[iii] The unequal occupation of H_2 at the two sites is also predicted by applying an additional, small out-of-registry potential in the modeling of the potential energy surface.

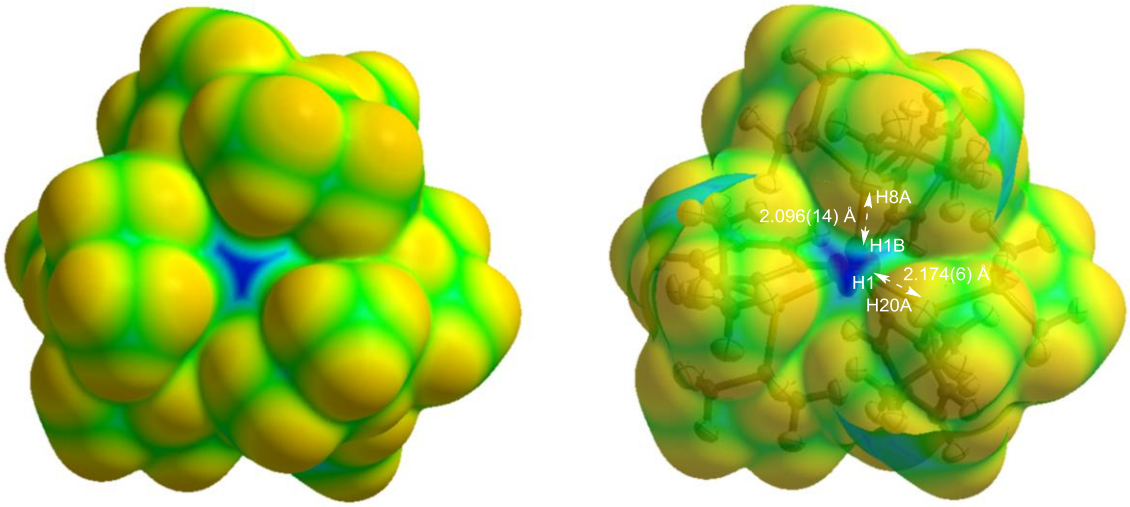

Figure 3.6 Plot of the isosurface of the promolecule electron density of (**TPB**)Co(H_2). (left) Isosurface of electron density of (**TPB**)Co(H_2) with the dihydrogen ligand removed. The isovalue of 0.0020e au^{-3} used in the plot is comparable to the expected van der Waals radii. (right) A translucent view of the same isosurface showing the disordered dihydrogen ligand located in the blue colored triangular cavity.

in the crystal: the desired (**SiP$^{iPr}_3$**)Fe(H_2) accounted for *ca.* 45 % and the previously reported Fe^{II}-hydride-dihydrogen complex (**SiP$^{iPr}_3$**)Fe(H_2)(H)[29] accounted for another *ca.* 20 %. The remaining 35 % impurity was assigned to chloride from the (**SiP$^{iPr}_3$**)FeCl starting material. The significant amounts of impurities, particularly of the (**SiP$^{iPr}_3$**)Fe(H_2)(H), wherein the H_2 ligand residues in the same coordination site as the H_2 ligand in (**SiP$^{iPr}_3$**)Fe(H_2), rendered this structure inconclusive with respect to the nature of the H_2 ligand in (**SiP$^{iPr}_3$**)Fe(H_2). For a figure of the structure, see Figure A2.1 in Appendix 2.

3.3.2 Comparisons with the ENDOR Data

The localization of the H_2 ligand among two preferred orientations in the solid state neutron structure of (**TPB**)Co(H_2) is distinct from the free rotor behavior of the H_2 ligand suggested by the frozen solution ENDOR data, but it agrees with the predicted localization for the H_2 ligand upon distortion of the MP_3 plane. The ENDOR results presented in section 3.2.1 showed that static distortions of the MP_3 plane and competitive π-backbonding between the π-acidic phosphines and H_2 ligand can lead to preferential alignment of the H_2 ligand along two M–P bond vectors (Figure 3.4C), as was suggested by ENDOR results for the frozen solution samples of (**SiP$^{iPr}_3$**)Fe(H_2). It is evident from the neutron structure for (**TPB**)Co(H_2) that in the solid, crystalline state the MP_3 plane is also distorted similarly to the frozen solution structure of (**SiP$^{iPr}_3$**)Fe(H_2) (Table 3.1). Such a distortion in the solid state, as well as additional forces created by the solid, crystalline state molecular environment about the H_2 ligand's coordination sphere, serve to quench free rotation of the H_2 ligand.

The P1–Co1–P2 angle in the solid state structure of (**TPB**)Co(H_2) is contracted from the 120° of an idealized C_3 symmetric MP_3 core to 111° (Table 3.1), with the MP_3 core best described as an acute, isosceles triangle, as shown in Figure 3.4. It was predicted that this geometric distortion quenches free rotor behavior and localizes the H_2 ligand among two preferred orientations, where each H_2 unit of the disorder lies in parallel with a M−P bond vector, leaving the third M−P* bond vector as a non-preferred orientation. Indeed, this is observed in the neutron structure of (**TPB**)Co(H_2). The H_2 ligand is localized in two orientations that are each associated with the Co−P3 and Co−P1 bond vectors, respectively.

The Co–P2 bond vector is the non-preferred orientation. To illustrate the correspondence between the neutron structure and the potential energy surface, the core of the structure of (**TPB**)Co(H_2) can be overlaid with the potential energy surface, which was originally presented in Figure 3.4C, to give Figure 3.7. The potential energy surface is oriented so as to maximize the overlap of the two H_2 orientations with energy minima. The figure illustrates the correspondence between the potential energy surface predicted by quantum mechanics and the neutron diffraction determined localization of the H_2 ligand within these potential energy minima.

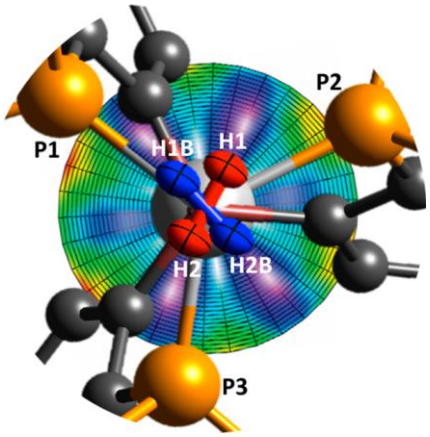

Figure 3.7 Overlay of the core of the (**TPB**)Co(H_2) neutron structure with the potential energy surface for H_2 rotation upon distortion of the MP_3 core, emphasizing the two preferred orientations of the H_2 ligand.

The H_2 ligand also does not occupy each of the two preferred orientation equally: H1–H2 has occupancy of 68.2 %, while the H1B–H2B has occupancy of 25.2 %. H1–H2 and H1B–H1B are skewed from the M–P bond vectors by *ca.* 21° and *ca.* 8°, respectively. The deviation from the predicted structure can be explained in part with the isosurface shown in

Figure 3.6, which shows that the H_2 ligand is in close contact with three separate methyl hydrogen atoms from the three isopropyl group of the TPB ligand. The higher occupancy of H1–H2 may be favored because it has the longest H ··· H close-contact distance of 2.174 Å, compared to the to the significantly shorter H ··· H close-contact distance of 2.096 Å for the lower occupancy H1B–H2B. These close contacts are likely not present in frozen solution, where packing forces are not in play and also contribute to quenching of the free rotation of the H_2 ligand.

3.4 Conclusions

The neutron diffraction determined H–H distance of 0.83 Å is evidence that (**TPB**)Co(H_2) is a nonclassical H_2 adduct. Comparison of the solid state neutron structure to frozen solution ENDOR data reveals that the rotational dynamics of the H_2 ligand are very different in the solid state versus frozen solutions. Whereas the H_2 ligand is a free-rotor in frozen solution, arising from H_2 residing in an environment of C_3 symmetry, the solid state structure reveals that H_2 is localized among two preferred orientations. The quenching of free-rotation for the H_2 ligand in the solid state is attributed to structural distortions and crystal packing forces that generate barriers to free rotation of the H_2 ligand. The neutron structure of (**TPB)**Co(H_2) exhibits exactly what is observed by ENDOR for frozen solution samples of (**SiP$^{iPr}_3$**)Fe(H_2). The contrast between the solid state data and frozen solution data illustrates how single crystal neutron diffraction and ENDOR can be used as complementary tools for the study of molecular dihydrogen complexes in the solid and solution states, respectively.

3.5 Experimental Section

3.5.1 Sample Preparation

Samples for EPR/ENDOR studies were prepared using a standard glovebox or Schlenk techniques. (**TPB**)Co(H_2), (**TPB**)Co(D_2), and (**TPB**)Co(HD) were prepared according to literature procedures.[8] THF, 2-Me-THF, toluene, HMDSO, and methylcyclohexane were rigorously dried by stirring over Na metal for several days, followed by filtration through a pad of activated alumina. HD gas was generated by the slow addition of D_2O into $LiAlH_4$. Q-band ENDOR tubes were charged with the (**TPB**)Co(H_2), (**TPB**)Co(D_2), and (**TPB**)Co(HD) solutions under an atmosphere of the respective dihydrogen isotopomer.

(**TPB**)Co(H_2) crystals of suitable size for single crystal neutron diffraction were grown under 1 atm of H_2 in a J-Young NMR tube according to the following procedure. A suspension of (**TPB**)Co(H_2) in 2:1 HMDSO:methylcyclohexane at room temperature (RT) was dissolved by heating to 90 °C in an oil bath. Homogeneity of the solution is critical to growing large crystals suitable for neutron diffraction. The sample was then allowed to cool to RT in the oil bath, which was left undisturbed for three days, yielding large yellow crystals of (**TPB**)Co(H_2).

3.5.2 Neutron Diffraction

Single crystal neutron diffraction data were measured on the TOPAZ instrument at the Spallation Neutron Source at Oak Ridge National Laboratory, in the wavelength-resolved time-of-flight Laue diffraction mode using wavelengths in the range 0.4 – 3.5 Å.[30] A rod-shaped crystal of (**TPB**)Co(H_2) with the dimensions of $0.42 \times 0.60 \times 1.20$ mm^3 was mounted onto the tip of a polyimide capillary with fluorinated grease in a nitrogen glove box, and

transferred onto the TOPAZ goniometer for data collection at 100 K. To ensure good coverage and redundancy, data were collected using 26 crystal orientations optimized with CrystalPlan software.[31] Each orientation was measured for approximately 5.9 h.

The integrated raw Bragg intensities were obtained using the 3-D reciprocal *Q*-space integration method in Mantid,[32] where $Q = 2\pi/d = 4\pi(\sin\theta)/\lambda$. The peaks from (**TPB**)Co(H_2) were found to be triplets in Q-space within less than 0.15 $Å^{-1}$ radii. Bragg peaks from the major component were used for determination of orientation matrix for the (**TPB**)Co(H_2) crystal. Peak integration was performed accordingly using a radius of 0.15 $Å^{-1}$ to include contributions from all three components. Data reduction for each sample, including neutron TOF spectrum, detector efficiency, and absorption corrections, was carried out with the ANVRED2 program.[33] The reduced data were saved in SHELX HKLF2 format in which the wavelength is recorded separately for each individual reflection, and not merged as a consequence of this saved format. The initial structural model used the unit cell parameters and non-hydrogen atom positions from the single-crystal XRD experiment measured at 100 K. The hydrogen atoms were found from nuclear difference Fourier map of the neutron data, and refined anisotropically using SHELXL-97[34] in WinGX.[35]

The dihydrogen ligand was found to be disordered in two positions with the site occupancy factors refined to 68.2 % and 25.2 %, respectively, for the major and minor components. The remaining 6.6 % nuclear density was modeled as a bromide ligand at 2.383(13) Å away from the Co center (*trans* to the boron) and is attributed to residual (**TPB**)CoBr starting material. The neutron structure was validated with Platon and the IUCr online checkcif program. The

following is a list of programs used: orientation matrix from live neutron event data, ISAW Event Viewer; data collection strategy, CrystalPlan; Data collection, SNS PyDas; data reductions, Mantid; absorption correction, ANVRED2; structural refinement, SHELXL-97;[34] promolecule isosurface plots, CrystalExplore.[36]

3.6 Cited References

(1) Lee, Y.; Kinney, R. A.; Hoffman, B. M.; Peters, J. C. *J. Am. Chem. Soc.* **2011**, *133*, 16366-16369.

(2) Kubas, G. J. *J. Chem. Soc., Chem. Commun.* **1980**, 61-62.

(3) Kubas, G. J. *Chem. Rev.* **2007**, *107*, 4152-4205.

(4) Seefeldt, L. C.; Dance, I. G.; Dean, D. R. *Biochemistry* **2004**, *43*, 1401-1409.

(5) Hoffman, B. M.; Lukoyanov, D.; Yang, Z.-Y.; Dean, D. R.; Seefeldt, L. C. *Chem. Rev.* **2014**, *114*, 4041-4062.

(6) Dempsey, J. L.; Brunschwig, B. S.; Winkler, J. R.; Gray, H. B. *Acc. Chem. Res.* **2009**, *42*, 1995-2004.

(7) Proposed nonclassical H_2 binding in a paramagnetic metal complex: (a) Hetterscheid, D. G. H.; Hanna, B. S.; Schrock, R. R. *Inorg. Chem.* **2009,** *48*, 8569-8577; (b) Kinney, R. A.; Hetterscheid, D. G. H.; Schrock, R. R.; Hoffman, B. M. *Inorg. Chem.* **2010,** *49*, 704-713; (c) Bart, S. C.; Lobkovsky, E.; Chirik, P J. *J. Am. Chem. Soc.* **2004,** *126*, 13794-13807; (d) Baya, M.; Houghton, J.; Daran, J.-C.; Poli, R.; Male, L.; Albinati, A.; Gutman, M. *Chem.-Eur. J.* **2007,** *13*, 5347-5359.

(8) Suess, D. L. M.; Tsay, C.; Peters, J. C. *J. Am. Chem. Soc.* **2012**, *134*, 14158-14164.

(9) Kubas, G. J.; Ryan, R. R.; Swanson, B. I.; Vergamini, P. J.; Wasserman, H. J. *J. Am. Chem. Soc.* **1984**, *106*, 451-452.

(10) Kubas, G. J.; Unkefer, C. J.; Swanson, B. I.; Fukushima, E. *J. Am. Chem. Soc.* **1986**, *108*, 7000-7009.

(11) Morris, R. H. *Coord. Chem. Rev.* **2008**, *252*, 2381-2394.

(12) Desrosiers, P. J.; Cai, L.; Lin, Z.; Richards, R.; Halpern, J. *J. Am. Chem. Soc.* **1991**, *113*, 4173-4184.

(13) Maltby, P. A.; Schlaf, M.; Steinbeck, M.; Lough, A. J.; Morris, R. H.; Klooster, W. T.; Koetzle, T. F.; Srivastava, R. C. *J. Am. Chem. Soc.* **1996**, *118*, 5396-5407.

(14) Heinekey, D. M.; van Roon, M. *J. Am. Chem. Soc.* **1996**, *118*, 12134-12140.

(15) Hoffman, B. M. *Proc. Natl. Acad. Sci. U. S. A.* **2003**, *100*, 3575-3578.

(16) Farkas, A. *Orthohydrogen, Parahydrogen, and Heavy Hydrogen*; University Press: New York, 1935.

(17) McConnell, H. M. *J. Chem. Phys.* **1958**, *29*, 1422-1422.

(18) Kubas, G. J.; Burns, C. J.; Eckert, J.; Johnson, S. W.; Larson, A. C.; Vergamini, P. J.; Unkefer, C. J.; Khalsa, G. R. K.; Jackson, S. A.; Eisenstein, O. *J. Am. Chem. Soc.* **1993**, *115*, 569-581.

(19) Eckert, J.; Kubas, G. J. *J. Phys. Chem.* **1993**, *97*, 2378-2384.

(20) Bersuker, I. B. *Chem. Rev.* **2013**, *113*, 1351-1390.

(21) Gunderson, W. A.; Suess, D. L. M.; Fong, H.; Wang, X.; Hoffmann, C. M.; Cutsail, G. E. I.; Peters, J. C.; Hoffman, B. M. *J. Am. Chem. Soc.* **2014**, *136*, 14998-15009.

(22) Whited, M. T.; Mankad, N. P.; Lee, Y.; Oblad, P. F.; Peters, J. C. *Inorg. Chem.* **2009**, *48*, 2507-2517.

(23) Morris, R. H.; Earl, K. A.; Luck, R. L.; Lazarowych, N. J.; Sella, A. *Inorg. Chem.* **1987**, *26*, 2674-2683.

(24) Kubas, G. J. *J. Organomet. Chem.* **2014**, *751*, 33-49.

(25) Eckert, J. *Spectrochim. Acta, Part A* **1992**, *48*, 363-378.

(26) Van der Sluys, L. S.; Eckert, J.; Eisenstein, O.; Hall, J. H.; Huffman, J. C.; Jackson, S. A.; Koetzle, T. F.; Kubas, G. J.; Vergamini, P. J.; Caulton, K. G. *J. Am. Chem. Soc.* **1990**, *112*, 4831-4841.

(27) Ricci, J. S.; Koetzle, T. F.; Bautista, M. T.; Hofstede, T. M.; Morris, R. H.; Sawyer, J. F. *J. Am. Chem. Soc.* **1989**, *111*, 8823-8827.

(28) Promolecule is the sum of electron density distribution of spherical atoms within the same molecule. see McKinnon, J. J.; Spackman, M. A.; Mitchell, A. S. *Acta Crystallogr., Sect. B: Struct. Sci., Cryst. Eng. Mater.* **2004,** *60*, 627-668.

(29) Fong, H.; Moret, M.-E.; Lee, Y.; Peters, J. C. *Organometallics* **2013**, *32*, 3053-3062.

(30) Jogl, G.; Wang, X.; Mason, S. A.; Kovalevsky, A.; Mustyakimov, M.; Fisher, Z.; Hoffman, C.; Kratky, C.; Langan, P. *Acta Crystallogr., Sect. D: Biol. Crystallogr.* **2011**, *67*, 584-591.

(31) Zikovsky, J.; Peterson, P. F.; Wang, X. P.; Frost, M.; Hoffmann, C. *J. Appl. Crystallogr.* **2011**, *44*, 418-423.

(32) Mantid: A high performance framework for reduction and analysis of neutron scattering data, http://www.mantidproject.org (accessed April 2013).

(33) Schultz, A. J.; Srinivasan, K.; Teller, R. G.; Williams, J. M.; Lukehart, C. M. *J. Am. Chem. Soc.* **1984**, *106*, 999-1003.

(34) Sheldrick, G. *Acta Crystallogr., Sect. A: Found. Crystallogr.* **2008**, *64*, 112-122.

(35) Farrugia, L. *J. Appl. Crystallogr.* **1997**, *30*, 565.

(36) McKinnon, J. J.; Spackman, M. A.; Mitchell, A. S. *Acta Crystallogr., Sect. B: Struct. Sci., Cryst. Eng. Mater.* **2004**, *60*, 627-668.

Chapter 4. Hydricity of an Fe–H Species and Catalytic CO_2 Hydrogenation

Reproduced in part with permission from:
Fong, H.; Peters, J. C. *Inorganic Chemistry* [Online early access]. DOI: 10.1021/ic502508p.

4.1 Preface

This chapter describes the CO_2 hydrogenation chemistry of a series of *tris*-phosphino-iron-hydride complexes. In Chapter 2, I showed that the (**TPB**)Fe scaffold is a competent for catalytic olefin and arylacetylene hydrogenation and that the hydrogenative reactivity was due in part to iron-borane cooperativity. In this chapter, I will show that the iron-borane cooperativity does not facilitate catalytic CO_2 hydrogenation for the (**TPB**)Fe system. I also studied the CO_2 hydrogenation chemistry of a series of structurally related *tris*-phosphino-iron complexes, and experimentally estimated the hydricity of the iron-hydride species (**SiP$^{iPr}_3$**)Fe(N_2)(H).

I am the first author of a paper published in *Inorganic Chemistry* that describes this work. The other author is Jonas Peters. I performed all of the experiments described in the manuscript, and Jonas Peters and I analyzed the results. Nathan Dalleska of the Environmental Analysis Center at Caltech assisted me in developing a method for the GC-FID measurements.

4.2 Introduction

The reduction of carbon dioxide into value-added chemicals and liquid fuels has received considerable attention recently due to increasing interest in the development of carbon neutral energy sources.[1] The production of liquid fuels such as methanol[2] or formic acid[3] from CO_2 and H_2 (or its formal equivalents) is particularly attractive. However, selective production of these products using heterogeneous catalysts remains challenging.[4-6] One interesting approach towards CO_2 reduction is to use molecular catalysis, where product selectivity may be better controlled than heterogeneous systems.[7] The catalytically active species in molecular systems can often be probed either directly or indirectly, thereby offering opportunities to understand the catalytic mechanism and synthetically tune systems in a well-defined manner.[8]

One of the simplest CO_2 reduction reactions is its hydrogenation to formic acid.[3] While a number of noble-metal catalysts for the hydrogenation of CO_2 to formic acid exist,[9-17] there are only a handful of examples using first-row transition metals such as iron[18-24] and cobalt,[25-28] and information about their thermodynamic properties and elementary reaction steps is needed.[29-34] For example, the hydricity (ΔG_H-), which is the heterolytic dissociation energy of an $[M{-}H]^{n+}$ into M^{n+1} and H^- (equation 4.1), has only been experimentally determined for one iron-hydride complex FpH[35] (FpH = $(C_5H_5)Fe(CO)_2(H)$) despite recent reports of iron-catalyzed CO_2 hydrogenation.[18-24] Knowledge of the hydricities of hydrogenation catalysts can aid the design of new catalysts. This is highlighted by the recent work of Linehan and coworkers on a cobalt-hydride catalyst,[26-27] in which the design of this efficient CO_2-to-

formate hydrogenation system was achieved in part by using a cobalt-hydride that was more hydridic (i.e., < 43 kcal/mol) than the hydricity of formate[36] (equation 4.2).

$[M–H]^{n+} \rightarrow M^{n+1} + H^-$ ΔG_H- (4.1)

$OCHO^- \rightarrow CO_2 + H^-$ ΔG_H- = 43 kca/mol (4.2)

As part of our exploratory research of phosphine-supported iron complexes in small molecule activation reactions[37-42] I were interested in studying the catalytic CO_2 hydrogenation chemistry of a series of *tris*-phosphino-iron species (Chart 4.1): (**SiP$^{R}_{3}$**)Fe(L)(H) (L = H_2 or N_2; SiP^{R}_{3} = [Si(*o*-$C_6H_4PR_2)_3$]$^-$, R = ^{i}Pr or Ph),[37,43-44] (**PhBP$^{iPr}_{3}$**)Fe(H)$_3$(PMe_3) ($PhBP^{iPr}_{3}$ = $PhB(CH_2P^{i}Pr_2)_3$),[45] [(**NP$^{iPr}_{3}$**)Fe(N_2)(H)](PF_6) (NP^{iPr}_{3} = $N(CH_2CH_2P^{i}Pr_2)_3$),[46] (**TPB**)(μ–H)Fe(L)(H) (L = N_2 or H_2, TPB = B(*o*-$C_6H_4P^{i}Pr_3)_3$),[44] (**CP$^{iPr}_{3}$**)FeCl (CP^{iPr}_{3} = [C(*o*-$C_6H_4P^{i}Pr_2)_3$]$^-$),[42] and (**C^{Si}P$^{Ph}_{3}$**)FeCl ($C^{Si}P^{Ph}_{3}$ = [C(Si$(CH_3)_2CH_2PPh_2)_3$]$^-$).[47] These systems are structurally related to two *tetra*-phosphino-iron-hydride CO_2 hydrogenation catalysts ([(**PP$_3$**)Fe(H_2)(H)](BF_4)[19,48] and (**tetraphos**)Fe(H_2)(H)](BF_4),[20] where PP_3 = $P(CH_2CH_2PPh_2)_3$ and tetraphos = P(*o*-$C_6H_4PPh_2)_3$), studied in a similar context by the groups of Beller and Laurenczy (Chart 4.1). A distinguishing feature of the present series of *tris*-phosphino-iron complexes is that each of the present ligand scaffolds possesses a different apical unit. These include an X-type silyl in SiP^{R}_{3}, an X-type alkyl in CP^{iPr}_{3} and $C^{Si}P^{Ph}_{3}$, a non-coordinating borate in $PhBP^{iPr}_{3}$, an L-type amine in NP^{iPr}_{3}, and a Z-type borane in TPB. Each of these apical units can confer different (i) geometries at iron, (ii) formal oxidation states at iron, and (iii) reactivity patterns for otherwise structurally similar species, as we have studied previously with respect to N_2 activation chemistry.[37-42]

Chart 4.1 Select phosphine-metal complexes of relevance to catalytic CO_2 hydrogenation.

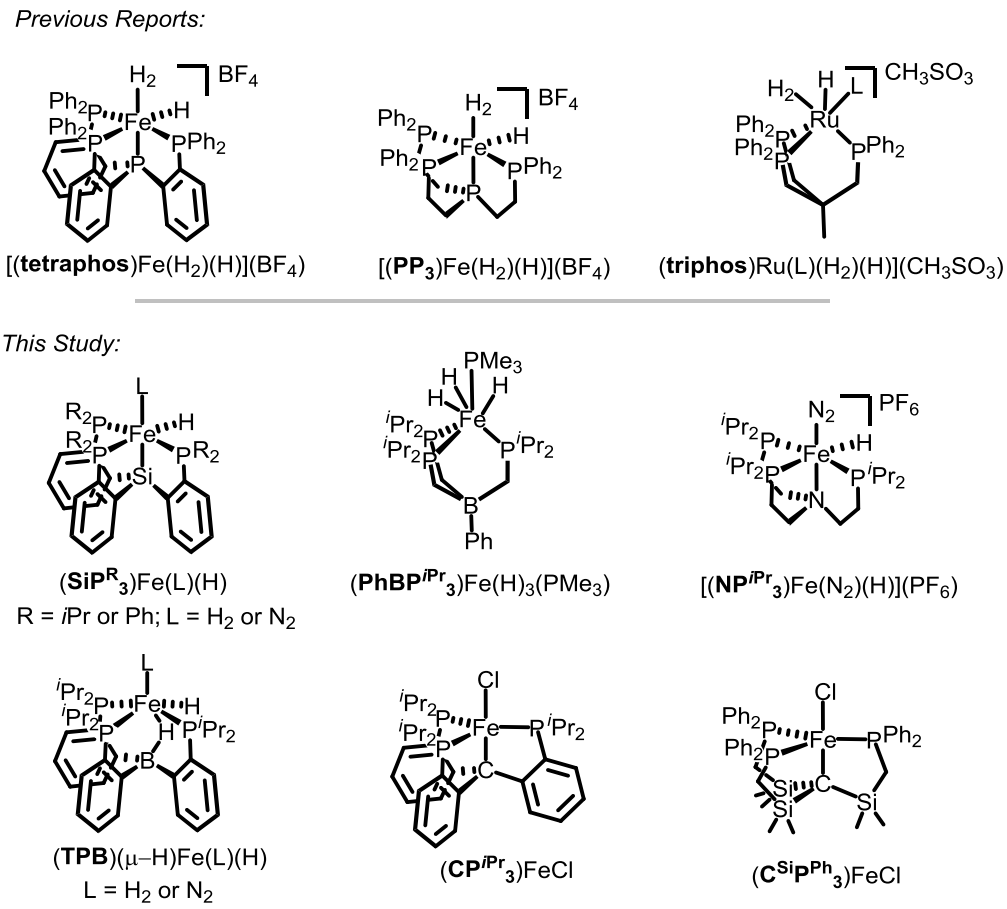

This chapter presents the experimentally determined pK_a and hydricity values for the (**SiP$^{iPr}_3$**)Fe system as well as the catalytic and stoichiometric hydrogenation of CO_2 in this and related *tris*-phosphino-iron species shown in Chart 4.1. Under elevated temperatures and pressures of CO_2 and H_2 and with triethylamine as base, the (**SiP$^{iPr}_3$**)Fe, (**SiP$^{Ph}_3$**)Fe, (**PhBP$^{iPr}_3$**)Fe, and (**CP$^{iPr}_3$**)Fe systems catalytically hydrogenate CO_2 to triethylammonium formate and methylformate, while (**NP$^{iPr}_3$**)Fe, (**TPB**)Fe, and (**C^{Si}P$^{Ph}_3$**)Fe did not catalyze CO_2

hydrogenation. We also show that despite a low hydricity (i.e., large ΔG_{H^-} value) for the complex (**SiP$^{iPr}_3$**)Fe(H_2)(H) (ΔG_{H^-} = 54.3 ± 0.9 kcal/mol) coordination of the formate product to the iron-center following hydride transfer to CO_2 provides enough driving force to make the reaction thermally accessible.

4.3 Results and Discussion

*4.3.1 pK_a and Hydricity for (**SiP$^{iPr}_3$**)Fe*

Since Fe−H species have been invoked as intermediates for CO_2 hydrogenation, we were curious if (**SiP$^{iPr}_3$**)Fe(H_2)(H) was sufficiently hydridic to react with CO_2. One method for determining hydricities is to use a thermochemical cycle that involves deprotonating the conjugate acid of the metal-hydride of interest. We previously reported the dihydrogen chemistry of the (**SiP$^{iPr}_3$**)Fe system,[44] including the deprotonation of the cationic iron-dihydrogen complex [(**SiP$^{iPr}_3$**)Fe(H_2)](BAr$^F_4$) (BAr$^F_4$ = [B(3,5-CF_3-C_6H_3)$_4$]$^-$) by Hünig's base under H_2 to afford (**SiP$^{iPr}_3$**)Fe(H_2)(H).[43] This motivated us to use this deprotonation reaction to experimentally determine the hydricity of (**SiP$^{iPr}_3$**)Fe(H_2)(H) using the series of equations in Scheme 4.1. The equilibrium in equation 4.3 was followed by ^{1}H NMR spectroscopy independently with 1,8-*bis*(dimethylamino)naphthalene (proton sponge, K_{eq} = 4.3), 2,6-lutidine (K_{eq} = 3.3 x 10^{-5}), and 2,4,6-trimethylpyridine (K_{eq} = 5.1 x 10^{-5}) in d_8-THF.[i] The reverse protonation of (**SiP$^{iPr}_3$**)Fe(H_2)(H) with the BAr$^F_4$-salt of 1,8-

[i] THF is known to bind competitively with H_2 on [(**SiP$^{iPr}_3$**)Fe(L)](BAr$^F_4$] (where L = THF or H_2), and the THF/H_2 binding equilibrium was taken into account in the calculations; see Appendix 3.

bis(dimethylammonium)naphthalene (K_{eq} = 2.6) was also followed by ^{1}H NMR spectroscopy in d_8-THF.

Scheme 4.1 Reactions relevant to the determination of the pK_a and hydricity of (**SiP$^{iPr}_3$**)Fe.

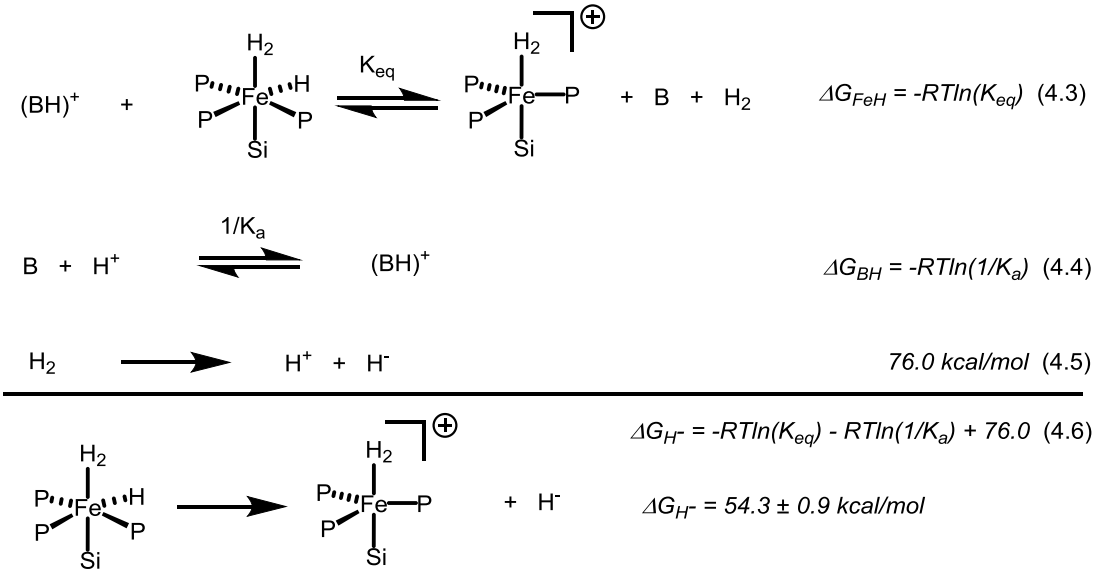

See Chart 4.1 for the detailed ligand representation. B = base.

Note that the pK_a of the dihydrogen ligand in [(**SiP$^{iPr}_3$**)Fe(H_2)](BAr$^F_4$) can be estimated using equations 4.3 and 4.4. The experimentally determined pK_a in THF using this method is pK_a^{THF} = 10.8 ± 0.6 for [(**SiP$^{iPr}_3$**)Fe(H_2)](BAr$^F_4$). Notably, the pK_a^{THF} agrees very well with the predicted value of 10.2 obtained from the ligand acidity constants method recently developed by Morris.[ii,49] It should be cautioned that this is only a rough estimate of the pK_a of

[ii] The pK_a of [(**SiP$^{iPr}_3$**)Fe(H_2)](BAr$^F_4$) was estimated using the Morris ligand acidity constants method. These calculations rely on ligand acidity constants for each of the ligands of the conjugate base metal complex, which in this case is the deprotonation product (**SiP$^{iPr}_3$**)Fe(H_2)(H). We note that the ligand acidity constants for H_2 and the formally Si^- ligands of the conjugate base complex are not known. Therefore, the reported ligand acidity

[(**SiP$^{iPr}_3$**)Fe(H_2)](BAr^F_4), because the pK_a of [(**SiP$^{iPr}_3$**)Fe(H_2)](BAr^F_4) is a measure of the removal of a proton to afford "(**SiP$^{iPr}_3$**)Fe(H)", whereas in the observed deprotonation reaction dihydrogen coordinates to this species to afford the (**SiP$^{iPr}_3$**)Fe(H_2)(H) and contributes to the equilibrium depicted in equation 4.3.

With the equilibrium of equation 4.3 in hand, the hydricity of the conjugate base (**SiP$^{iPr}_3$**)Fe(H_2)(H) can be determined by the summation of equations 4.3-4.5 to give equation 4.6.[50-51] Most hydricity values have been reported in acetonitrile due in part to the known heterolytic dissociation energy of H_2 in acetonitrile (equation 4.5). However, irreversible coordination of acetonitrile to [(**SiP$^{iPr}_3$**)Fe precluded the use of this solvent. An empirical relationship relates the pK_a^{THF} of a metal complex to the pK_a in acetonitrile (pK_a^{MeCN}).[52] Using this relationship, the pK_a^{MeCN} of [(**SiP$^{iPr}_3$**)Fe(H_2)](BAr^F_4) is 15.9 ± 0.7. Combining the pK_a^{MeCN} of [(**SiP$^{iPr}_3$**)Fe(H_2)](BAr^F_4) with equation 4.5, the hydricity of (**SiP$^{iPr}_3$**)Fe(H_2)(H) in MeCN is 54.3 ± 0.9 kcal/mol. This is only the second experimentally estimated hydricity value of an iron-hydride complex.[35]

Formal hydride transfer from phosphine ligated iron-hydride complexes to CO_2 to give formate is known in the literature.[29-34,53] A comparison of the hydricity of (**SiP$^{iPr}_3$**)Fe(H_2)(H) to that of formate (equation 4.2) indicates that the reaction for hydride transfer from (**SiP$^{iPr}_3$**)Fe(H_2)(H) to CO_2 to afford formate is endergonic by over 10 kcal/mol. Yet, as will

---

constants for C_2H_4 as a model for the H_2 ligand and CH_3^-/H^- as a model for the Si^- ligand unit were used for these calculations. For the Morris acidity constant method, see ref 49.

be shown below, (**SiP$^{iPr}_3$**)Fe(H_2)(H) can still react with CO_2 both stoichiometrically and catalytically to afford formate.

Scheme 4.2 Stoichiometric CO_2 hydrogenation to triethylammonium formate.

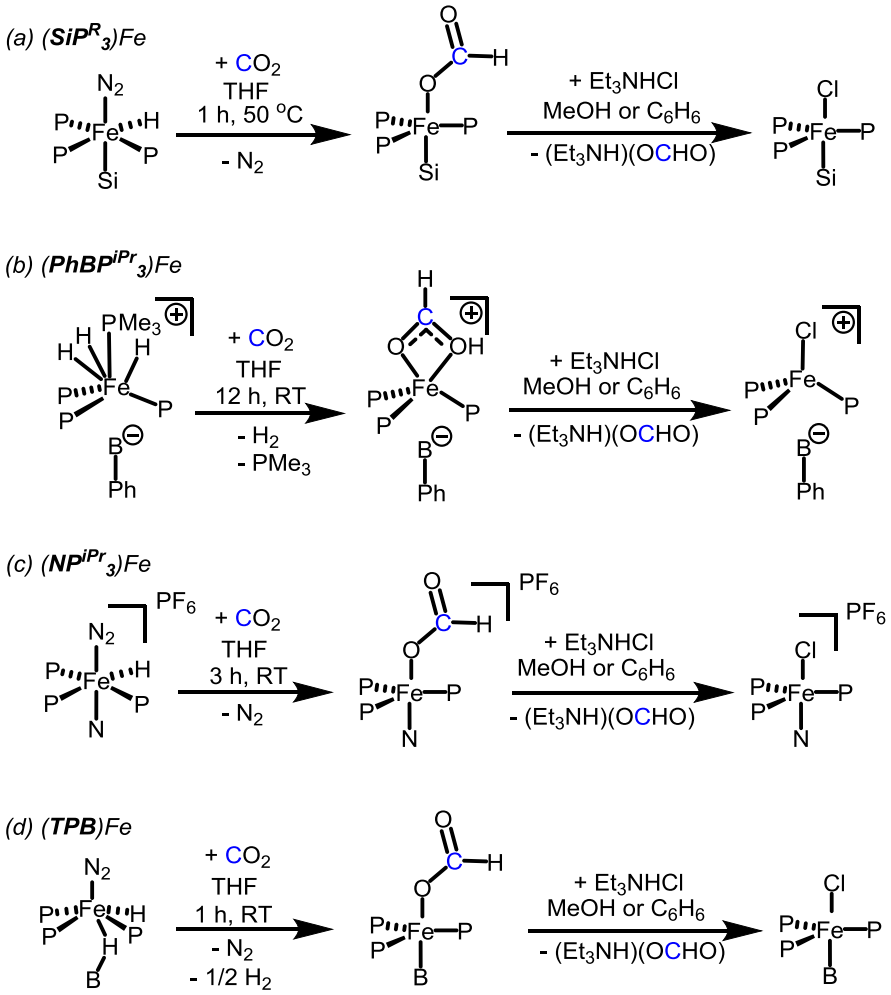

See Chart 4.1 for the detailed representations of the ligands indicated.

4.3.2 Stoichiometric Reactivity of Fe–H Species with CO_2

In addition to (**SiP$^{iPr}_3$**)Fe(L)(H)[43-44] (where L = N_2 or H_2), our group has previously reported the synthesis and characterization of three other related *tris*-phosphino-iron-hydride

complexes, (**PhBP$^{iPr}_3$**)Fe(H)$_3$(PMe$_3$),[45] [(**NP$^{iPr}_3$**)Fe(N$_2$)(H)](PF$_6$),[46] and (**TPB**)(μ–H)Fe(N$_2$)(H)[44] (Chart 4.1), and demonstrated that the two former complexes, (**PhBP$^{iPr}_3$**)Fe(H)$_3$(PMe$_3$) and (**TPB**)(μ–H)Fe(N$_2$)(H), are olefin hydrogenation catalysts. The iron-hydride species of the *tris*(diphenyl-phosphino)silyl ligand, (**SiP$^{Ph}_3$**)Fe(N$_2$)(H), had not previously been reported, but it has now been synthesized in an analogous manner to the preparation of the isopropyl-analogue (**SiP$^{iPr}_3$**)Fe(N$_2$)(H) (*vide infra*). The reactivity of these iron-hydrides to CO_2 was probed.

Synthesis of iron-formate species. A yellow solution of (**SiP$^{Ph}_3$**)Fe(N$_2$)(H) reacted with CO_2 (1 atm) at 50 °C over 1 h to afford the orange insertion product (**SiP$^{Ph}_3$**)Fe(OCHO) (Scheme 4.2a**)**. Consistent with the κ^1-bound formate ligand,[54] ATR-IR spectroscopy showed two signature vibrational features at 1618 cm^{-1} and 1316 cm^{-1} ($^{13}CO_2$: 1587 and 1254 cm^{-1}) with a Δν(O–C–O) of 302 cm^{-1} (Table 4.1). As expected for a five-coordinate (**SiP$^{R}_3$**)Fe^{II} complex,[55]

Table 4.1 IR stretching frequencies and solution magnetic moments for iron-formate complexes.

	μ_{eff} (μ_B)[a]	ν_{asym}(O–C–O) (cm^{-1})[b]		ν_{sym}(O–C–O) (cm^{-1})[b]		$\Delta\nu_{asym}$ (O–C–O) (cm^{-1})[b]
		CO_2	$^{13}CO_2$	CO_2	$^{13}CO_2$	
(**SiP$^{Ph}_3$**)Fe(OCHO)	2.7	1618	1587	1316	1254	302
(**SiP$^{iPr}_3$**)Fe(OCHO)	2.8	1623	1583	---	---	---
(**PhBP$^{iPr}_3$**)Fe(OCHO)	5.0	1595	1546	1362	1355	233
[(**NP$^{iPr}_3$**)Fe(OCHO)][PF$_6$]	5.1	1613	1579	---	---	---
(**TPB**)Fe(OCHO)	4.2	1627	1588	1291	1269	336

[a]Solution magnetic moments at RT. [b]ATR-IR data of solution thin films. [c]Difference between ν_{asym}(O–C–O) and ν_{sym}(O-C–O).

(**SiP$^{Ph}_3$**)Fe(OCHO) is S = 1 (2.7 μ_B in C_6D_6 at RT). (**SiP$^{iPr}_3$**)Fe(N_2)(H) reacted with CO_2 similarly to afford (**SiP$^{iPr}_3$**)Fe(OCHO). The ATR-IR spectrum showed an asymmetric O–C–O stretch at 1623 cm^{-1} ($^{13}CO_2$: 1583 cm^{-1}). While the symmetric O–C–O stretch could not be reliably discerned (Table 4.1), its S = 1 spin state (2.8 μ_B in C_6D_6 at RT) and yellow colour indicate a five coordinate (**SiP$^{iPr}_3$**)Fe(OCHO) complex.

Exposing a yellow THF solution of (**PhBP$^{iPr}_3$**)Fe(H)$_3$(PMe_3) to CO_2 (1 atm) for 12 h at room temperature afforded the κ^2-bound formate adduct (**PhBP$^{iPr}_3$**)Fe(OCHO) (Scheme 4.2b) as a light yellow solution. The ATR-IR spectrum of this S = 2 species (5.0 μ_B, C_6D_6 at RT) exhibited features of a formate ligand at 1595 cm^{-1} and 1362 cm^{-1} ($^{13}CO_2$: 1546 and 1355 cm^{-1}) with a $\Delta\nu$(O–C–O) = 233 cm^{-1} that is consistent with the κ^2-bound formate assignment.[54] The formate coordination mode is in contrast to the κ^1-bound formate ligands in (**SiP$^{R}_3$**)Fe(OCHO), [(**NP$^{iPr}_3$**)Fe(OCHO)](PF_6), and (**TPB**)Fe(OCHO). Presumably, this arises because of the lower coordination number in (**PhBP$^{iPr}_3$**)Fe.

A yellow THF solution of [(**NP$^{iPr}_3$**)Fe(N_2)(H)](PF_6) reacted with CO_2 (1 atm) at room temperature over 3 h to afford the formate adduct [(**NP$^{iPr}_3$**)Fe(OCHO)](PF_6) (Scheme 4.2c) as a colorless solution. [(**NP$^{iPr}_3$**)Fe(OCHO)](PF_6) is S = 2 (5.1 μ_B, C_6D_6 at RT), analogous to [(**NP$^{iPr}_3$**)FeCl](PF_6).[46] Consistent with the iron-formate formulation, ATR-IR spectroscopy showed a diagnostic ν_{asym}(O–C–O) vibrational feature at 1613 cm^{-1} that shifts to 1579 cm^{-1} with $^{13}CO_2$. However, the accompanying lower energy ν_{sym}(O–C–O) vibrational feature could not be reliably assigned due to overlapping ligand vibrational modes in the 1200 – 1300 cm^{-1}

region. The obscured ν_{sym}(O–C–O) feature prevented assignment of the formate binding mode, but the ν_{asym}(O–C–O) most closely matches κ^1-bound formate ligands (Table 4.1).[54]

Mixing a benzene solution of (**TPB**)(μ–H)Fe(N_2)(H) with CO_2 (1 atm) at room temperature afforded the κ^1-formate complex (**TPB**)Fe(OCHO) (Scheme 4.2d) as a yellow solution. The color, ^{1}H NMR spectrum, and solution magnetic moment (4.2 μ_B, S = 3/2 in C_6D_6 at RT) are consistent with the formulation of (**TPB**)Fe(OCHO) as a {Fe–B}^{7} species.[iii,58] As for (**SiP$^R_3$**)Fe(OCHO), (**TPB**)Fe(OCHO) exhibited diagnostic κ^1-formate ligand vibrational modes at 1627 cm^{-1} and 1291 cm^{-1} ($^{13}CO_2$: 1588 and 1269 cm^{-1}) with a Δν(O–C–O) of 336 cm^{-1} (Table 4.1).[54] The IR spectrum of (**TPB**)Fe(OCHO) lacks any feature that is diagnostic for a B–H unit.[59] For comparison, in the related S = 2 (**TPBH**)Fe(CCAr) (Ar = phenyl or tolyl) complex, where a terminal B–H is present, the IR spectra exhibits diagnostic B–H vibrations at 2490 cm^{-1} for Ar = phenyl and 2500 cm^{-1} for Ar = tolyl.[44]

The formation of (**TPB**)Fe(OCHO) from the reaction of (**TPB**)(μ–H)Fe(N_2)(H) with CO_2 (1 atm) is notable in that there is a formal loss of an H-atom (Scheme 4.3). The loss of 0.5 equiv of H_2 (relative to the starting iron complex) was confirmed by gas-chromatography (GC-TCD; 0.44 equiv of H_2 quantified). The reaction between the previously reported (**TPB**)Fe(N_2)[58] with formic acid also formed **(TPB**)Fe(OCHO), with 0.42 equiv of H_2 detected by GC-TCD as a product (Scheme 4.3).

[iii] The {M–E}^{n} notation refers to the number of valence electrons that are formally assigned to the metal (e.g., Fe) and those shared with E (e.g., B). Since the M–E bond may be covalent and the M–E interaction is dictated in part by the ligand chelate and M–E distance, the bonding electrons between M–E are not reliably assigned to either atom. As such, the {M–E}^{n} notation tracks the number of valence electrons without assignment of valence or oxidation numbers. See ref 56 and 57.

Scheme 4.3 Reactivity of (**TPB**)Fe complexes with CO_2 and formic acid.

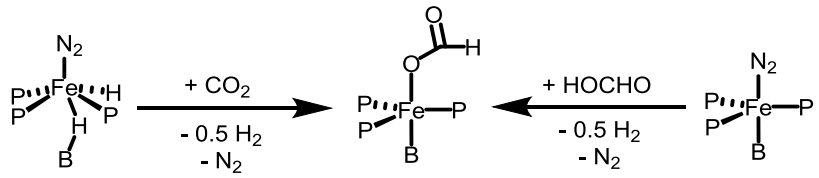

See Chart 4.1 for the detailed ligand representation.

Reactivity of Fe–OCHO species. The formate ligands in all five of the aforementioned iron-formate complexes are substitutionally labile. The addition of triethylammonium chloride (10 equiv) into either benzene or methanol solutions of these complexes resulted in the formation of the respective iron-chloride complexes and triethylammonium formate (Scheme 4.2). Furthermore, the iron-chloride products from these metathesis reactions are synthons for the respective iron-hydride complexes.

With this metathesis reaction and known reaction chemistry for the (**SiP$^{iPr}_3$**)Fe scaffold, we can construct a synthetic cycle for CO_2 hydrogenation, which may inform the catalytic CO_2 hydrogenation reaction (*vide infra*). Starting from the Fe–Cl species, (**SiP$^{iPr}_3$**)FeCl reacts with MeMgCl (1 equiv) to afford the iron-methyl complex (**SiP$^{iPr}_3$**)FeMe (this work, Scheme 4.4a). Subsequent reaction with H_2 affords (**SiP$^{iPr}_3$**)Fe(N_2)(H) (Scheme 4.4b).[43] Alternatively, the iron-methyl complex (**SiP$^{iPr}_3$**)FeMe can be converted into cationic dihydrogen complex [(**SiP$^{iPr}_3$**)Fe(H_2)](BAr$^F_4$)[43] (Scheme 4.4c-d). The dihydrogen ligand in the latter complex can be deprotonated by triethylamine (this work) to generate (**SiP$^{iPr}_3$**)Fe(L)(H) (where L = N_2 or H_2) (Scheme 4.4e). As shown above, (**SiP$^{iPr}_3$**)Fe(N_2)(H) reacts with CO_2 to afford the

(**SiP$^{iPr}_{3}$**)Fe(OCHO) (Scheme 4.4f), which can undergo metathesis with (Et_3NH)Cl to afford the starting iron-chloride complex (Scheme 4.4g).

Reaction of (**SiP$^{iPr}_{3}$**)FeCl with H_2 is also possible. A CD_3OD:d_8-THF (10:1) solution of (**SiP$^{iPr}_{3}$**)FeCl with excess triethylamine in the presence of H_2 and D_2 (*ca.* 1 atm : 1 atm) gives HD (Scheme 4.4h). Related, the cationic dihydrogen adduct [(**SiP$^{iPr}_{3}$**)Fe(H_2)][BAr^F_4], a model for [(**SiP$^{iPr}_{3}$**)Fe(H_2)]$^+$, scrambles a mixture of H_2 and D_2 (*ca.* 1 atm : 1 atm) to HD in a CD_3OD:d_8-THF solution (10:1). (**SiP$^{iPr}_{3}$**)FeCl is the sole observed iron-containing species by ^{1}H NMR spectroscopy in the former experiment, indicating that the equilibrium with the putative [(**SiP$^{iPr}_{3}$**)Fe(H_2)]$^+$ responsible for scrambling H_2/D_2 heavily favors (**SiP$^{iPr}_{3}$**)FeCl.

Scheme 4.4 Synthetic cycle for CO_2 hydrogenation to formate by (**SiP$^{iPr}_{3}$**)Fe**.**

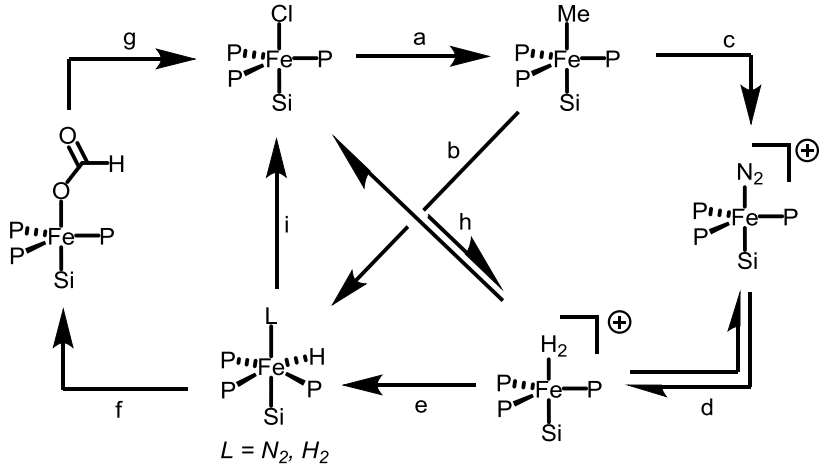

See Chart 4.1 for the detailed ligand representation. Conditions: a) MeMgCl, THF; b) H_2, THF (plus N_2 workup for L = N_2); c) ($HBAr^F_4$)(Et_2O)$_2$, C_6H_6; d) H_2 (*forward*), N_2 (*reverse*), THF; e) Et_3N, THF (plus N_2 workup for L = N_2); f) CO_2, MeOH, THF or C_6H_6; g) (Et_3NH)Cl, C_6H_6 or MeOH; h) 1:1 atm H_2:D_2, Et_3N, 10:1 CD_3OD:d_8-THF (*HD is produced*); i) for L = N_2, Et_3NHCl, 10:1 CD_3OD:d_8-THF.

4.3.3 Catalytic Hydrogenation

Having realized a synthetic cycle for CO_2 hydrogenation to formate, the next step was to explore if the process could be made catalytic. Following literature precedent, the *tris*-phosphino-iron-chloride complexes were tested in an initial screen for catalysis,[9-16,18-26,28] and triethylamine was added to serve as a base.[60] ^{1}H NMR spectroscopy with DMF added as an integration standard was used to quantify triethylammonium formate yields. Other known products of CO_2 hydrogenation are formate esters such as methylformate obtained from the esterification of formate with methanol.[19-20] Due to the volatility and low yields of MeOCHO, GC-FID was used to quantify this product.

Under the standardized reaction conditions of 29 atm of CO_2 and 29 atm of H_2 in methanol solvent with triethylamine, (**SiP$^{iPr}_3$**)FeCl, (**SiP$^{Ph}_3$**)FeCl, and (**PhBP$^{iPr}_3$**)FeCl are precatalysts for the hydrogenation of CO_2 to triethylammonium formate and methylformate (Table 4.2, entries 1-3). (**SiP$^{Ph}_3$**)FeCl is the most active, having an average turnover number of 200. These three systems are also more selective for $(Et_3NH)(OCHO)$ than MeOCHO, with (**PhBP$^{iPr}_3$**)FeCl being the most selective of the three with a 10:1 $(Et_3NH)(OCHO)$ to MeOCHO product ratio. It is also worth noting that the primary coordination sphere of the zwiterionic (**PhBP$^{iPr}_3$**)Fe system is structurally similar to a known cationic ruthenium system (**triphos**)Ru (triphos = $CH_3C(CH_2PPh_2)_3$) that hydrogenates CO_2 to methanol[61] and also dehydrogenates formic acid[62] (Chart 4.1). We have also reported the reduction of CO_2 to oxalate by (**PhBP$^{iPr}_3$**)Fe.[63]

Table 4.2 *Tris*-phosphino-iron catalyzed CO_2 hydrogenation.

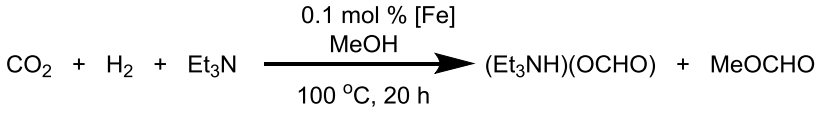

Entry	Precatalyst	TON[a]	$(Et_3NH)(OCHO)$:MeOCHO ratio[e]
1	(**SiP$^{iPr}_3$**)FeCl	53	3:1
2	(**SiP$^{Ph}_3$**)FeCl	200	2:1
3	(**PhBP$^{iPr}_3$**)FeCl	27	10:1
4	[(**NP$^{iPr}_3$**)FeCl](PF$_6$)	0	0
5	(**TPB**)FeCl	0	0
6	(**CP$^{iPr}_3$**)FeCl	27	6:1
7	(**C^{Si}P$^{Ph}_3$**)FeCl	0	0
8	**PP$_3$**/Fe(BF$_4$)$_2$[b,c]	486	3:1
9	[(**tetraphos**)FeF]BF$_4$[b,d]	1661	1:1
10	$FeCl_2$	0	0
11	$FeCl_2$/4 PPh_3	0	0
12	no iron	0	0

Conditions: 0.1 mol % (0.7 mM) iron-precatalyst (relative to Et_3N), methanol, 651 mM Et_3N, 29 atm CO_2 (RT), 29 atm H_2 (RT), 100 °C, 20 h. [a]Turnover number: combined yield (moles) of $(Et_3NH)(OCHO)$ and MeOCHO divided by moles of precatalyst. [b]Previously studied under slightly different conditions. [c]See ref 19. [d]See ref 20. [e]Ratio of the amount of $(Et_3NH)(OCHO)$ product to the amount of MeOCHO product.

Under the standard conditions, [(**NP$^{iPr}_3$**)FeCl](PF$_6$) and (**TPB**)FeCl are not precatalysts for the reaction (Table 4.2, entries 4 and 5). The recently reported (**CP$^{iPr}_3$**)FeCl complex (Chart 4.1),[42] where the silicon atom in (**SiP$^{iPr}_3$**)FeCl is substituted by a carbon atom, is also catalytically competent (Table 4.2, entry 6) but is significantly less active than (**SiP$^{Ph}_3$**)FeCl.

Another carbon variant of the *tris*-phosphino-iron series of complexes, ($\mathbf{C^{Si}P^{Ph}_3}$)FeCl[47] (Chart 4.1), is not catalytically competent (Table 4.2, entry 7).

For a direct comparison with known iron CO_2 hydrogenation catalysts and as a benchmark of the method employed, we subjected the (**PP$_3$**)Fe[19] and (**tetraphos**)Fe[20] systems to our standardized conditions. Beller and Laurenczy reported that a mixture of the PP_3 ligand with $Fe(BF_4)_2$ is one of the more active conditions for CO_2 hydrogenation in the PP_3 system. Under the standard conditions of this study, a 1:1 mixture of PP_3 and $Fe(BF_4)_2$ hydrogenates CO_2 to triethylammonium formate and methylformate, as well, at a total TON of 486 (Table 4.2, entry 8). The (**tetraphos**)Fe(F)$(BF_4)_2$ complex also catalyzes CO_2 hydrogenation to the same products at a total TON of 1661 (Table 4.2, entry 9). These values are in near agreement with the respective literature reports. The (**tetraphos**)Fe(F)$(BF_4)_2$ complex is the least selective of the series in Table 4.2 for formate production.

A series of control experiments were performed to probe the homogeneity of the reaction. The catalytic reaction is uninhibited by the addition of elemental mercury (see Appendix 3). Also, CO_2 hydrogenation does not occur with the iron salt $FeCl_2$ (Table 4.2, entry 10) or with a 1:4 mixture of $FeCl_2$ and triphenylphosphine (Table 4.2, entry 11), nor does it proceed in the absence of an iron source (Table 4.2, entry 12). These experiments do not preclude a role for heterogeneous species, but provide evidence consistent with a homogeneous process.

To gain insight into the reaction, we chose to study the hydrogenation catalysis by the ($\mathbf{SiP^{iPr}_3}$)Fe system further, as it is more active than ($\mathbf{PhBP^{iPr}_3}$)FeCl, and because its

coordination chemistry has been studied in greater detail than that of its phenyl-analogue (**SiP$^{Ph}_3$**)Fe.[43-44]

Under standard conditions but in the absence of H_2, triethylammonium formate and methylformate were not detected (Table 4.3, entry 1). When the reaction was run in CD_3OD instead of CH_3OH, $(Et_3NH)(OCHO)$ was detected by ^1H NMR spectroscopy at the conclusion of the reaction, while $(Et_3ND)(OCDO)$ was not detected by ^2H NMR spectroscopy (Table 4.3, entry 2). The data collectively indicate that H_2 is the source of the H-atom equivalents.

High pressures of CO_2 and H_2 are critical, as the reaction does not proceed at or near atmospheric pressures of H_2 and CO_2, in agreement with most literature examples (see Appendix 3).[3,9-16,18-26,28] Reducing the CO_2 pressure to 5.5 atm while keeping the H_2 pressure at 29 atm only modestly decreases the overall TON (Table 4.3, entry 13), but significantly increases the selectivity for formate. Reducing the H_2 pressure to 5.5 atm while keeping the CO_2 pressure at 29 atm stops catalysis (Table 4.3, entry 14). Also critical is methanol, as catalytic activity does not occur in THF under any pressures of CO_2 and H_2 studied here (see Appendix 3), highlighting the importance of polar, protic solvents in phosphine-iron CO_2 hydrogenation catalysis.[60]

It was determined that 100 °C and 20 h are optimal for the catalytic reaction under the conditions studied here. Running the reaction at 150 °C slightly reduces the turnover relative to the standard conditions (Table 4.3, entry 3), which is likely a result of catalyst decomposition (*vide infra*). At 20 °C no reaction occurs (Table 4.3, entry 4), and the starting precatalyst, (**SiP$^{iPr}_3$**)FeCl, is the only iron-containing species at the end of the reaction. Decreasing the

Table 4.3 (**SiP$^{iPr}_3$**)FeCl catalyzed CO_2 hydrogenation under varied conditions.

$CO_2 + H_2 + Et_3N \xrightarrow{0.1\ \text{mol \% [Fe]}} (Et_3NH)(OCHO) + MeOCHO$

Entry	Deviation from Standard Conditions[a]	TON[b]	$(Et_3NH)(OCHO)$:MeOCHO ratio[f]
0	none	53	3:1
1	0 atm H_2	0	0
2[c]	CD_3OD	32	2:1
3	150 °C	40	2:1
4	20 °C	0	0
5	2 h	16	1:0
6	0.5 equiv $(Et_3NH)Cl$[d]	41	5:1
7	0.5 equiv $NaBF_4$[d]	93	6:1
8	0.5 equiv $NaBAr^F_4$[d]	69	2:1
9	0.5 equiv NaF[d]	45	8:1
10	0.5 equiv TBAF[d,e]	33	12:1
11	0.5 equiv CsF[d]	26	9:1
12	0.5 equiv K_2CO_3[d]	57	21:1
13	5.5 atm CO_2	47	14:1
14	5.5 atm H_2	0	0

[a]Standard conditions: 0.1 mol % (0.7 mM) iron-precatalyst (relative to Et_3N), methanol, 651 mM Et_3N, 29 atm CO_2 (RT), 29 atm H_2 (RT), 100 °C, 20 h. [b]Turnover number: combined yield (moles) of $(Et_3NH)(OCHO)$ and MeOCHO divided by moles of precatalyst. [c]$(Et_3NH)(OCHO)$ was detected by 1H NMR spectroscopy, but neither $(Et_3ND)(OCDO)$, $(Et_3NH)(OCDO)$, nor $(Et_3ND)(OCHO)$ was detected by ^{2}H NMR spectroscopy. [d]Relative to moles of (**SiP$^{iPr}_3$**)FeCl. [e]TBAF = tetrabutylammonium fluoride. [f]Ratio of the amount of $(Et_3NH)(OCHO)$ product to the amount of MeOCHO product.

reaction time to 2 h at 100 °C reduces the TON by a factor of three (Table 4.3, entry 5) compared to the standard conditions.

Using the stoichiometric reactions as a guide, the effects of additives and precatalysts on the catalysis was also probed. The stoichiometric metathesis reaction for the transformation of (**SiP$^{iPr}_3$**)Fe(OCHO) to (**SiP$^{iPr}_3$**)FeCl suggests that chloride substitution for formate may be a route for formate release. However, the addition of 0.5 equiv of (Et_3NH)Cl (relative to iron) into the reaction reduces the TON, although the selectivity for (Et_3NH)(OCHO) over MeOCHO slightly increases to 5:1 (Table 4.3, entry 6). It appears that while chloride may substitute for formate, excess chloride may also slow dihydrogen substitution at iron (*vide infra*) and reduces the overall TON. The addition of a non-coordinating anion in the form of $NaBF_4$ to the catalytic mixture is beneficial, yielding a TON of 93 and 6:1 selectivity for (Et_3NH)(OCHO) (Table 4.3, entry 7), while the addition of Na(BAr^F_4) (BAr^F_4 = B(3,5-(CF_3)$_2$-C_6H_3)$_4$) only modestly increases the TON to 69 and without significantly affecting selectivity (Table 4.3, entry 8). The origin of the effect from the Na^+ and/or borate anion is not understood, but one effect may be that the Na^+ facilitates the removal of the inner-sphere chloride as NaCl. Additionally, alkali metals are known to facilitate CO_2 coordination to cobalt centres.[64] It is also noteworthy that BF_4^- is the counter anion of the highly active tetraphosphine-iron (**PP$_3$**)Fe[19] and (**tetraphos**)Fe[20] systems and also beneficial for iron catalyzed formic acid dehydrogenation.[65] It is unlikely that fluoride, which may be a decomposition product of BF_4^-, is the source of the positive response, as fluoride-salts decrease the TON but increase the selectivity for (Et_3NH)(OCHO) (Table 4.3, entries 9-11). Finally, the

addition of K_2CO_3, which has been reported to enhance CO_2 hydrogenation catalysis for some noble- and non-noble metal systems,[66] has no effect on the TON but most significantly increases selectivity for $(Et_3NH)(OCHO)$ compared to the other additives (Table 4.3, entry 12). The additives containing coordinating anions are more selective for $(Et_3NH)(OCHO)$ over MeOCHO, presumably as a result of anion coordination inhibiting iron-catalyzed esterification of formate to methylformate.[67] However, it should be cautioned that these results are qualitative. A systematic study of the effects of these and other additives on catalysis would be warranted to draw quantitative conclusions.

Other important factors known to affect catalysis are the base identity[26] and base concentrations.[60] A careful study of the effect of different bases and concentrations on catalysis in the present series is beyond the scope of this report, but note that the pK_a of triethylamine is suitably matched to the pK_a of $[(\mathbf{SiP^{iPr}_3})Fe(H_2)]^+$ (*vide supra*), an intermediate in the catalytic cycle of the $(\mathbf{SiP^{iPr}_3})Fe$ system (Scheme 4.5; *vide infra*).

Other $(\mathbf{SiP^{iPr}_3})Fe$ species are also competent precatalyst. The iron-formate $(\mathbf{SiP^{iPr}_3})Fe(OCHO)$ and iron-hydride complex $(\mathbf{SiP^{iPr}_3})Fe(N_2)(H)$ are each catalytically competent precatalyst (Scheme 4.4, entries 1 and 2), with TON's comparable to $(\mathbf{SiP^{iPr}})FeCl$. The cationic dinitrogen complex $[(\mathbf{SiP^{iPr}_3})Fe(N_2)](BAr^F_4)$, which is a synthon for $(\mathbf{SiP^{iPr}_3})Fe(N_2)(H)$ in the presence of H_2 and triethylamine (Scheme 4.4), is also a catalytically competent precatalyst (Scheme 4.4, entry 3). Finally, a mixture of the 1:1 free ligand $HSiP^{iPr}_3$ and $FeCl_2$ is significantly less catalytically competent than the synthesized iron complex

(**SiP$^{iPr}_3$**)FeCl (Scheme 4.4, entry 4). All four of these precatalysts are more selective than (**SiP$^{iPr}_3$**)FeCl for (Et_3NH)(OCHO).

Table 4.4 CO_2 hydrogenation catalyzed by various (**SiP$^{iPr}_3$**)Fe species.

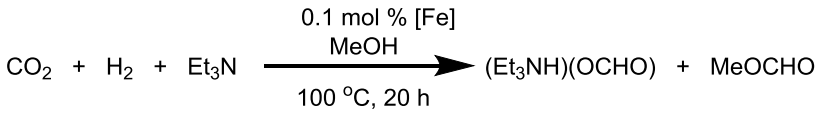

Entry	Precatalyst	TON[a]	(Et_3NH)(OCHO):MeOCHO ratio[c]
0	(**SiP$^{iPr}_3$**)FeCl	53	3:1
1	(**SiP$^{iPr}_3$**)Fe(OCHO)	52	15:1
2	(**SiP$^{iPr}_3$**)Fe(N_2)(H)	47	3:1
3	[(**SiP$^{iPr}_3$**)Fe(N_2)](BAr^F_4)	18	8:1
4	**HSiP$^{iPr}_3$**/$FeCl_2$ (1:1)[b]	12	4:1

Conditions: 0.1 mol % (0.7 mM) iron-precatalyst (relative to Et_3N), methanol, 651 mM Et_3N, 29 atm CO_2 (RT), 29 atm H_2 (RT), 100 °C, 20 h. [a]Turnover number: combined yield (moles) of (Et_3NH)(OCHO) and MeOCHO divided by moles of precatalyst. [b]1:1 mixture of $HSiP^{iPr}_3$:$FeCl_2$ (0.7 mM) was used as the precatalyst in place of (**SiP$^{iPr}_3$**)FeCl. [c]Ratio of the amount of (Et_3NH)(OCHO) product to the amount of MeOCHO product.

The fate of the iron precatalyst (**SiP$^{iPr}_3$**)FeCl under the reaction conditions was also probed. At the end of the reaction under standard conditions, the ^{31}P NMR spectrum showed a mixture of phosphorous-containing material, including significant quantities of free ligand ($HSiP^{iPr}_3$). If the reaction was run at room temperature, only the starting precatalyst (**SiP$^{iPr}_3$**)FeCl was observed by ^1H NMR spectroscopy. These observations indicate that while the catalysis requires heating, elevated temperatures lead to eventual catalyst decomposition.

Scheme 4.5 Proposed catalytic cycle for (**SiP**$^{i\mathbf{Pr}}_{\mathbf{3}}$)Fe in MeOH.

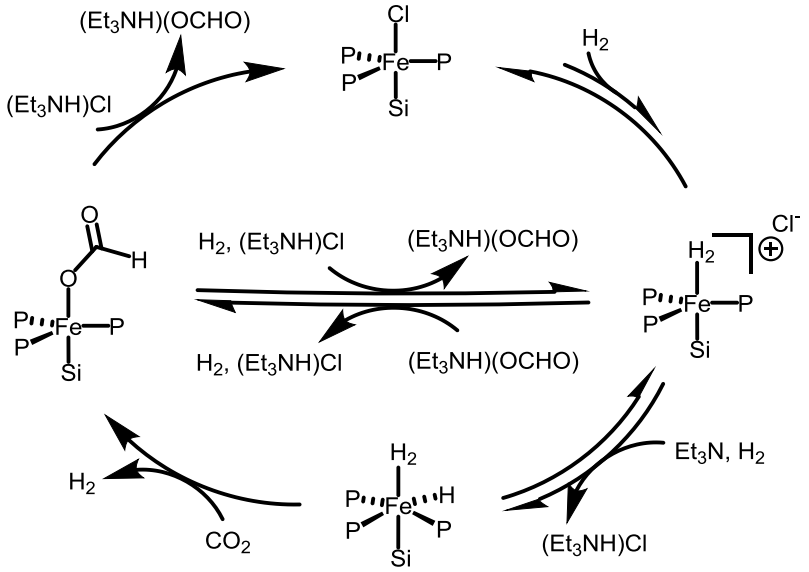

See Chart 4.1 for detailed ligand representation.

A possible catalytic cycle based in part on the observed stoichiometric reactions discussed in Scheme 4.4 is proposed in Scheme 4.5 for the (**SiP**$^{i\mathbf{Pr}}_{\mathbf{3}}$)Fe system. Starting from precatalyst (**SiP**$^{i\mathbf{Pr}}_{\mathbf{3}}$)FeCl in Scheme 4.5, dihydrogen substitution forms the cationic dihydrogen adduct [(**SiP**$^{i\mathbf{Pr}}_{\mathbf{3}}$)Fe($H_2$)]$^+$. The viability of this H_2 for Cl^- substitution step is demonstrated by H/D scrambling experiments discussed above. The cationic dihydrogen adduct [(**SiP**$^{i\mathbf{Pr}}_{\mathbf{3}}$)Fe($H_2$)]$^+$ in the catalytic cycle can be deprotonated by triethylamine to give (**SiP**$^{i\mathbf{Pr}}_{\mathbf{3}}$)Fe($H_2$)(H), as was observed in the stoichiometric reaction (Scheme 4.4e). The reverse of this reaction is also possible: a 1:1 mixture of (Et_3NH)Cl and (**SiP**$^{i\mathbf{Pr}}_{\mathbf{3}}$)Fe($H_2$)(H) reacts to afford (**SiP**$^{i\mathbf{Pr}}_{\mathbf{3}}$)FeCl (Scheme 4.4i).

The iron-hydride intermediate (**SiP**$^{i\mathbf{Pr}}_{\mathbf{3}}$)Fe($H_2$)(H) can then react with CO_2 to form the iron-formate complex (**SiP**$^{i\mathbf{Pr}}_{\mathbf{3}}$)Fe(OCHO), which can subsequently react with (Et_3NH)Cl and

reform (**SiP$^{iPr}_3$**)FeCl and release (Et_3NH)(OCHO). The direct conversion of (**SiP$^{iPr}_3$**)Fe(OCHO) to [(**SiP$^{iPr}_3$**)Fe(H_2)]$^+$ may also be a viable pathway, as chloride-free[(**SiP$^{iPr}_3$**)Fe(N_2)](BAr^F_4), (**SiP$^{iPr}_3$**)Fe(N_2)(H), and (**SiP$^{iPr}_3$**)Fe(OCHO) are catalytically competent. An alternative mechanism involving an iron-dihydride species cannot be ruled out but is unlikely for the (**SiP$^{iPr}_3$**)Fe system (Scheme 4.6a). A similar mechanism was proposed by Beller et al. for the cationic (**tetraphos**)Fe catalyst based on *in situ* NMR data, where the intermediate [(**tetraphos**)Fe(H_2)(H)]$^+$ was deprotonated by Et_3N to give (**tetraphos**)Fe($H)_2$ (Scheme 4.6b).[20] This iron-dihydride intermediate was suggested to react with CO_2 to give the iron-hydrido-formate intermediate (**tetraphos**)Fe(H)(OCHO). However, note that a dihydride intermediate in the (**SiP$^{iPr}_3$**)Fe system would be unlikely because the analogous deprotonaton of (**SiP$^{iPr}_3$**)Fe(H_2)(H) would form an anionic iron-dihydride species "[(**SiP$^{iPr}_3$**)Fe$(H)_2$]$^-$", which is likely to be thermodynamically inaccessible. For example, a solution of (**SiP$^{iPr}_3$**)Fe(H_2)(H) with excess triethylamine is stable for hours at 90 °C. While this does not rule out the possibility of an equilibrium mixture of (**SiP$^{iPr}_3$**)Fe(H_2)(H) and [(**SiP$^{iPr}_3$**)Fe$(H)_2$]$^-$, heavily favoring the neutral monohydride species, and note that the estimated pK_a of the H_2 and H^- ligands in (**SiP$^{iPr}_3$**)Fe(H_2)(H) is greater than 45 in THF,[49] vastly higher than for triethylamine ([Et_3NH]$^+$ pK_a = 12.5 in THF).[68]

It is of interest to compare the (**SiP$^{R}_3$**)Fe system to the catalytically incompetent (**TPB**)Fe system, since (**TPB**)(μ–H)Fe(N_2)(H) is an olefin hydrogenation catalyst.[44] A key step that may be required for catalysis is the substitution of Cl^- by H_2 in (**SiP$^{iPr}_3$**)FeCl to give the cationic dihydrogen adduct [(**SiP$^{iPr}_3$**)Fe(H_2)]$^+$. Deprotonation of the dihydrogen ligand in a C_6D_6:d_8-

Scheme 4.6 Dihydride pathways for catalytic CO_2 hydrogenation.

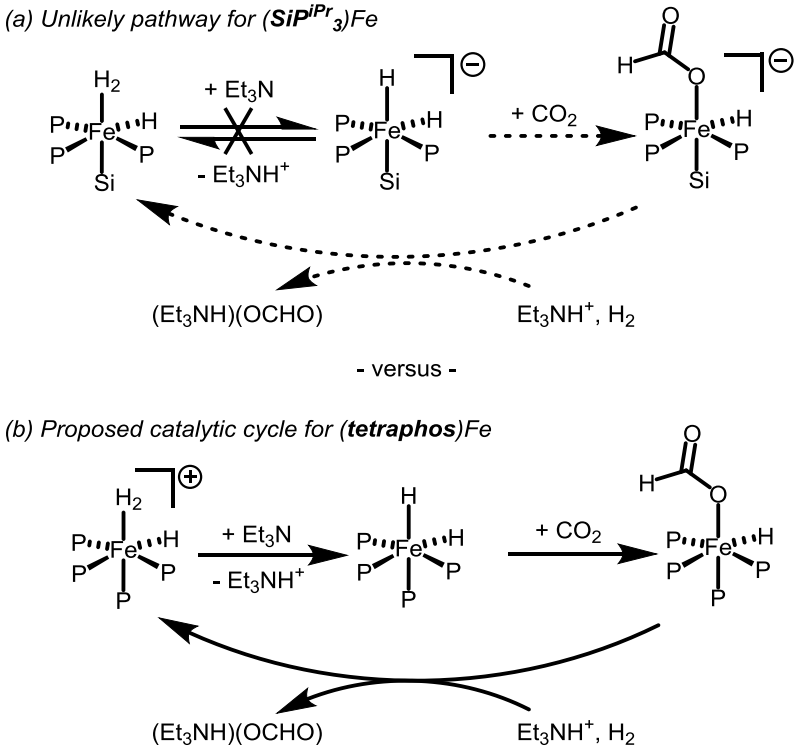

See Chart 4.1 for detailed representation of the ligands indicated.

THF mixture by triethylamine leads to the CO_2 reactive iron-hydride complex (**SiP**$^{\textbf{iPr}}_{\textbf{3}}$)Fe($H_2$)(H). The initial H_2 substitution step, therefore, is critical towards forming (**SiP**$^{\textbf{iPr}}_{\textbf{3}}$)Fe($H_2$)(H). However, the {Fe–B}^{7} complexes (**TPB**)Fe(OCHO) and (**TPB**)FeCl do not react with H_2 (4 atm). Related, the previously reported {Fe–B}^{7} [(**TPB**)Fe](BAr$^F{}_4$) complex,[41] which has a vacant fifth coordination site, does not react with H_2 in the presence of excess triethylamine under 1 atm of H_2 at 90 °C for 12 h. Furthermore, [(**TPB**)Fe](BAr$^F{}_4$) does not hydrogenate CO_2 under the catalytic conditions (see Appendix 3). [(**NP**$^{\textbf{iPr}}_{\textbf{3}}$)FeCl]($PF_6$) is not a hydrogenation precatalyst for possibly the same reason. Qualitatively, it appears that the inability of these latter systems to coordinate H_2, presumably a reflection of their weaker

ligand-field (LF) strengths by comparison to the SiP^R_3 system and hence their tendency to populate high spin configurations ([(**NP$^{iPr}_3$**)FeCl](PF$_6$), $S = 2$;[46] (**TPB**)FeCl, $S = 3/2$[58]), limits their efficacy towards CO_2 hydrogenation by comparison with the (**SiP$^R_3$**)Fe system ((**SiP$^{iPr}_3$**)FeCl, $S = 1$[55]). An additional factor preventing catalysis in the (**TPB**)Fe system is the unproductive loss of 0.5 equiv of H_2 following the reaction of (**TPB**)(μ–H)Fe(N_2)(H) with CO_2, which generates the catalytically incompetent (**TPB**)Fe(OCHO) (Scheme 4.3).

4.3.4 Influence of Hydricity on the Reaction with CO_2

Based only on the hydricity (54.3 ± 0.9 kcal/mol), the reaction of (**SiP$^{iPr}_3$**)Fe(H_2)(H) with CO_2 to afford formate (ΔG_H- = 43 kcal/mol) is endergonic by over 10 kcal/mol. However, comparisons of only the hydricities of the iron-hydride and formate neglect to take into account the observed formate coordination to iron (Scheme 4.2). To estimate the free energy afforded by formate coordination to iron, the formate binding constant was determined by UV-vis titration for the reaction of [(**SiP$^{iPr}_3$**)Fe(N_2)](BAr$^F_4$) and Li(OCHO) to (**SiP$^{iPr}_3$**)Fe(OCHO) (Scheme 4.7, equation 4.7). The titration in THF indicates that the binding constant of formate to the iron complex is on the order of 10^6 M^{-1}. This is equivalent to $\Delta G < -8$ kcal/mol for formate binding. Thus, the added driving force from formate coordination brings the free energy change for the reaction of (**SiP$^{iPr}_3$**)Fe(H_2)(H) and CO_2 to form (**SiP$^{iPr}_3$**)Fe(OCHO) to about 3 kcal/mol (Scheme 4.7, equation 4.10; from the sum of equations 4.7-4.9). This is thermally accessible at the elevated temperatures at which the stoichiometric and catalytic reactions are run.

Scheme 4.7 Gibbs free energies for the reactions of relevance to CO_2 hydrogenation by (**SiP$^{iPr}_3$**)Fe(H_2)(H)**.**

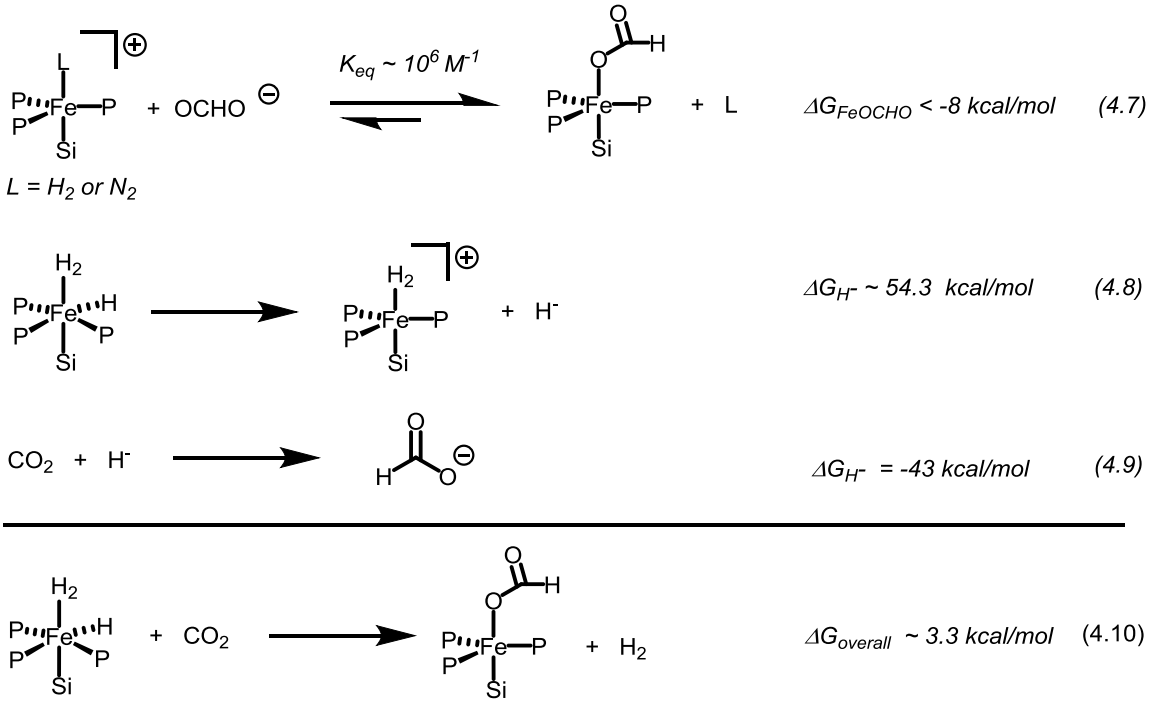

See Chart 4.1 for the detailed ligand representation.

It should be cautioned that (**SiP$^{iPr}_3$**)Fe(H_2)(H) may not be the actual iron-hydride intermediate that reacts with CO_2, i.e., an intermediate elementary step may occur prior to CO_2 reacting with the iron complex. The hydricity of such a species is likely different than (**SiP$^{iPr}_3$**)Fe(H_2)(H) owing to the trans-influencing Si^-. Also note that these hydricity values are for acetonitrile, while the catalytic reactions were run in methanol. The magnitude of the difference in hydricities between formate and metal-hydrides is known to decrease upon changing from acetonitrile to water.[69] A similar phenomenon may be occurring in methanol, where the difference in hydricity between (**SiP$^{iPr}_3$**)Fe(H_2)(H) and formate may not be as large

as the values in acetonitrile. This, combined with formate coordination to iron (Scheme 4.7, equation 4.7), may in fact make this formal CO_2 insertion step exergonic in methanol.

4.4 Conclusions

In summary, a series of *tris*-phosphino-iron-hydride complexes, including (**SiP$^{R}_{3}$**)Fe(L)(H), (**PhBP$^{iPr}_{3}$**)Fe(H)$_3$(PMe$_3$), [(**NP$^{iPr}_{3}$**)Fe(N$_2$)(H)](PF$_6$), and (**TPB**)(μ−H)Fe(N$_2$)(H), have been studied in the context of CO_2 hydrogenation. These iron-hydride complexes react with CO_2 to afford iron-formate complexes which can undergo metathesis with triethylammonium chloride to release triethylammonium formate and well-defined iron-chloride complexes, which are themselves synthons for the CO_2-reactive iron-hydride complexes (Scheme 4.2). Under the catalytic conditions under elevated pressures of H_2 and CO_2, (**SiP$^{iPr}_{3}$**)FeCl, (**SiP$^{Ph}_{3}$**)FeCl, and (**PhBP$^{iPr}_{3}$**)FeCl are precatalysts for catalytic CO_2 hydrogenation to formate and methylformate (Scheme 4.2). (**CP$^{iPr}_{3}$**)FeCl, in which carbon replaces the silicon-atom in (**SiP$^{iPr}_{3}$**)FeCl, was also a competent catalyst. The catalytic reactions proceeded in methanol but not in THF, highlighting the importance of solvent in the catalytic reaction. [60]

As depicted in Scheme 4.5, dihydrogen substitution into (**SiP$^{iPr}_{3}$**)FeCl or (**SiP$^{iPr}_{3}$**)Fe(OCHO) to form [(**SiP$^{iPr}_{3}$**)Fe(H$_2$)]$^+$ followed by deprotonation to form the CO_2-reactive (**SiP$^{iPr}_{3}$**)Fe(H$_2$)(H) are key steps in the catalytic cycle and determine catalytic competency. The proposed mechanism for (**SiP$^{iPr}_{3}$**)Fe also differs from the mechanism for the highly active (**tetraphos**)Fe system, which proceeds through a dihydride intermediate.

Finally, the hydricity value of an iron-hydride species has also been experimentally determined. The hydricity of (**SiP$^{iPr}_{3}$**)Fe(H$_2$)(H) is 54.3 ± 0.9 kcal/mol in acetonitrile, and the

estimated pK_a^{MeCN} of the related conjugate acid [(**SiP$^{iPr}_3$**)Fe(H_2)](BAr^F_4) is 15.9 ± 0.7. Despite the low hydricity, (**SiP$^{iPr}_3$**)Fe(H_2)(H) hydrogenates CO_2 to formate, and part of the driving force for the reaction is coordination of formate to the iron center. Thus, the free energy change for the reaction between (**SiP$^{iPr}_3$**)Fe(H_2)(H) and CO_2 to (**SiP$^{iPr}_3$**)Fe(OCHO) is only slightly uphill at 3 kcal/mol, and accessible under the reactions conditions. It will be of interest to measure the hydricities of other iron-hydrides, including within the present series of complexes, in the context of CO_2 hydrogenation to better understand the factors that may lead to improved catalytic activity.

4.5 Experimental

4.5.1 General Considerations

All manipulations were carried out using standard glovebox or Schlenk techniques under an N_2 atmosphere. Unless otherwise noted, solvents were deoxygenated and dried by thoroughly sparging with N_2 gas followed by passage through an activated alumina column in the solvent purification system by SG Water, USA LLC. Deuterated solvents and $^{13}CO_2$ gas were purchased from Cambridge Isotope Laboratories, INC. The deuterated solvents were degassed and dried over activated 3 Å sieves prior to use. Unless otherwise noted, all compounds were purchased commercially and used without further purification. (**SiP$^{iPr}_3$**)Fe(N_2)(H),[43] (**SiP$^{iPr}_3$**)FeCl,[55] [(**SiP$^{iPr}_3$**)Fe(N_2)](BAr^F_4),[37] (**SiP$^{Ph}_3$**)FeCl,[55] (**SiP$^{Ph}_3$**)FeMe,[55] (**PhBP$^{iPr}_3$**)Fe($H)_3$(PMe_3),[45] (**PhBP$^{iPr}_3$**)FeCl,[38] [(**NP$^{iPr}_3$**)Fe(N_2)(H)](PF_6),[46] [(**NP$^{iPr}_3$**)FeCl](PF_6),[46] (**TPB**)(μ–H)Fe(N_2)(H),[44] (**CP$^{iPr}_3$**)FeCl,[42] and (**C^{Si}P$^{Ph}_3$**)FeCl[47] were

synthesized by literature procedures. Elemental analyses were performed by Robertson Microlit Laboratories, Ledgewood, NJ.

NMR spectra were recorded on Varian 300 MHz, 400 MHz, and 500 MHz spectrometers. ^{1}H and ^{13}C chemical shifts are reported in ppm relative to residual solvent as internal standards. ^{31}P and ^{11}B chemical shifts are reported in ppm relative to 85 % aqueous H_3PO_4 and $BF_3{\cdot}Et_2O$, respectively. Multiplicities are indicated by br (broad), s (singlet), d (doublet), t (triplet), quart (quart), quin (quintet), m (multiplet), d-d (doublet-of-doublets), and t-d (triplet-of-doublets).

The ATR-IR measurements were performed in a glovebox on a thin film of the complex obtained from evaporating a drop of the solution on the probe surface of a Bruker APLHA ATR-IR Spectrometer (Platinum Sampling Module, diamond, OPUS software package) at 2 cm^{-1} resolution. IR intensities indicated by s (strong), m (medium), and w (weak).

UV-vis spectra were collected on a Cary 60 UV-Vis Spectrophotometer. The titration experiments were performed in a glovebox using an Ocean Optics HR4000CG Spectrometer.

H_2 quantification by GC-TCD: H_2 was quantified on an Agilent 7890A gas chromotograph (HP-PLOT U, 30 m, 0.32 mm i.d.; 30 °C isothermal; 1 mL/min flow rate; He carrier gas) using a thermal conductivity detector. The total amount of H_2 produced was determined as the sum of H_2 in the headspace plus dissolved H_2 in the solution calculated by Henry's law with a constant of 328 MPa.[70]

Methylformate quantification by GC-FID: Methylformate quantification was performed on a 1.2 mL aliquot of the crude reaction mixture by GC-FID against a methylformate calibration curve. GC-FID instrument: Hewlett Packard 5890 with a 57 m Restek RTX-VRX

column (0.32 mm inner diameter, 1.8 μm films). Method parameters: He carrier gas, 1 μL injection volume, 200 °C inlet temperature, 250 °C detector temperature, 7:1 split ratio, 2.9 mL/min flow rate, 20 psi pressure, 35 cm/s velocity. Ramp rate: 35 °C initial temperature held for 8 min, followed by 10 °C/min steps up to 100 °C, then immediately followed by 25 °C/min steps up to 230 °C, which was held for 4 min.

4.5.2 Synthetic Protocols

Synthesis of (SiP$^{iPr}_3$)FeMe from (SiP$^{iPr}_3$)FeCl. A yellow solution of (**SiP$^{iPr}_3$**)FeCl (44.4 mg, 73 μmol) in THF (10 mL) was cooled to -78 °C. A solution of MeMgCl (24 μL of a 3 M THF solution, 73 μmol) was diluted with THF (1 mL) and then added dropwise to the stirring reaction, causing a gradual change to a red solution. The stirring solution was allowed to warm to room temperature overnight. The crude mixture was filtered through a glass frit to remove black precipitate, and the volatiles were removed *in vacuo* to reveal a red solid. The material was taken up in a minimal amount of pentane and allowed to sit at -35 °C overnight, revealing red crystals of (**SiP$^{iPr}_3$**)FeMe (11.3 mg, 22 %). The ^{1}H and ^{31}P NMR spectra of this material were identical to the reported spectra.[55]

Synthesis of (SiP$^{iPr}_3$)Fe(OCHO). A yellow THF solution (10 mL) of (**SiP$^{iPr}_3$**)Fe(N_2)(H) (50 mg, 72 μmol) was degassed by freeze-pump-thaw cycles (3x). Subsequently, CO_2 (1 atm) was introduced to the thawed solution. The reaction was sealed and then heated for 1 h at 50 °C to give a yellow solution. The volatiles were removed *in vacuo* to give a yellow solid. The material was extracted with C_6H_6, and lyophilized to give (**SiP$^{iPr}_3$**)Fe(OCHO) as a yellow solid (46 mg, 90 %). Analytically pure material was obtained by layering a concentrated solution of

(**SiP$^{iPr}_3$**)Fe(OCHO) in THF (1 mL) under HMDSO (5 mL) and allowing the solution to sit at -35 °C for 3 days. ^{1}H NMR (C_6D_6, 400 MHz): δ 12.2, δ 12.1, δ 4.7, δ 4.6, δ 1.3, δ 0.2, δ -2.0, δ -2.2, δ -4.9. μ_{eff} (C_6D_6, method of Evans, 20 °C): 2.8 μ_B (S = 1). IR (thin film, cm^{-1}) 1623 (m, ν_{asym} (O–C–O)). UV-vis (THF, nm {M^{-1} cm^{-1}}) 357 {shoulder, 3247}, 426 {2243}, 478 {253}, 963 {br abs starting at 884 nm, 451}. Anal.: Calc'd for $C_{37}H_{55}FeO_2P_3Si$: C, 62.71; H, 7.82. Found: C, 61.81; H, 7.24.

Synthesis of (SiP$^{iPr}_3$)Fe(O^{13}CHO). The procedures used to synthesize (**SiP$^{iPr}_3$**)Fe(OCHO) were used here, except that $^{13}CO_2$ was used in place of CO_2. The ^{1}H NMR spectrum was identical to (**SiP$^{iPr}_3$**)Fe(OCHO). IR (thin film, cm^{-1}): 1583 (m, ν_{asym}(O–^{13}C–O)).

Synthesis of (SiP$^{Ph}_3$)Fe(N$_2$)(H). A procedure nearly identical to that used to synthesize **(SiP$^{iPr}_3$)**Fe(N$_2$)(H) was used to synthesize (**SiP$^{Ph}_3$**)Fe(N$_2$)(H). In a 100 mL Schlenk tube a red solution of (**SiP$^{Ph}_3$**)FeMe (26.3 mg, 30 μmol) in THF (20 mL) was degassed by freeze-pump-thaw cycles (3x). H_2 gas (1 atm) was charged into the thawed solution. The reaction was then sealed and heated to 60 °C for over a week. The reaction was then filtered through Celite and volatiles were removed *in vacuo* to give a light yellow powder. The solid was collected on a glass-frit and washed with pentane (3 mL x 2). The resulting product (**SiP$^{Ph}_3$**)Fe(N$_2$)(H) (24.4 mg, 91 %) was obtained as a light yellow powder after drying under vacuum. Layering a THF solution of (**SiP$^{Ph}_3$**)Fe(N$_2$)(H) under Et_2O and letting the solution stand for 2 days yields analytically pure powder of (**SiP$^{Ph}_3$**)Fe(N$_2$)(H). ^{1}H NMR (C_6D_6, 300 MHz): δ 8.55 (2H, d, $^2J_{H-H}$ = 6 Hz, Ar-*H*), δ 8.32 (2H, d, $^2J_{H-H}$ = 3 Hz, Ar-*H*), δ 7.62 (3H, br s, Ar-*H*), δ 7.45 (2H, br s, Ar-*H*), δ 7.34 (4H, d, $^2J_{H-H}$ = 6 Hz, Ar-*H*), δ 6.85 (2H, t, $^2J_{H-H}$ = 6 Hz, Ar-*H*), δ 6.69 (3H, q, $^2J_{H-}$

$_{H}$ = 3 Hz, Ar-*H*), δ 6.52 (2H, q, $^{2}J_{H-H}$ = 3 Hz, Ar-*H*), δ -11.88 (1H, t-d, $^{2}J_{P_{cis}-H}$ = 54 Hz, $^{2}J_{P_{trans}-H}$ = 12 Hz, Fe-*H*). ^{31}P NMR (C_6D_6, 121 MHz): 85.3 (2P, s), 78.7 (1P, s). ^{13}C NMR (THF with 1 drop of C_6D_6, 125 MHz): δ 156.3 (d, J_{C-P} = 38 Hz, C^{Ar}), δ 155.8 (d, J_{C-P} = 35 Hz, C^{Ar}), δ 150.7 (d, J_{C-P} = 5 Hz, C^{Ar}), δ 150.4 (s, C^{Ar}), δ 150.2 (s, C^{Ar}), δ 143.0 (s, C^{Ar}), δ 141.6 (d, J = 23 Hz, C^{Ar}), δ 141.0 (s, C^{Ar}), δ 139.6 (d, J = 28 Hz, C^{Ar}), δ 138.6 (d, J = 10, C^{Ar}), δ 133.8 (s, C^{Ar}) δ 132.6 (s, C^{Ar}), δ 132.3 (s, C^{Ar}), δ 129.5 (s, C^{Ar}), δ 128.4 (s, C^{Ar}), δ 128.2 (s, C^{Ar}), δ 128.1 (s, C^{Ar}), 127.5 (d, J = 5 Hz, C^{Ar}). IR (thin film, cm^{-1}): 2073 (s, ν(N≡N)), 1889 (w, ν(Fe–H)). UV-vis (THF, nm {M^{-1} cm^{-1}}) 335 {shoulder, 8125}, 437 {shoulder, 4500}. Anal.: Calc'd for $C_{54}H_{43}FeN_2P_3Si$: C, 72.32; H, 4.83; N, 3.12. Found: C, 72.94; H, 5.22; N, 2.83.

Synthesis of (SiP$^{Ph}_3$)Fe(OCHO). A yellow THF solution (10 mL) of (**SiP$^{Ph}_3$**)Fe(N_2)(H) (51 mg, 57 μmol) was degassed by freeze-pump-thaw cycles (3x). CO_2 (1 atm) was introduced to the thawed solution. The reaction was sealed and then heated for 1 h at 50 °C to give a yellow solution. The volatiles were removed *in vacuo* to give a yellow solid. The material was redissolved in C_6H_6 and filtered through a pipet filter to remove a small amount of black material. The filtrate was lyophilized *in vacuo* to give (**SiP$^{Ph}_3$**)Fe(OCHO) as a yellow solid (41 mg, 79 %). Analytically pure material was obtained by layering a concentrated THF solution of (**SiP$^{Ph}_3$**)Fe(OCHO) (3 mL) under pentane (5 mL) and allowing it to stand for 2 days at RT. ^{1}H NMR (3:2 mixture of C_6D_6:d_8-THF, 300 MHz): δ 12.2, δ 6.5, δ 5.7, δ 4.8, δ -2.1, δ -4.7. μ_{eff} (d_8-THF, method of Evans, 20 °C): 2.7 μ_B (S = 1). IR (thin film, cm^{-1}) 1618 (m, ν_{asym}(O–C–O)), 1316 (m, ν_{sym}(O–C–O)). UV-vis (THF, nm {M^{-1} cm^{-1}}) 325 {shoulder, 4775},

415 {4100}, 474 {3700}, 995 {br abs starting at 900 nm, 263}. Anal.: Calc'd for $C_{55}H_{43}FeO_2P_3Si$: C, 72.37; H, 4.75. Found: C, 73.21; H, 5.48.

Synthesis of (SiP$^{Ph}_3$)Fe(O^{13}CHO). The same procedures used to synthesize (**SiP$^{Ph}_3$**)Fe(OCHO) were used here, except that $^{13}CO_2$ was used in place of CO_2. The ^{1}H NMR spectrum of (**SiP$^{Ph}_3$**)Fe(O^{13}CHO) was identical to (**SiP$^{Ph}_3$**)Fe(OCHO). IR (thin film, cm^{-1}): 1587 (m, ν_{asym}(O–^{13}C–O)), 1254 (m, ν_{sym}(O–^{13}C–O)).

Synthesis of (PhBP$^{iPr}_3$)Fe(OCHO). A yellow THF solution (1 mL) of (**PhBP$^{iPr}_3$**)Fe(H)$_3$(PMe$_3$) (6.7 mg, 12 μmol) was degassed by freeze-pump-thaw cycles (3x). Subsequently, CO_2 (1 atm) was introduced to the thawed solution. The reaction was sealed and then stirred for 12 h at room temperature to give a light yellow solution. The volatiles were removed *in vacuo* to give an light yellow solid. The material was triterated with pentane, and the solvent was removed *in vacuo*. The material was then redissolved in C_6H_6 (3 mL) and filtered through a glass frit to remove a black solid. Removal of the solvent *in vacuo* gave (**PhBP$^{iPr}_3$**)Fe(OCHO) (4.7 mg, 70 %) as a light yellow solid. Analytically pure material was obtained by layering HDMSO on top of a THF solution of (**PhBP$^{iPr}_3$**)Fe(OCHO) and allowing it to stand overnight. ^{1}H NMR (C_6D_6, 300 MHz): δ 41.1, δ 19.9, δ 18.6, δ 13.5, δ 9.2, δ 4.5, δ 3.6, δ 1.6, δ -1.2, δ -11.2, δ -12.1, δ -32.6, δ -37.7. μ_{eff} (C_6D_6, method of Evans, 20 °C): 5.0 μ_B (S = 2). IR (thin film, cm^{-1}) 1595 (m, ν_{asym}(O–C–O)), 1362 (m, ν_{sym}(O–C–O)). UV-vis (THF, nm {M^{-1} cm^{-1}}) 298 {1173}, 410 {274}. Anal.: Calc'd for $C_{28}H_{54}FeO_2P_3$: C, 57.75; H, 9.35. Found: C, 58.12; H, 9.67.

Synthesis of (PhBP$^{iPr}_3$)Fe(O^{13}CHO). The same procedures used to synthesize (**PhBP$^{iPr}_3$**)Fe(OCHO) were used here, except that $^{13}CO_2$ was used in place of CO_2. The ^{1}H NMR spectrum of (**PhBP$^{iPr}_3$**)Fe(O^{13}CHO) was identical to (**PhBP$^{iPr}_3$**)Fe(OCHO). IR (thin film, cm^{-1}): 1546 (m, ν_{asym}(O–^{13}C–O)), 1355 (m, ν_{sym}(O–^{13}C–O)).

Synthesis of [(NP$^{iPr}_3$)Fe(OCHO)](PF$_6$). A yellow THF solution (10 mL) of [(**NP$^{iPr}_3$**)Fe(N$_2$)(H)](PF$_6$) (29 mg, 40 μmol) was degassed by freeze-pump-thaw cycles (3x). Subsequently, CO_2 (1 atm) was introduced. The reaction was then sealed and stirred for 3 h at room temperature to give a colorless solution. The solvent was removed *in vacuo* to give a colorless solid. The material was triturated with pentane, and the solvent was removed *in vacuo*. The solid was washed with diethyl ether (3 x 1 mL) to give [(**NP$^{iPr}_3$**)Fe(OCHO)](PF$_6$) (29 mg, 97 %) as a white solid. Analytically pure material was obtained by layering Et_2O on top of a THF solution of [(**NP$^{iPr}_3$**)Fe(OCHO)](PF$_6$) and allowing it to stand overnight at -35 °C. ^{1}H NMR (3:2 mixture of C_6D_6:d_8-THF, 300 MHz): δ 27.6, δ 9.4, δ 8.9, δ 6.4, δ 2.1, δ 1.9, δ 0.4, δ -8.3. ^{31}P NMR (3:2 mixture of C_6D_6:d_8-THF, 121 MHz): δ -144.4 (h, $^1J_{P\text{-}F}$ = 708 Hz, *P*F$_6$). ^{19}F NMR (3:2 mixture of C_6D_6:d_8-THF, 282 MHz): -73.4 (d, $^1J_{P\text{-}F}$ = 710 Hz, PF$_6$). μ_{eff} (C_6D_6, method of Evans, 20 °C): 5.1 μ_B (*S* = 2). IR (thin film, cm^{-1}) 1613 (m, ν_{asym}(O–C–O)). UV-vis (THF, nm {M^{-1} cm^{-1}}) 311 {shoulder, 660}, 379 {shoulder, 249}. Anal.: Calc'd for $C_{25}H_{55}F_6FeNO_2P_4$: C, 43.18; H, 7.97; N, 2.01. Found: C, 44.10; H, 8.25; N, 1.86.

Synthesis of [(NP$^{iPr}_3$)Fe(O^{13}CHO)](PF$_6$). The same procedures used to synthesize [(**NP$^{iPr}_3$**)Fe(OCHO)](PF$_6$) were used here, except that $^{13}CO_2$ was used in place of CO_2. The ^{1}H

NMR spectrum of [(**NP$^{iPr}_3$**)Fe(O^{13}CHO)](PF$_6$) was identical to [(**NP$^{iPr}_3$**)Fe(OCHO)](PF$_6$). IR (thin film, cm^{-1}): 1579 (m, ν_{asym}(O–^{13}C–O)).

Synthesis of (TPB)FeCl. The procedures used to synthesize (**TPB**)FeBr[58] were used to synthesize (**TPB**)FeCl, except that $FeCl_2$ was used in place of $FeBr_2$. A Schlenk tube was charged with TPB (117 mg, 172 μmol), $FeCl_2$ (26 mg, 200 μmol), Fe powder (113 mg, 2000 μmol), and THF (20 mL). The reaction was heated to 90 °C for 3 days with vigorous stirring, resulting in a color change of the liquid phase from light yellow to dark green-brown. The remaining iron powder was removed by filtration, and the solvent was removed *in vacuo*. The residue was taken up in toluene (5 mL), and the solvent was removed *in vacuo*. Pentane (200 mL) was added, and the mixture was stirred for 3 h and filtered. Removal of the solvent *in vacuo* yielded a yellow-brown powder of (**TPB**)FeCl (123 mg, 91 %). ^{1}H NMR (C_6D_6, 300 MHz): δ 97.6, δ 35.1, δ 23.6, δ 9.6, δ 5.8, δ 3.4, δ 1.9, δ -0.2 δ -2.3, δ -22.5. μ_{eff} (C_6D_6, method of Evans, 20 °C): 4.1 μ_B (S = 2). UV-vis (THF, nm {M^{-1} cm^{-1}}) 275 {14086}, 317 {10385}, 556 {sh, 80}, 774 {66}, 897 {91}. Anal.: Calc'd for $C_{36}H_{54}BClFeP_3$: C, 63.41; H, 7.98. Found: C, 64.06; H, 8.89.

Synthesis of (TPB)Fe(OCHO). A yellow benzene solution (6 mL) of (**TPB**)(μ–H)Fe(N_2)(H) (20.7 mg, 31 μmol) was degassed by freeze-pump-thaw cycles (3x). Subsequently, CO_2 (1 atm) was introduced. The reaction was then sealed and the yellow solution was mixed for 1 h at room temperature. The solvent was lyophilized *in vacuo* to give (**TPB**)Fe(OCHO) as a dark yellow solid (21.0 mg, 99 %). Analytically pure material was obtained by cooling a concentrated pentane solution of (**TPB**)Fe(OCHO) to -35 °C overnight.

^{1}H NMR (C_6D_6, 300 MHz): δ 86.1, δ 66.3, δ 38.5, δ 26.3, δ 15.5, δ 4.3, δ 2.7, δ 1.4, δ 1.0, δ -0.7, δ -2.6, δ -3.5, δ -24.1. μ_{eff} (C_6D_6, method of Evans, 20 °C): 4.2 μ_B (S = 2). IR (thin film, cm^{-1}): 1627 (m, ν_{asym}(O−C−O)), 1291 (m, ν_{sym}(O−C−O)). UV-vis (THF, nm {M^{-1} cm^{-1}}) 278 {16400}, 317 {12800}, 773 {br abs, 98}, 958 {127}. Anal.: Calc'd for $C_{37}H_{55}BFeO_2P_3$: C, 64.27; H, 8.02. Found: C, 63.16; H, 7.75.

Synthesis of (TPB)Fe(O^{13}CHO). The same procedures used to synthesize (**TPB**)Fe(OCHO) were used, except that $^{13}CO_2$ was used in place of CO_2. The ^{1}H NMR spectrum was identical to (**TPB**)Fe(OCHO). IR (thin film, cm^{-1}): 1588 (m, ν_{asym}(O–^{13}C–O)), 1269 (m, ν_{sym}(O–^{13}C–O)).

Reaction of (TPB)Fe(N_2) with formic acid. (**TPB**)Fe(N_2) (8.2 mg, 12.1 μmol) in 2 mL of THF was charged into a round bottom flask, and the flask was sealed with a rubber septum. Formic acid (3 μL, 80.3 μmol) was added by syringe through the septum, immediately resulting in effervescence of H_2 and a yellow-brown solution. The solution was allowed to stir for a few minutes before the volatiles were removed *in vacuo* to reveal a brown solid. The material was redissolved in benzene and filtered. Removal of the volatiles *in vacuo* revealed a brown powder of (**TPB**)Fe(OCHO) (8.1 mg, 96 %). NMR and IR spectral data for this material were identical to (**TPB**)Fe(OCHO).

Deprotonation of [(SiP$^{iPr}_3$)Fe(H_2)](BAr$^F_4$) with Et_3N. [(**SiP$^{iPr}_3$**)Fe(N_2)](BAr$^F_4$) (14.6 mg, 9.4 μmol) and triethylamine (1.7 μL, 9.7 μmol) were charged into an NMR tube with a J-young valve with C_6D_6 and d_8-THF (*ca.* 0.4 mL and 0.1 mL, respectively), yielding a green solution. The solution was degassed by freeze-pump-thaw cycles (3x), revealing an orange

solution consistent with [(**SiP$^{iPr}_3$**)Fe(THF)](BAr$^F_4$). H_2 (1 atm) was charged into the reaction mixture, yielding a transient gray solution (consistent with [(**SiP$^{iPr}_3$**)Fe(H_2)](BAr$^F_4$) that immediately changed to orange-yellow upon mixing. The reaction was mixed overnight. The NMR data of the iron-species in this reaction mixture were identical to (**SiP$^{iPr}_3$**)Fe(H_2)(H).[43] The volatiles were removed *in vacuo*, and the resulting yellow solid was extracted with pentane. The pentane was removed *in vacuo* to yield a yellow solid of (**SiP$^{iPr}_3$**)Fe(N_2)(H) (5.1 mg, 88 %). The ^{1}H and ^{31}P NMR spectra of this material are identical to (**SiP$^{iPr}_3$**)Fe(N_2)(H).

Quantifying H_2 loss from the reaction of (TPB)(μ–H)Fe(N_2)(H) with CO_2. Procedures similar to the synthesis of (**TPB**)Fe(OCHO) were followed. (**TPB**)(μ–H)Fe(N_2)(H) (20.0 mg, 31 μmol) was dissolved in 6 mL of benzene and charged into a calibrated 200 mL Schlenk tube that had a Teflon valve and 24/40 side joint. The solution was degassed by freeze-pump-thaw cycles (3x), opened to CO_2 (1 atm), and agitated for *ca.* 5 sec to ensure adequate dissolution of CO_2 into the solution. The reaction was then sealed at the Teflon valve joint and also with a rubber septum at the 24/40 joint. The reaction was stirred vigorously for 30 min, the Teflon valve was opened, and the headspace was sampled through the rubber septum with a 10 mL gastight syringe, being careful to ensure adequate mixing of the gases from reaction headspace into the 24/40 joint's headspace by repeated extraction and reinjection (3x) of the headspace gas with the gas-tight syringe before a final aliquot was taken for analysis by GC-TCD. 0.44 equiv of H_2 (relative to (**TPB**)(μ–H)Fe(N_2)(H)) found.

Quantifying H_2 loss from the reaction of (TPB)Fe(N_2) with formic acid. Procedures similar to the synthesis of (**TPB**)Fe(OCHO) from formic acid and (**TPB**)Fe(N_2) were

followed. (**TPB**)Fe(N_2) (24.5 mg, 36 μmol) in benzene (3 mL) was charged into a calibrated 100 mL round-bottomed flask and sealed with a rubber septum. Formic acid (1.3 μL, 36 μmol) was added by syringe. Effervescence was immediately visible. The reaction was allowed to stir for a few minutes before the headspace was sampled through the rubber septum with a 10 mL gastight syringe for analysis by GC-TCD. 0.42 equiv of H_2 (relative to (**TPB**)Fe(N_2)) found.

Metathesis reactions of iron-formate complexes with (Et_3NH)Cl. (Et_3NH)Cl (10 equiv) was charged into a methanol or benzene solution of (**SiP$^{iPr}_3$**)Fe(OCHO), (**SiP$^{Ph}_3$**)Fe(OCHO), (**PhBP$^{iPr}_3$**)Fe(OCHO), [(**NP$^{iPr}_3$**)Fe(OCHO)](PF_6), or (**TPB**)Fe(OCHO). The resulting suspension was stirred overnight and then filtered through a glass frit. The filtrate was concentrated *in vacuo* into a solid and then extracted. For (**SiP$^{iPr}_3$**)Fe(OCHO), (**SiP$^{Ph}_3$**)Fe(OCHO), (**PhBP$^{iPr}_3$**)Fe(OCHO), and (**TPB**)Fe(OCHO), pentane (3 x 1 mL) was used for extraction, while a 4:1 C_6H_6:THF mixture (3 x 1 mL) was used for [(**NP$^{iPr}_3$**)Fe(OCHO)](PF_6)). The respective ^{1}H NMR spectra and IR spectra of the extract showed conversion to (**SiP$^{iPr}_3$**)FeCl, (**SiP$^{Ph}_3$**)FeCl, (**PhBP$^{iPr}_3$**)FeCl, [(**NP$^{iPr}_3$**)FeCl](PF_6), or (**TPB**)FeCl.

4.5.3 CO_2 Hydrogenation Catalysis Protocols.

High pressure hydrogenation reactions were run in a Parr Instruments Company 4590 Micro Bench Top Reactor, with a 20 mL reaction vessel, controlled by a Parr Instruments Company 4834 Controller. In a typical catalytic run, iron precatalyst in 0.1 mL of THF (to solubilize iron precatalyst), 10 mL methanol, and 1 mL triethylamine was charged into the Parr reactor. The reactor was sealed, stirred with the attached mechanical stirrer (100 rpm), and charged with

CO_2 until the desired pressure at equilibrium was achieved (*ca.* 10 min). H_2 was subsequently added into the reactor. The gas inlet port was closed, and the reactor was then heated at 100 °C for 20 h. Changes to these conditions were made as described in Tables 4.2, 4.3, and 4.4 and Table A3.1 in Appendix 3. At the conclusion of the reaction, the reactor was cooled to 10 °C with an ice bath over *ca.* 1.5 h, and the pressure was slowly released through a needle valve. An aliquot of the crude solution was immediately taken for methylformate quantification by GC-FID. The aliquot was then recombined with the crude solution, DMF was added (1 mmol), and 25 μL of this solution was taken into 0.5 mL of CD_2Cl_2 for triethylammonium formate quantification by ^{1}H NMR spectroscopy.

Similar procedures were followed for the low pressure reactions (1 atm CO_2, 1-4 atm H_2), which were run in a 15 mL Schlenk tube having a Teflon valve. The solution was degassed by freeze-pump-thaw cycles (3x), and CO_2 (1 atm) was introduced into the vessel at room temperature. For the reactions requiring 4 atm of H_2, the entire body of the Schlenk tube was then cooled in a liquid-N_2 bath and 1 atm (RT) of H_2 was introduced. For reactions requiring 1 atm of H_2, the Schlenk tube was cooled with liquid-N_2 up to the solution level, and 1 atm (RT) of H_2 was introduced.

Analysis of iron-content post catalytic reaction. The reaction was worked up similar to the procedures described above for the hydrogenation runs. After depressurizing the reactor, it was brought into the glovebox for workup. The crude solution was transferred to a scintillation vial, and the volatiles were removed *in vacuo*. The resulting light yellow solid was dissolved in C_6D_6 and analyzed by ^{1}H and ^{31}P NMR spectroscopy.

4.5.4 Hydricity Determination

The hydricity was experimentally determined using the method present by DuBois.[50-51] The equilibrium of equation 4.3 (Scheme 4.2) with a given base (proton sponge, 2,6-lutidine, or 2,4,6-trimethylpyridine) was measured in d_8-THF. With proton sponge as base, [(**SiP$^{iPr}_3$**)Fe(N_2)](BAr$^F_4$) (8.0 mg, 5.1 μmol) was mixed with proton sponge (1.1 mg, 5.1 μmol) and the integration standard 1,3,5-trimethoxybenzene (1.2 mg, 7.1 μmol) in d_8-THF (0.5 mL). With 2,6-lutidine as base, [(**SiP$^{iPr}_3$**)Fe(N_2)](BAr$^F_4$) (8.7 mg, 5.6 μmol) was mixed with 2,6-lutidine (34 μL, 292 μmol) and the integration standard 1,3,5-trimethoxybenzene (1.1 mg, 6.5 μmol) in d_8-THF (0.5 mL). With 2,4,6-trimethylpyridine as base, [(**SiP$^{iPr}_3$**)Fe(N_2)](BAr$^F_4$) (8.3 mg, 5.3 μmol) was mixed with 2,4,6-trimethylpyridine (1.6 μL, 19.8 μmol) and the integration standard 1,3,5-trimethoxybenzene (1.3 mg, 7.7 μmol) with d_8-THF (0.5 mL). The solutions were degassed by freeze-pump-thaw cycles (3x) and H_2 (1 atm) was introduced. The solutions were mixed using a mechanical rotator at a rate of *ca.* 12 min^{-1}, and the reaction was monitored by ^{1}H NMR spectroscopy until equilibration: proton sponge, 6 days; 2,6-lutidine, 5 days; 2,4,6-trimethylpyridine, 5 days. Equations 4.3-4.5 were used to calculate ΔG_H-. The equilibrium between [(**SiP$^{iPr}_3$**)Fe(H_2)](BAr$^F_4$) and its THF-adduct [(**SiP$^{iPr}_3$**)Fe(H_2)](BAr$^F_4$) was also taken into account in the calculations (see Appendix 3).

4.5.5 UV-vis Titration of Formate Binding

The UV-vis titration experiments of [(**SiP$^{iPr}_3$**)Fe(N_2)](BAr$^F_4$) (4.8 mM) with Li(OCHO) (48 mM) in THF was performed by adding aliquots of the formate solution to a solution of the iron complex. The decay of [(**SiP$^{iPr}_3$**)Fe(N_2)](BAr$^F_4$) was monitored, with the absorbance at 752 nm

used for fitting to a quadratic equation against K_{eq}. After the addition of 1 eqv of Li(OCHO), a spectrum corresponding to (**SiP$^{iPr}_{3}$**)Fe(OCHO) was observed.

4.6 Cited References

(1) In *Carbon Dioxide as Chemical Feedstock*; Wiley-VCH Verlag GmbH & Co. KGaA: 2010.

(2) Olah, G. A. *Angew. Chem. Int. Ed.* **2013**, *52*, 104-107.

(3) Enthaler, S.; von Langermann, J.; Schmidt, T. *Energy Environ. Sci.* **2010**, *3*, 1207-1217.

(4) Arakawa, H.; Aresta, M.; Armor, J. N.; Barteau, M. A.; Beckman, E. J.; Bell, A. T.; Bercaw, J. E.; Creutz, C.; Dinjus, E.; Dixon, D. A.; Domen, K.; DuBois, D. L.; Eckert, J.; Fujita, E.; Gibson, D. H.; Goddard, W. A.; Goodman, D. W.; Keller, J.; Kubas, G. J.; Kung, H. H.; Lyons, J. E.; Manzer, L. E.; Marks, T. J.; Morokuma, K.; Nicholas, K. M.; Periana, R.; Que, L.; Rostrup-Nielson, J.; Sachtler, W. M. H.; Schmidt, L. D.; Sen, A.; Somorjai, G. A.; Stair, P. C.; Stults, B. R.; Tumas, W. *Chem. Rev.* **2001**, *101*, 953-996.

(5) Appel, A. M.; Bercaw, J. E.; Bocarsly, A. B.; Dobbek, H.; DuBois, D. L.; Dupuis, M.; Ferry, J. G.; Fujita, E.; Hille, R.; Kenis, P. J. A.; Kerfeld, C. A.; Morris, R. H.; Peden, C. H. F.; Portis, A. R.; Ragsdale, S. W.; Rauchfuss, T. B.; Reek, J. N. H.; Seefeldt, L. C.; Thauer, R. K.; Waldrop, G. L. *Chem. Rev.* **2013**, *113*, 6621-6658.

(6) Benson, E. E.; Kubiak, C. P.; Sathrum, A. J.; Smieja, J. M. *Chem. Soc. Rev.* **2009**, *38*, 89-99.

(7) Cokoja, M.; Bruckmeier, C.; Rieger, B.; Herrmann, W. A.; Kühn, F. E. *Angew. Chem. Int. Ed.* **2011**, *50*, 8510-8537.

(8) In *The Handbook of Homogeneous Hydrogenation*; Wiley-VCH Verlag GmbH: 2008.

(9) Jessop, P. G.; Ikariya, T.; Noyori, R. *Nature* **1994**, *368*, 231-233.

(10) Tanaka, R.; Yamashita, M.; Nozaki, K. *J. Am. Chem. Soc.* **2009**, *131*, 14168-14169.

(11) Graf, E.; Leitner, W. *J. Chem. Soc., Chem. Commun.* **1992**, 623-624.

(12) Lau, C. P.; Chen, Y. Z. *J. Mol. Catal. A: Chem.* **1995**, *101*, 33-36.

(13) Erlandsson, M.; Landaeta, V. R.; Gonsalvi, L.; Peruzzini, M.; Phillips, A. D.; Dyson, P. J.; Laurenczy, G. *Eur. J. Inorg. Chem.* **2008**, *2008*, 620-627.

(14) Huff, C. A.; Sanford, M. S. *J. Am. Chem. Soc.* **2011**, *133*, 18122-18125.

(15) Huff, C. A.; Sanford, M. S. *ACS Catal.* **2013**, 2412-2416.

(16) Schaub, T.; Paciello, R. A. *Angew. Chem. Int. Ed.* **2011**, *50*, 7278-7282.

(17) Wang, W.-H.; Muckerman, J. T.; Fujita, E.; Himeda, Y. *ACS Catal.* **2013**, *3*, 856-860.

(18) Langer, R.; Diskin-Posner, Y.; Leitus, G.; Shimon, L. J. W.; Ben-David, Y.; Milstein, D. *Angew. Chem. Int. Ed.* **2011**, *50*, 9948-9952.

(19) Federsel, C.; Boddien, A.; Jackstell, R.; Jennerjahn, R.; Dyson, P. J.; Scopelliti, R.; Laurenczy, G.; Beller, M. *Angew. Chem. Int. Ed.* **2010**, *49*, 9777-9780.

(20) Ziebart, C.; Federsel, C.; Anbarasan, P.; Jackstell, R.; Baumann, W.; Spannenberg, A.; Beller, M. *J. Am. Chem. Soc.* **2012**, *134*, 20701-20704.

(21) Evans, G. O.; Newell, C. J. *Inorg. Chim. Acta* **1978**, *31*, L387-L389.

(22) Tai, C.-C.; Chang, T.; Roller, B.; Jessop, P. G. *Inorg. Chem.* **2003**, *42*, 7340-7341.

(23) Inoue, Y.; Sasaki, Y.; Hashimoto, H. *J. Chem. Soc., Chem. Commun.* **1975**, 718-719.

(24) Haynes, P.; Slaugh, L. H.; Kohnle, J. F. *Tetrahedron Lett.* **1970**, *11*, 365-368.

(25) Federsel, C.; Ziebart, C.; Jackstell, R.; Baumann, W.; Beller, M. *Chem. Eur. J.* **2012**, *18*, 72-75.

(26) Jeletic, M. S.; Mock, M. T.; Appel, A. M.; Linehan, J. C. *J. Am. Chem. Soc.* **2013**, *135*, 11533-11536.

(27) Kumar, N.; Camaioni, D.; Dupuis, M.; Raugei, S.; Appel, A. M. *Dalton Trans.* **2014**, *43*, 11803-11106.

(28) Badiei, Y. M.; Wang, W.-H.; Hull, J. F.; Szalda, D. J.; Muckerman, J. T.; Himeda, Y.; Fujita, E. *Inorg. Chem.* **2013**, *52*, 12576-12586.

(29) Field, L. D.; Lawrenz, E. T.; Shaw, W. J.; Turner, P. *Inorg. Chem.* **2000**, *39*, 5632-5638.

(30) Allen, O. R.; Dalgarno, S. J.; Field, L. D. *Organometallics* **2008**, *27*, 3328-3330.

(31) Field, L. D.; Shaw, W. J.; Turner, P. *Chem. Commun.* **2002**, 46-47.

(32) Hills, A.; Hughes, D. L.; Jimenez-Tenorio, M.; Leigh, G. J. *J. Organomet. Chem.* **1990**, *391*, C41-C44.

(33) Bianco, V. D.; Doronzo, S.; Gallo, N. *Inorg. Nucl. Chem. Lett.* **1980**, *16*, 97-99.

(34) Bianco, V. D.; Doronzo, S.; Rossi, M. *J. Organomet. Chem.* **1972**, *35*, 337-339.

(35) Estes, D. P.; Vannucci, A. K.; Hall, A. R.; Lichtenberger, D. L.; Norton, J. R. *Organometallics* **2011**, *30*, 3444-3447.

(36) DuBois, D. L.; Berning, D. E. *Appl. Organomet. Chem.* **2000**, *14*, 860-862.

(37) Lee, Y.; Mankad, N. P.; Peters, J. C. *Nature Chem.* **2010**, *2*, 558-565.

(38) Betley, T. A.; Peters, J. C. *J. Am. Chem. Soc.* **2003**, *125*, 10782-10783.

(39) Betley, T. A.; Peters, J. C. *J. Am. Chem. Soc.* **2004**, *126*, 6252-6254.

(40) Anderson, J. S.; Rittle, J.; Peters, J. C. *Nature* **2013**, *501*, 84-87.

(41) Anderson, J. S.; Moret, M.-E.; Peters, J. C. *J. Am. Chem. Soc.* **2012**, *135*, 534-537.

(42) Creutz, S. E.; Peters, J. C. *J. Am. Chem. Soc.* **2013**, *136*, 1105-1115.

(43) Lee, Y.; Kinney, R. A.; Hoffman, B. M.; Peters, J. C. *J. Am. Chem. Soc.* **2011**, *133*, 16366-16369.

(44) Fong, H.; Moret, M.-E.; Lee, Y.; Peters, J. C. *Organometallics* **2013**, *32*, 3053-3062.

(45) Daida, E. J.; Peters, J. C. *Inorg. Chem.* **2004**, *43*, 7474-7485.

(46) MacBeth, C. E.; Harkins, S. B.; Peters, J. C. *Can. J. Chem.* **2005**, *83*, 332-340.

(47) Rittle, J.; Peters, J. C. *Proc. Natl. Acad. Sci. U. S. A.* **2013**, *110*, 15898-15903.

(48) Heinekey, D. M.; van Roon, M. *J. Am. Chem. Soc.* **1996**, *118*, 12134-12140.

(49) Morris, R. H. *J. Am. Chem. Soc.* **2014**, *136*, 1948-1959.

(50) Ciancanelli, R.; Noll, B. C.; DuBois, D. L.; DuBois, M. R. *J. Am. Chem. Soc.* **2002**, *124*, 2984-2992.

(51) Price, A. J.; Ciancanelli, R.; Noll, B. C.; Curtis, C. J.; DuBois, D. L.; DuBois, M. R. *Organometallics* **2002**, *21*, 4833-4839.

(52) Abdur-Rashid, K.; Fong, T. P.; Greaves, B.; Gusev, D. G.; Hinman, J. G.; Landau, S. E.; Lough, A. J.; Morris, R. H. *J. Am. Chem. Soc.* **2000**, *122*, 9155-9171.

(53) Chen, J. Z.; Szalda, D. J.; Fujita, E.; Creutz, C. *Inorg. Chem.* **2010**, *49*, 9380-9391.

(54) Gibson, D. H. *Coord. Chem. Rev.* **1999**, *185–186*, 335-355.

(55) Whited, M. T.; Mankad, N. P.; Lee, Y.; Oblad, P. F.; Peters, J. C. *Inorg. Chem.* **2009**, *48*, 2507-2517.

(56) Hill, A. F. *Organometallics* **2006**, *25*, 4741-4743.

(57) Parkin, G. *Organometallics* **2006**, *25*, 4744-4747.

(58) Moret, M.-E.; Peters, J. C. *Angew. Chem. Int. Ed.* **2011**, *50*, 2063-2067.

(59) Marks, T. J.; Kolb, J. R. *Chem. Rev.* **1977**, *77*, 263-293.

(60) Munshi, P.; Main, A. D.; Linehan, J. C.; Tai, C.-C.; Jessop, P. G. *J. Am. Chem. Soc.* **2002**, *124*, 7963-7971.

(61) Wesselbaum, S.; vom Stein, T.; Klankermayer, J.; Leitner, W. *Angew. Chem. Int. Ed.* **2012**, *51*, 7499-7502.

(62) Mellone, I.; Peruzzini, M.; Rosi, L.; Mellmann, D.; Junge, H.; Beller, M.; Gonsalvi, L. *Dalton Trans.* **2013**, *42*, 2495-2501.

(63) Saouma, C. T.; Lu, C. C.; Day, M. W.; Peters, J. C. *Chem. Sci.* **2013**, *4*, 4042-4051.

(64) Gambarotta, S.; Arena, F.; Floriani, C.; Zanazzi, P. F. *J. Am. Chem. Soc.* **1982**, *104*, 5082-5092.

(65) Bielinski, E. A.; Lagaditis, P. O.; Zhang, Y.; Mercado, B. Q.; Würtele, C.; Bernskoetter, W. H.; Hazari, N.; Schneider, S. *J. Am. Chem. Soc.* **2014**, *136*, 10234-10237.

(66) Drake, J. L.; Manna, C. M.; Byers, J. A. *Organometallics* **2013**, *32*, 6891-6894.

(67) Otera, J.; Nishikido, J. *Esterification*; Wiley-VCH Verlag GmbH & Co. KGaA, 2010.

(68) Kaljurand, I.; Kütt, A.; Sooväli, L.; Rodima, T.; Mäemets, V.; Leito, I.; Koppel, I. A. *J. Org. Chem.* **2005**, *70*, 1019-1028.

(69) Matsubara, Y.; Fujita, E.; Doherty, M. D.; Muckerman, J. T.; Creutz, C. *J. Am. Chem. Soc.* **2012**, *134*, 15743-15757.

(70) Brunner, E. *J. Chem. Eng. Data* **1985**, *30*, 269-273.

Appendix 1. Supplementary Data for Chapter 2

Table A1.5 Crystal data and structure refinement for (**TPB**)(μ–H)Fe(N_2)(H).

Identification code	Mem123a_cut	
Empirical formula	C36 H56 B Fe N2 P3	
Formula weight	676.40	
Temperature (K)	100(2)	
Wavelength (Å)	0.71073	
Crystal system	Monoclinic	
Space group	P2(1)/c	
Unit cell dimensions	a = 10.9690(10)	α = 90.00
	b = 15.8820(14)	β = 102.446(4)
	c = 120.7040(18)	γ = 90.00
Volume	3522.1(5)	
Z	4	
Density (Mg/m^3; calculated)	1.276	
Absorption coefficient	0.592	
F(000)	1444	
Crystal size (mm)	0.42 x 0.17 x 0.04	
Theta range for data collection (degrees)	1.63 to 28.27	
Index ranges	$-14 \leq h \leq 14, -21 \leq k \leq 21, -27 \leq l \leq 26$	
Reflections collected	64963	
Independent reflections	8699	
Completeness to theta = 28.27°	99.6 %	
Absorption correction	Multi-scan	
Max. and min transmission	0.7890 to 0.8767	
Refinement method	Full-matrix least squares on F^2	
Data/restraints/parameters	8699/0/406	
Goodness-of-fit on F^2	1.035	
Final R indices [I > 2sigma(I)]	R = 0.0505, wR2 = 0.1111	
R indices (all data)	R = 0.0865, wR2 = 0.1264	
Largest diff. peak and hole	0.086 and -0.619 $eÅ^{-3}$	

Table A1.6 Crystal data and structure refinement for (**TPB**)(μ–H)Fe(H_2)(H).

Identification code	hf12	
Empirical formula	C36 H56 B Fe N2 P3	
Formula weight	676.40	
Temperature (K)	100(2)	
Wavelength (Å)	0.71073	
Crystal system	Monoclinic	
Space group	P2(1)/n	
Unit cell dimensions	a = 10.6196(6)	α = 90.00
	b = 21.3418(13)	β = 94.019(4)
	c = 15.6111(9)	γ = 90.00
Volume	3529.4(4)	
Z	4	
Density (Mg/m^3; calculated)	1.218	
Absorption coefficient	0.586	
F(000)	1388	
Crystal size (mm)	0.28 x 0.16 x 0.15	
Theta range for data collection (degrees)	1.91 to 39.27	
Index ranges	$-17 \leq h \leq 18, -37 \leq k \leq 37, -26 \leq l \leq 27$	
Reflections collected	187522	
Independent reflections	20034	
Completeness to theta = 25.00°	95.9 %	
Absorption correction	Multi-scan	
Max. and min transmission	0.8530 to 0.9157	
Refinement method	Full-matrix least squares on F^2	
Data/restraints/parameters	20034/0/286	
Goodness-of-fit on F^2	1.056	
Final R indices [I > 2sigma(I)]	R = 0.0548, wR2 = 0.1270	
R indices (all data)	R = 0.1021, wR2 = 0.1511	
Largest diff. peak and hole	1.822 and -1.288 $eÅ^{-3}$	

Table A1.7 Crystal data and structure refinement for (**TPB**)Fe(CN^{t}Bu).

Identification code	Mem129	
Empirical formula	C43 H69 B Fe N P3 Si0.5	
Formula weight	774.61	
Temperature (K)	100(2)	
Wavelength (Å)	0.71073	
Crystal system	Rhombohedral	
Space group	R-3	
Unit cell dimensions	a = 11.2415(3)	α = 90.00
	b = 11.2415(3)	β = 90.00
	c = 59.3261(18)	γ = 120.00
Volume	6492.7(3)	
Z	6	
Density (Mg/m^3; calculated)	1.187	
Absorption coefficient	0.503	
F(000)	2502	
Crystal size (mm)	0.37 x 0.22 x 0.05	
Theta range for data collection (degrees)	2.06 to 30.04	
Index ranges	$-15 \leq h \leq 15$, $-14 \leq k \leq 15$, $-83 \leq l \leq 83$	
Reflections collected	46175	
Independent reflections	4245	
Completeness to theta = 30.04°	99.9 %	
Absorption correction	Multi-scan	
Max. and min transmission	0.8359 to 0.9753	
Refinement method	Full-matrix least squares on F^2	
Data/restraints/parameters	4225/88/257	
Goodness-of-fit on F^2	1.082	
Final R indices [I > 2sigma(I)]	R = 0.0611, wR2 = 0.1562	
R indices (all data)	R = 0.0771, wR2 = 0.1683	
Largest diff. peak and hole	0.079 and -1.970 eÅ^{-3}	

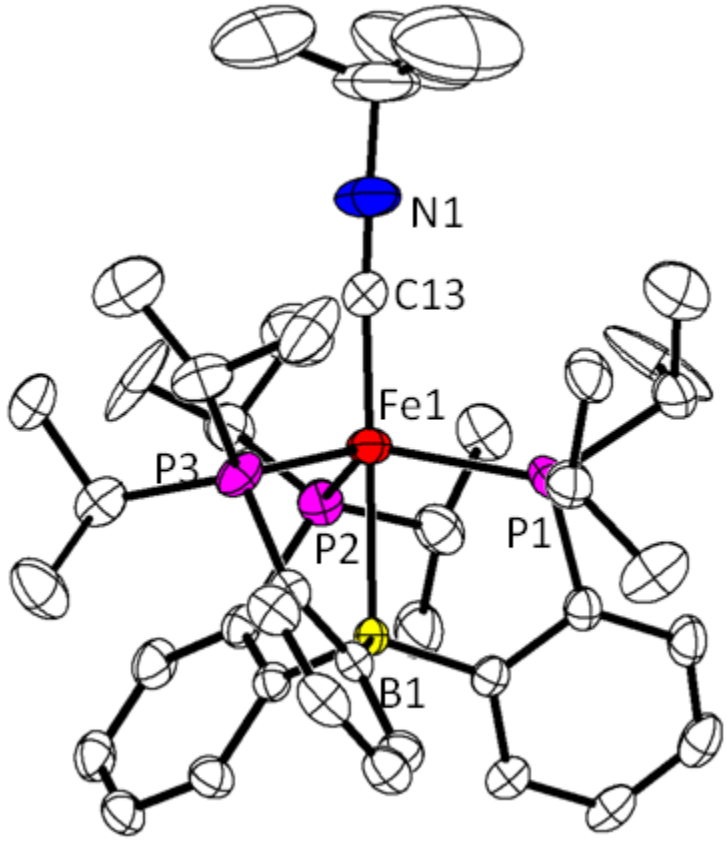

Figure A1.1 XRD structure of (**TPB**)Fe(CN^{t}Bu). Ellipsoids shown at 50 % probability. The CN^{t}Bu unit is disordered over three positions, and therefore the Fe−C13 and C13−N1 bond distance are reported as an average of the three Fe−C13 and three C13−N1 positions, respectively. Selected bond distances (Å) and angles (°): Fe1−P1 = 2.3193(7), Fe−P2 = 2.3193(7), Fe−P3 = 2.3194(7), 2.320(4), Fe−C13(avg) = 1.861(7), C13−N1(avg) = 1.179(9), Fe1−B1 = 2.340(4), ∑(P−Fe−P) = 345.03(1).

Table A1.8 Crystal data and structure refinement for (**TPB**)(μ–H)Fe(CN^{t}Bu)(H).

Identification code	Hf15	
Empirical formula	C41 H65 B Fe N P3	
Formula weight	731.51	
Temperature (K)	100(2)	
Wavelength (Å)	0.71073	
Crystal system	Orthorhombic	
Space group	Pna2(1)	
Unit cell dimensions	a = 28.1082(11)	α = 90.00
	b = 11.7188(5)	β = 90.00
	c = 12.0896(5)	γ = 90.00
Volume	3982.2(3)	
Z	4	
Density (Mg/m^3; calculated)	1.220	
Absorption coefficient	0.528	
F(000)	1576	
Crystal size (mm)	0.27 x 0.25 x 0.12	
Theta range for data collection (degrees)	2.22 to 35.72	
Index ranges	$-45 \leq h \leq 45$, $-19 \leq k \leq 18$, $-19 \leq l \leq 19$	
Reflections collected	125477	
Independent reflections	17351	
Completeness to theta = 25.00°	99.9 %	
Absorption correction	Multi-scan	
Max. and min transmission	0.8705 to 0.9393	
Refinement method	Full-matrix least squares on F^2	
Data/restraints/parameters	17351/1/447	
Goodness-of-fit on F^2	1.441	
Final R indices [I > 2sigma(I)]	R = 0.0369, wR2 = 0.0807	
R indices (all data)	R = 0.0531, wR2 = 0.0878	
Largest diff. peak and hole	0.799 and -0.297 eÅ^{-3}	

Table A1.9 Crystal data and structure refinement for (**TPB**)Fe(C_2H_4).

Identification code	Hf16	
Empirical formula	C38 H58 B Fe P3	
Formula weight	731.51	
Temperature (K)	100(2)	
Wavelength (Å)	0.71073	
Crystal system	Triclinic	
Space group	P-1	
Unit cell dimensions	a = 11.7652(5)	α = 112.296(2)
	b = 18.1293(8)	β = 90.626(2)
	c = 18.8179(8)	γ = 105.264(3)
Volume	3555.0(3)	
Z	4	
Density (Mg/m^3; calculated)	1.260	
Absorption coefficient	0.585	
F(000)	1448	
Crystal size (mm)	0.29 x 0.24 x 0.22	
Theta range for data collection (degrees)	1.88 to 44.33	
Index ranges	$-22 \leq h \leq 22, -35 \leq k \leq 35, -36 \leq l \leq 36$	
Reflections collected	285706	
Independent reflections	55462	
Completeness to theta = 44.33°	98.0 %	
Absorption correction	Multi-scan	
Max. and min transmission	0.8487 to 0.8821	
Refinement method	Full-matrix least squares on F^2	
Data/restraints/parameters	55462/0/831	
Goodness-of-fit on F^2	1.030	
Final R indices [I > 2sigma(I)]	R = 0.0428, wR2 = 0.1232	
R indices (all data)	R = 0.0761, wR2 = 0.1475	
Largest diff. peak and hole	2.925 and -0.791 $eÅ^{-3}$	

Table A1.10 Crystal data and structure refinement for (**TPBH**)Fe(C_2Tol).

Identification code	Hf36	
Empirical formula	C45 H62 B Fe N P3	
Formula weight	761.51	
Temperature (K)	100(2)	
Wavelength (Å)	0.71073	
Crystal system	Monoclinic	
Space group	P2(1)/c	
Unit cell dimensions	a = 25.3343(11)	α = 90.00
	b = 15.1553(6)	β = 113.176(2)
	c = 23.4782(1)	γ = 90.00
Volume	8287.0(6)	
Z	8	
Density (Mg/m^3; calculated)	1.222	
Absorption coefficient	0.510	
F(000)	3264	
Crystal size (mm)	0.41 x 0.30 x 0.18	
Theta range for data collection (degrees)	1.60 to 37.28	
Index ranges	$-43 \leq h \leq 42$, $-25 \leq k \leq 25$, $-39 \leq l \leq 38$	
Reflections collected	256649	
Independent reflections	41264	
Completeness to theta = 25.00°	96.0 %	
Absorption correction	Multi-scan	
Max. and min transmission	0.8182 to 0.9138	
Refinement method	Full-matrix least squares on F^2	
Data/restraints/parameters	41264/0/927	
Goodness-of-fit on F^2	1.239	
Final R indices [I > 2sigma(I)]	R = 0.0671, wR2 = 0.1565	
R indices (all data)	R = 0.1171, wR2 = 0.1824	
Largest diff. peak and hole	4.308 and -0.756 $eÅ^{-3}$	

Table A1.11 Crystal data and structure refinement for **D**.

Identification code	Hf31	
Empirical formula	C48 H81 B Fe P4	
Formula weight	854.44	
Temperature (K)	100(2)	
Wavelength (Å)	0.71073	
Crystal system	Monoclinic	
Space group	C2/c	
Unit cell dimensions	a = 14.7183(8)	α = 90.00
	b = 22.2944(13)	β = 103.864(3)
	c = 14.8410(9)	γ = 90.00
Volume	4728.0(5)	
Z	8	
Density (Mg/m^3; calculated)	1.200	
Absorption coefficient	0.486	
F(000)	1840	
Crystal size (mm)	0.33 x 0.30 x 0.24	
Theta range for data collection (degrees)	1.69 to 48.29	
Index ranges	$-30 \leq h \leq 30$, $-46 \leq k \leq 46$, $-30 \leq l \leq 30$	
Reflections collected	143163	
Independent reflections	22688	
Completeness to theta = 48.29°	98.9 %	
Absorption correction	Multi-scan	
Max. and min transmission	0.8561 to 0.8923	
Refinement method	Full-matrix least squares on F^2	
Data/restraints/parameters	22688/0/265	
Goodness-of-fit on F^2	0.928	
Final R indices [I > 2sigma(I)]	R = 0.0373, wR2 = 0.0885	
R indices (all data)	R = 0.0668, wR2 = 0.1027	
Largest diff. peak and hole	1.332 and -0.854 $eÅ^{-3}$	

Table A1.12 Crystal data and structure refinement for (**SiP$^{i\mathbf{Pr}}_{\mathbf{3}}$**)Fe(CO(H).

Identification code	D8_08027_0m	
Empirical formula	C27 H55 Fe P3 Si	
Formula weight	692.66	
Temperature (K)	100(2)	
Wavelength (Å)	1.54178	
Crystal system	Monoclinic	
Space group	C2/c	
Unit cell dimensions	a = 36.5798(8)	α = 90.00
	b = 11.7777(3)	β = 104.2430(1)
	c = 17.1309(4)	γ = 90.00
Volume	7153.6(3)	
Z	8	
Density (Mg/m^3; calculated)	1.286	
Absorption coefficient	5.715	
F(000)	2960	
Crystal size (mm)	0.25 x 0.20 x 0.15	
Theta range for data collection (degrees)	2.49 to 68.95	
Index ranges	$-43 \leq h \leq 44$, $-13 \leq k \leq 14$, $-20 \leq l \leq 20$	
Reflections collected	50397	
Independent reflections	6480	
Completeness to theta = 68.95°	98.8 %	
Absorption correction	Multi-scan	
Max. and min transmission	0.3578 to 0.5107	
Refinement method	Full-matrix least squares on F^2	
Data/restraints/parameters	6580/0/44	
Goodness-of-fit on F^2	1.046	
Final R indices [I > 2sigma(I)]	R = 0.0273, wR2 = 0.0693	
R indices (all data)	R = 0.0290, wR2 = 0.0703	
Largest diff. peak and hole	0.439 and -0.287 $eÅ^{-3}$	

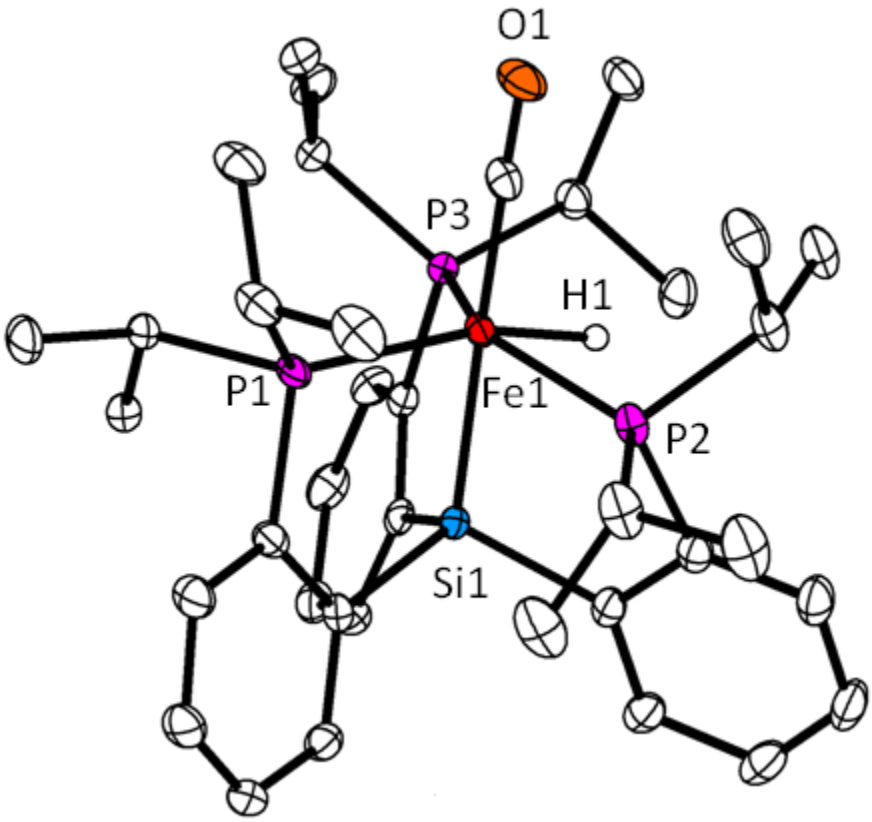

Figure A1.2 XRD structure of (**SiP$^{iPr}_{3}$**)Fe(CO)(H). Ellipsoids shown at 50 % probability. Selected bond distances (Å) and angles (°): Fe1−P1 = 2.2559(4), Fe1−P2 = 2.2495(4), Fe1−P3 = 2.2214(4), Fe1−H1 = 1.43(2), Fe1−C11 = 1.768(2), Fe1−Si1 = 2.2567(4), P3−Fe1−P1 = 106.05(2), P1−Fe1−P2 = 110.27(2), P2−Fe1−H1 = 66.4(1), P3−Fe1−H1 = 73.4(1).

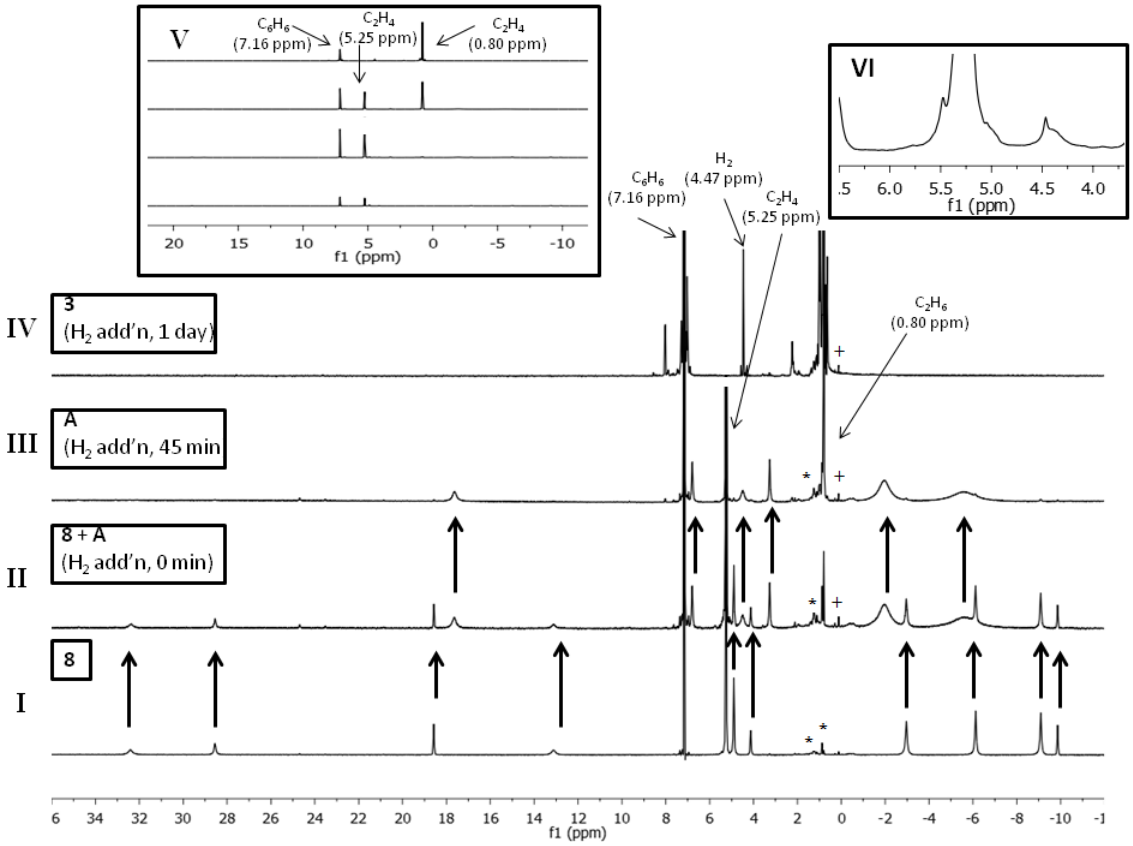

Figure A1.3 Stacked ^{1}H NMR spectra of the reaction of (**TPB**)Fe(C_2H_4) with H_2 (1 atm) and C_2H_4 (1 atm) in C_6D_6. (I) Compound (**TPB**)Fe(C_2H_4) under a C_2H_4 atmosphere. (II) Mixture of compounds (**TPB**)Fe(C_2H_4) and **A** immediately following H_2 addition. (III) Compound **A** was formed after mixing the reaction for *ca*. 45 min; H_2 was added to replenish the consumed H_2. (IV) Compound (**TPB**)(μ−H)Fe(H_2)(H) was formed at the conclusion of the reaction. (inset V) Zoom out of spectra. (inset VI) Zoom in to show the H_2 resonance. *Residual pentane. $^{+}$Residual silicon grease.

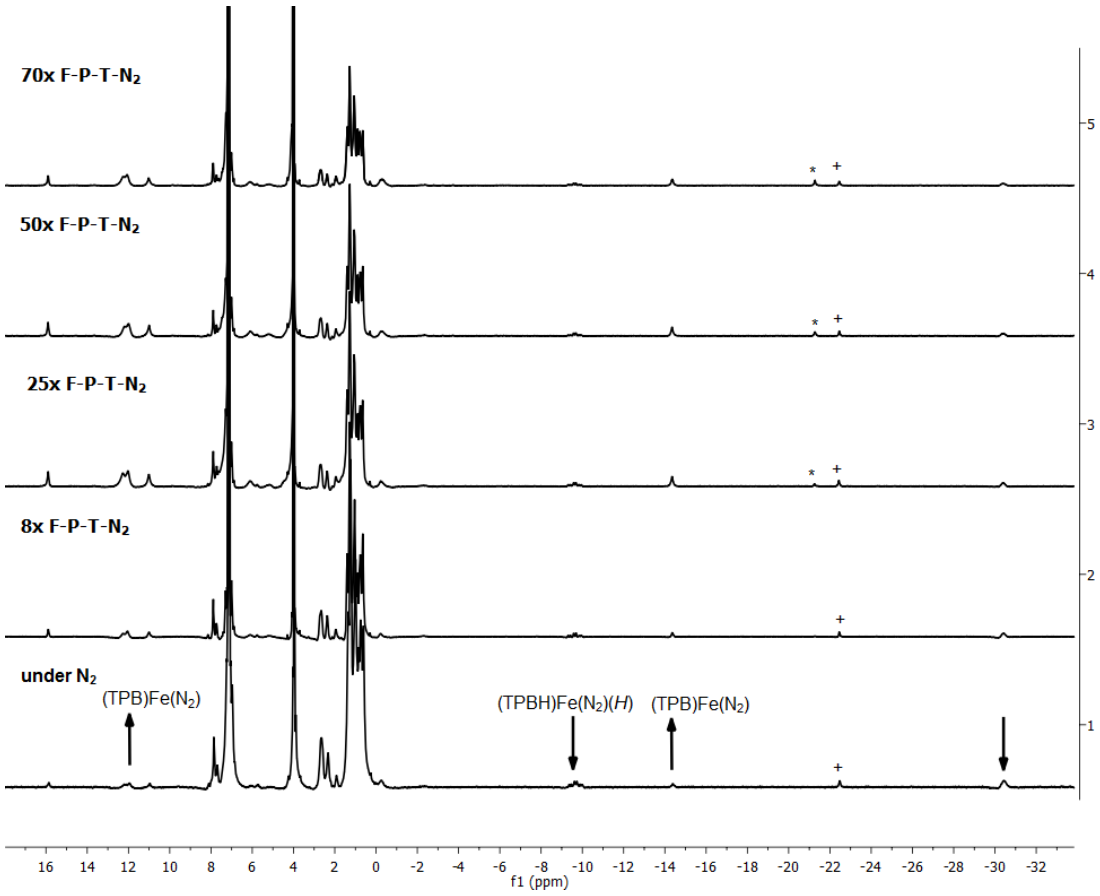

Figure A1.4 Elimination of H_2 from (**TPB**)(μ-H)Fe(N_2)(H). Iterative freeze-pump-thaw-N_2 cycles were performed to promote H_2 release and reformation of (**TPB**)Fe(N_2). Ferrocence (δ 4.0) was used as an integration standard. $^{+}$Residual (**TPB**)FeBr (previously reported). *(**TPB**)FeCl, known decomposition product from (**TPB**)Fe(N_2).

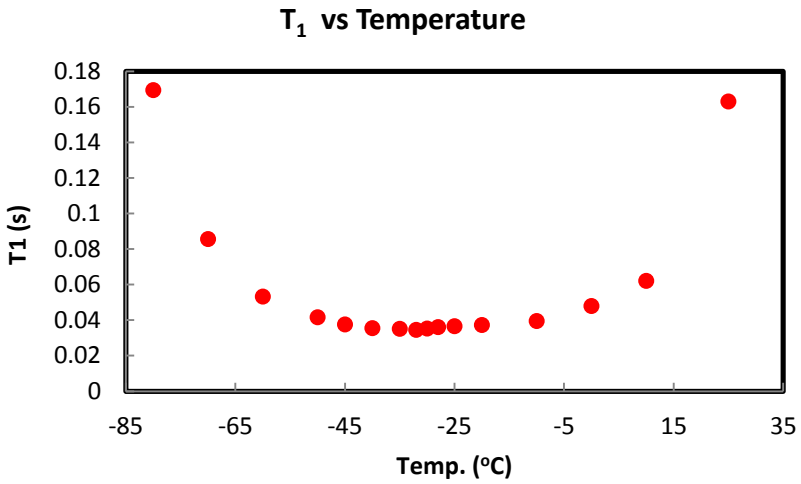

Figure A1.5 T_1 values for (**TPB**)(μ–H)Fe(H_2)(H) (d_8-toulene). T_{1min} is 35 ms at -32 °C.

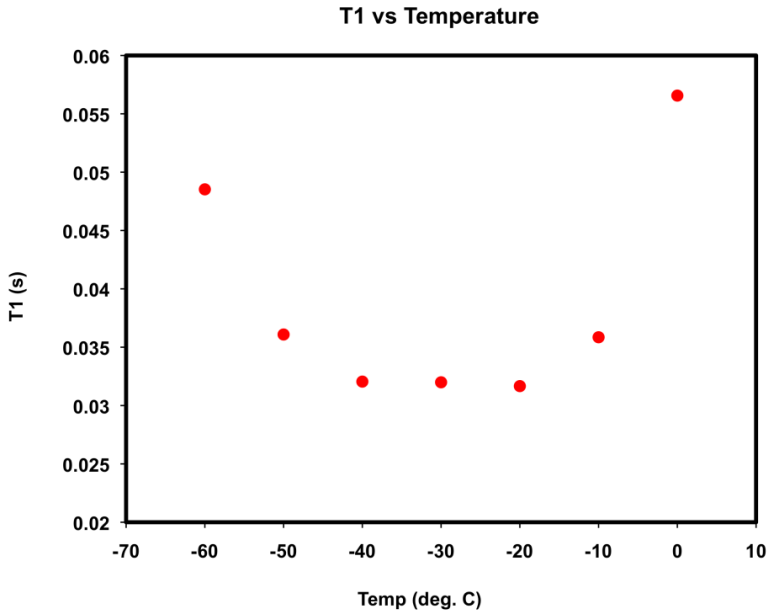

Figure A1.6 T_1 values for (**SiP$^{iPr}_3$**)Fe(H_2)(H) (d_8-toluene). T_{1min} is 32 ms at -30 °C.

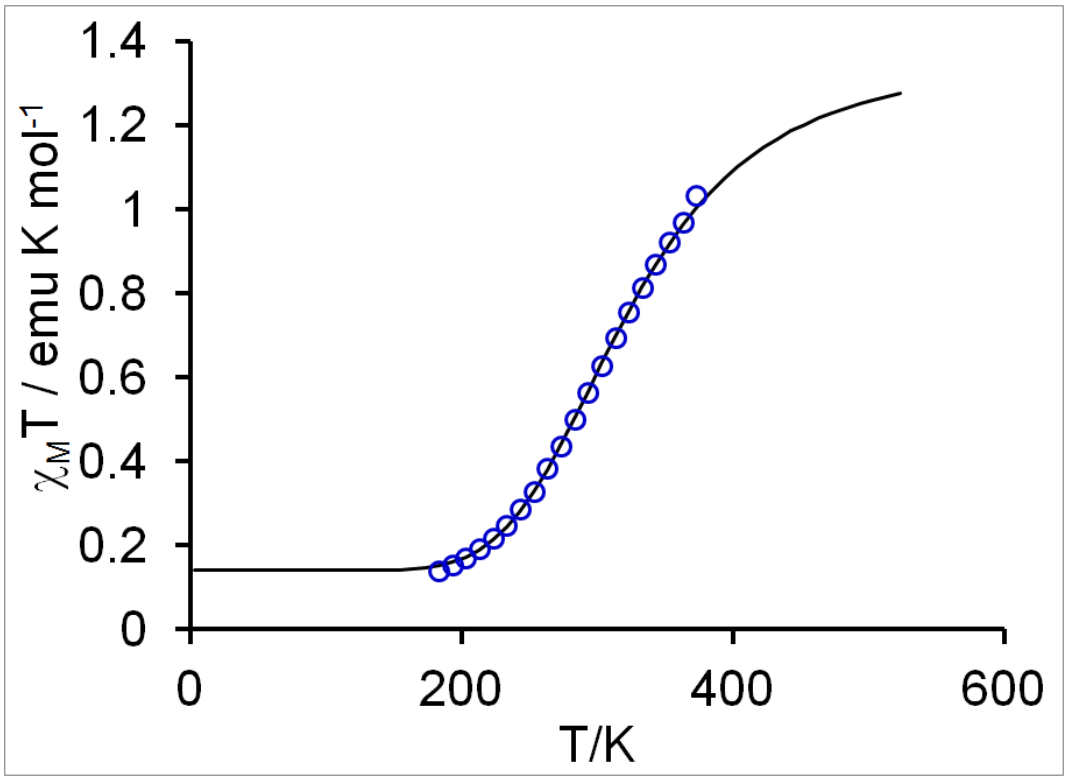

Figure A1.7 Variable temperature magnetic susceptibility measurements (method of Evans) of (**TPB**)Fe(CN^{t}Bu).

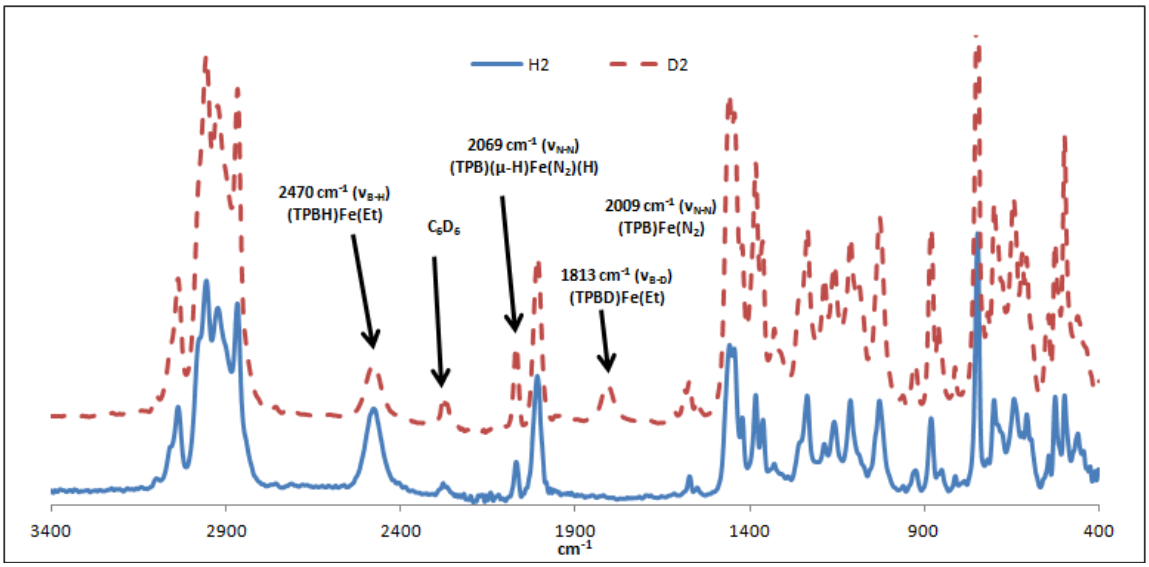

Figure A1.8 ATR-IR (THF thin film) of **A**, (**TPBH**)Fe(Et), (blue) and labeled (**TPBD**)Fe(Et) (red) generated from reaction of (**TPB**)Fe(C_2H_4) with H_2 or D_2, respectively. In the (**TPBD**)Fe(Et) spectrum, the 2470 cm^{-1} signal assigned to the B–H stretch of (**TPBH**)Fe(Et) is attributed to facile scrambling of B–D with the hydrogen atoms of the isopropyl groups from the ligand. The 2009 cm^{-1} signal is assigned to the N–N stretch of (**TPB**)Fe(N_2) is attributed to the decomposition of the (**TPBH**)Fe(Et) and (**TPBD**)Fe(Et) to ethane and (**TPB**)Fe(N_2).

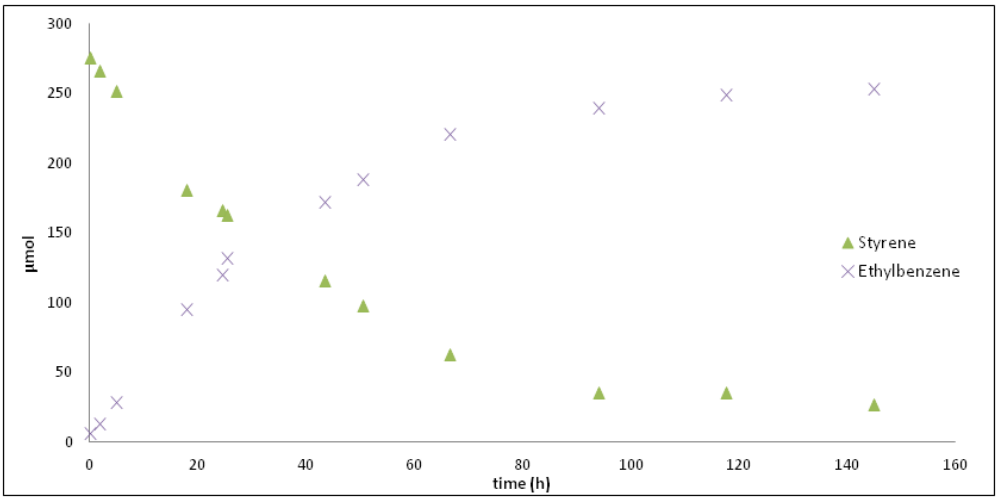

Figure A1.9 Catalytic hydrogenation of styrene with (**TPB**)Fe(N_2). Amounts of styrene and ethylbenzene were determined by ^{1}H NMR spectroscopy with ferrocene as an integration standard.

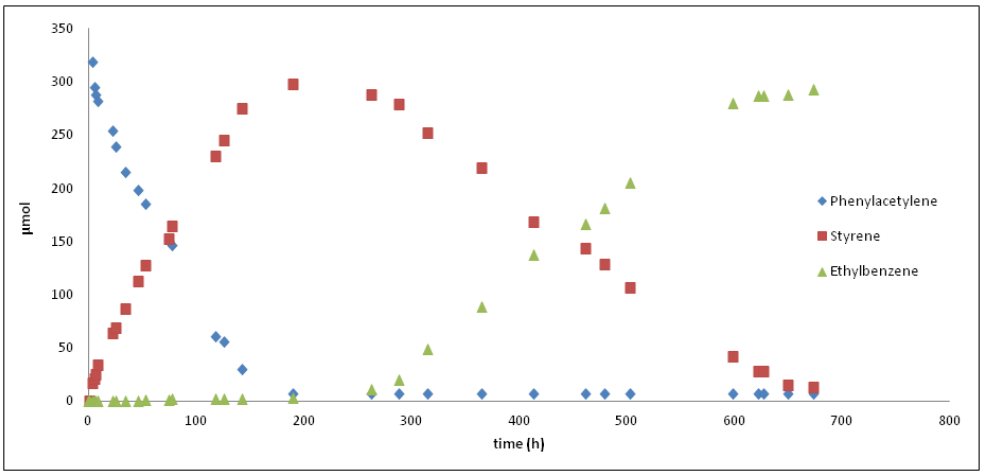

Figure A1.10 Catalytic hydrogenation of phenylacetylene with (**TPB**)Fe(N_2). Amounts of phenylacetylene, styrene, and ethylbenzene were determined by ^{1}H NMR spectroscopy with ferrocene as an integration standard.

Appendix 2. Supplementary Data for Chapter 3

Table A2.1 Crystal data and neutron structure refinement for (**TPB**)Co(H_2).

Identification code	tpbcoh2	
Empirical formula	C36 H55.86 B Br0.07 Co P3	
Formula weight	656.96	
Temperature (K)	100(2)	
Wavelength (Å)	0.4 - 3.5	
Crystal system	Triclinic	
Space group	P-1	
Unit cell dimensions	a = 10.8535(2)	α = 91.474(2)
	b = 11.2160(2)	β = 101.653(2)
	c = 16.7367(3)	γ = 118.930(2)
Volume	1728.21(7)	
Z	2	
Density (Mg/m^3; calculated)	1.264	
Absorption coefficient	The linear absorption coefficient is wavelength dependent and is calculated as: $\mu = 1.543 + 1.718 * \lambda$ [cm^{-1}]	
F(000)	108	
Crystal size (mm)	1.50 x 1.00 x 0.75	
Theta range for data collection (degrees)	7.48 to 79.21	
Index ranges	$-19 \leq h \leq 19$, $-20 \leq k \leq 20$, $-30 \leq l \leq 30$	
Reflections collected	26012	
Independent reflections	26004	
Completeness to theta = 78.21°	13.60 %	
Absorption correction	sphere	
Max. and min transmission	0.4574 to 0.7915	
Refinement method	Full-matrix least squares on F^2	
Data/restraints/parameters	26012/912/11	
Goodness-of-fit on F^2	1.115	
Final R indices [I > 2sigma(I)]	R = 0.0664, wR2 = 0.1288	
R indices (all data)	R = 0.0664, wR2 = 0.1288	
Largest diff. peak and hole	0.946 and -0.927 $eÅ^{-3}$	

Table A2.2 Crystal data and neutron structure refinement for (**SiP$^{iPr}_3$**)Fe(H_2).

Identification code	sip3feh2	
Empirical formula	C36 H55.52 C10.35 Fe P3 Si	
Formula weight	677.44	
Temperature (K)	100(2)	
Wavelength (Å)	0.4 - 3.5	
Crystal system	Triclinic	
Space group	P-1	
Unit cell dimensions	a = 11.0481(1)	α = 92.332(1)
	b = 11.3328(1)	β = 100.440(1)
	c = 16.8023(2)	γ = 119.636(2)
Volume	1777.26(3)	
Z	2	
Density (Mg/m^3; calculated)	1.266	
Absorption coefficient	The linear absorption coefficient is wavelength dependent and is calculated as: $\mu = 1.543 + 1.718 * \lambda$ [cm^{-1}]	
F(000)	128.0	
Crystal size (mm)	1.20 x 0.60 x 0.42	
Theta range for data collection (degrees)	7.48 to 79.21	
Index ranges	$-19 \leq h \leq 20$, $-20 \leq k \leq 20$, $-31 \leq l \leq 30$	
Reflections collected	26367	
Independent reflections	26352	
Completeness to theta = 25.00°	76.8 %	
Absorption correction	sphere	
Max. and min transmission	0.7837 to 0.9157	
Refinement method	Full-matrix least squares on F^2	
Data/restraints/parameters	26367/949/19	
Goodness-of-fit on F^2	1.072	
Final R indices [I > 2sigma(I)]	R = 0.0548, wR2 = 0.1148	
R indices (all data)	R = 0.0548, wR2 = 0.1148	
Largest diff. peak and hole	0.848 and -0.818 $eÅ^{-3}$	

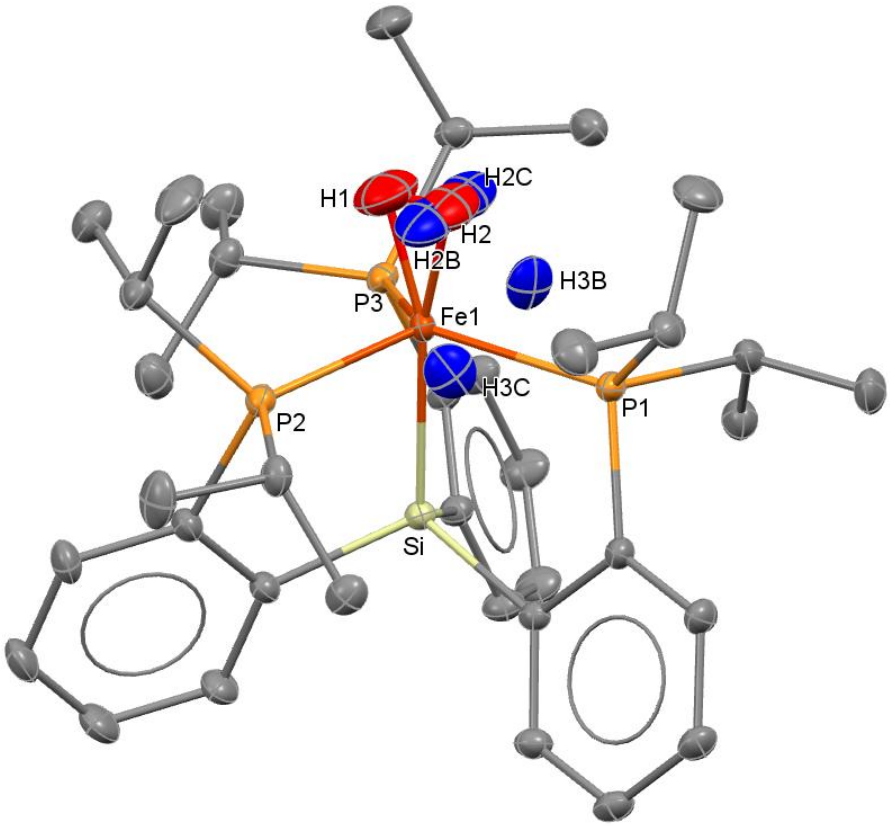

Figure A2.1 Solid state neutron diffraction structure of (**SiP$^{iPr}_{3}$**)Fe(H_2). The structure is disordered. The hydride and H_2 ligands of the disordered components are shown. The majority component (45 %) is the (**SiP$^{iPr}_{3}$**)Fe(H_2) (blue H atoms). The remaining components are (**SiP$^{iPr}_{3}$**)Fe(H_2)(H) (red H atom) and (**SiP$^{iPr}_{3}$**)FeCl (not shown).

Appendix 3. Supplementary Data for Chapter 4

Table A3.1 Catalytic hydrogenation results for (**SiP**$^{\mathbf{R}}_{\mathbf{3}}$)Fe, (**PhBP**$^{\mathbf{iPr}}_{\mathbf{3}}$)Fe, (**NP**$^{\mathbf{iPr}}_{\mathbf{3}}$)Fe, (**TPB**)Fe, (**CP**$^{\mathbf{iPr}}_{\mathbf{3}}$)Fe, (**C**$^{\mathbf{Si}}$**P**$^{\mathbf{Ph}}_{\mathbf{3}}$)Fe, **PP**$_{\mathbf{3}}$/Fe$(BF_4)_2$, and [(**tetraphos**)FeF](BF_4).

Entry	Precatalyst	$(Et_3NH)(OCHO)$ Yield (mmol)	MeOCHO Yield (mmol)	Total Yield (mmol)	$(Et_3NH)(OCHO)$ TON[a]	MeOCHO TON[a]	Total TON[a]	Solvent	P_{CO_2}/P_{H_2} (atm)	Additive[b]	Time (h)	Temp. (°C)
S1	(**SiP**$^{\mathbf{iPr}}_{\mathbf{3}}$)FeCl	0.00	0.00	0.00	0.00	0.00	0.00	THF	1/1		50	100
S2	(**SiP**$^{\mathbf{iPr}}_{\mathbf{3}}$)FeCl	0.00	0.00	0.00	0.00	0.00	0.00	THF	1/4		21	100
S3	(**SiP**$^{\mathbf{iPr}}_{\mathbf{3}}$)FeCl	0.00	0.00	0.00	0.00	0.00	0.00	MeOH	1/4		40	60
S4	(**SiP**$^{\mathbf{iPr}}_{\mathbf{3}}$)FeCl	0.00	0.00	0.00	0.00	0.00	0.00	THF	29/29		20	100
S5	(**SiP**$^{\mathbf{iPr}}_{\mathbf{3}}$)FeCl	0.31	0.14	0.45	39.60	18.20	57.80	MeOH	29/29		20	100
S6	(**SiP**$^{\mathbf{iPr}}_{\mathbf{3}}$)FeCl	0.31	0.13	0.44	37.90	15.30	53.20	MeOH	29/29		20	100
S7	(**SiP**$^{\mathbf{iPr}}_{\mathbf{3}}$)FeCl	0.31	0.08	0.40	37.90	10.55	48.45	MeOH	29/29		20	100
S8	(**SiP**$^{\mathbf{iPr}}_{\mathbf{3}}$)FeCl	0.14	0.00	0.14	17.40	0.00	17.40	MeOH	29/29		2	100
S9	(**SiP**$^{\mathbf{iPr}}_{\mathbf{3}}$)FeCl	0.12	0.00	0.12	15.25	0.00	15.25	MeOH	29/29		2	100
S10	(**SiP**$^{\mathbf{iPr}}_{\mathbf{3}}$)FeCl	0.26	0.10	0.35	32.54	12.20	44.74	MeOH	29/29		20	150
S11	(**SiP**$^{\mathbf{iPr}}_{\mathbf{3}}$)FeCl	0.18	0.11	0.29	22.63	13.98	36.61	MeOH	29/29		20	150
S12	(**SiP**$^{\mathbf{iPr}}_{\mathbf{3}}$)FeCl	0	0	0	0	0	0	MeOH	29/29		20	20
S13	(**SiP**$^{\mathbf{iPr}}_{\mathbf{3}}$)FeCl	0	0	0	0	0	0	MeOH	29/29		20	20
S14[c]	(**SiP**$^{\mathbf{iPr}}_{\mathbf{3}}$)FeCl	0.15	0.12	0.27	18.73	14.98	33.71	CD_3OD	29/29		20	100

Entry	Precatalyst	$(Et_3NH)(OCHO)$ Yield (mmol)	MeOCHO Yield (mmol)	Total Yield (mmol)	$(Et_3NH)(OCHO)$ TON[a]	MeOCHO TON[a]	Total TON[a]	Solvent	P_{CO_2}/P_{H_2} (atm)	Additive[b]	Time (h)	Temp. (°C)
S15[c]	(**SiP**$^{iPr}_3$)FeCl	0.16	0.08	0.24	19.40	10.10	29.50	CD_3OD	29/29		20	100
S16	(**SiP**$^{iPr}_3$)FeCl	0.27	0.05	0.32	34.90	6.36	41.26	MeOH	29/29	0.5 equiv $(Et_3NH)Cl$	20	100
S17	(**SiP**$^{iPr}_3$)FeCl	0.26	0.06	0.32	33.30	7.28	40.58	MeOH	29/29	0.5 equiv $(Et_3NH)Cl$	20	100
S18	(**SiP**$^{iPr}_3$)FeCl	0.68	0.15	0.83	86.31	18.90	105.21	MeOH	29/29	0.5 equiv $NaBF_4$	20	100
S19	(**SiP**$^{iPr}_3$)FeCl	0.59	0.05	0.64	75.12	6.26	81.38	MeOH	29/29	0.5 equiv $NaBF_4$	20	100
S20	(**SiP**$^{iPr}_3$)FeCl	0.31	0.28	0.59	38.1	34.6	72.7	MeOH	29/29	0.5 equiv $NaBAr^F_4$	20	100
S21	(**SiP**$^{iPr}_3$)FeCl	0.37	0.17	0.54	45.1	20.6	65.7	MeOH	29/29	0.5 equiv $NaBAr^F_4$	20	100
S22	(**SiP**$^{iPr}_3$)FeCl	0.31	0.03	0.34	39.0	4.3	44.3	MeOH	29/29	0.5 equiv NaF	20	100
S23	(**SiP**$^{iPr}_3$)FeCl	0.31	0.05	0.35	39.0	6.4	45.4	MeOH	29/29	0.5 equiv NaF	20	100
S24	(**SiP**$^{iPr}_3$)FeCl	0.16	0.02	0.18	20.4	2.9	23.3	MeOH	29/29	0.5 equiv CsF	20	100
S25	(**SiP**$^{iPr}_3$)FeCl	0.19	0.02	0.21	25.0	2.9	27.9	MeOH	29/29	0.5 equiv CsF	20	100
S26[d]	(**SiP**$^{iPr}_3$)FeCl	0.22	0.01	0.23	28.5	1.4	29.9	MeOH	29/29	0.5 equiv TBAF	20	100
S27[d]	(**SiP**$^{iPr}_3$)FeCl	0.24	0.03	0.27	31.1	3.9	35.0	MeOH	29/29	0.5 equiv TBAF	20	100
S28	(**SiP**$^{iPr}_3$)FeCl	0.39	0.03	0.42	50.2	4.4	54.6	MeOH	29/29	0.5 equiv K_2CO_3	20	100
S29	(**SiP**$^{iPr}_3$)FeCl	0.45	0.01	0.46	58.3	1.7	60.0	MeOH	29/29	0.5 equiv K_2CO_3	20	100
S30	(**SiP**$^{iPr}_3$)FeCl	0.00	0.00	0.007	0.00	0.0	0.00	MeOH	29/0		20	100

Entry	Precatalyst	$(Et_3NH)(OCHO)$ Yield (mmol)	MeOCHO Yield (mmol)	Total Yield (mmol)	$(Et_3NH)(OCHO)$ TON[a]	MeOCHO TON[a]	Total TON[a]	Solvent	P_{CO_2}/P_{H_2} (atm)	Additive[b]	Time (h)	Temp. (°C)
S31	(**SiP**$^{iPr}_3$)Fe(N_2)(H)	0.32	0.08	0.40	41.53	9.74	51.27	MeOH	29/29		20	100
S32	(**SiP**$^{iPr}_3$)Fe(N_2)(H)	0.25	0.09	0.34	31.79	11.83	43.62	MeOH	29/29		20	100
S33	(**SiP**$^{iPr}_3$)Fe(OCHO)	0.39	0.02	0.41	51.66	2.43	54.09	MeOH	29/29		20	100
S34	(**SiP**$^{iPr}_3$)Fe(OCHO)	0.36	0.03	0.39	46.98	3.22	50.20	MeOH	29/29		20	100
S35	(**SiP**$^{Ph}_3$)FeCl	0.94	0.56	1.51	121.55	72.71	194.26	MeOH	29/29		20	100
S36	(**SiP**$^{Ph}_3$)FeCl	1.08	0.52	1.59	139.36	66.44	205.44	MeOH	29/29		20	100
S37	[(**SiP**$^{iPr}_3$)Fe](BAr$^F_4$)	0.10	0.03	0.13	12.72	3.82	16.54	MeOH	29/29		20	100
S38	[(**SiP**$^{iPr}_3$)Fe](BAr$^F_4$)	0.13	0.00	0.15	16.30	2.80	19.10	MeOH	29/29		20	100
S39	(**SiP**$^{iPr}_3$)FeCl	0.39	0.03	0.42	48.69	3.75	52.44	MeOH	29/29	Hg	20	100
S40	(**SiP**$^{iPr}_3$)FeCl	0.33	0.00	0.38	41.00	6.24	47.24	MeOH	29/29	Hg	20	100
S41	**HSiP**$^{iPr}_3$/$FeCl_2$ (1:1)	0.08	0.03	0.11	9.68	3.10	12.78	MeOH	29/29		20	100
S42	**HSiP**$^{iPr}_3$/$FeCl_2$ (1:1)	0.10	0.02	0.12	11.98	1.82	13.80	MeOH	29/29		20	100
S43	(**PhBP**$^{iPr}_3$)FeCl	0.24	0.02	0.26	29.00	3.10	32.10	MeOH	29/29		20	100
S44	(**PhBP**$^{iPr}_3$)FeCl	0.15	0.02	0.17	19.00	2.40	21.40	MeOH	29/29		20	100
S45	[(**NP**$^{iPr}_3$)FeCl](PF_6)	0.00	0.00	0.00	0.00	0.00	0.00	MeOH	29/29		20	100
S46	(**TPB**)FeCl	0.00	0.00	0.00	0.00	0.00	0.00	MeOH	29/29		20	100

Entry	Precatalyst	$(Et_3NH)(OCHO)$ Yield (mmol)	MeOCHO Yield (mmol)	Total Yield (mmol)	$(Et_3NH)(OCHO)$ TON[a]	MeOCHO TON[a]	Total TON[a]	Solvent	P_{CO_2}/P_{H_2} (atm)	Additive[b]	Time (h)	Temp. (°C)
S47	[(**TPB**)Fe](BAr$^F_4$)	0.00	0.00	0.00	0.00	0.00	0.00	MeOH	29/29		20	100
S48	(**TPB**)μ–H)Fe(N_2)(H)	0.00	0.00	0.00	0.00	0.00	0.00	MeOH	29/29		20	100
S49	**PP_3**/Fe(BF_4)$_2$	3.30	0.91	4.21	395.70	108.50	504.20	MeOH	29/29		20	100
S50	**PP_3**/Fe(BF_4)$_2$	2.69	0.98	3.67	342.24	124.68	466.92	MeOH	29/29		20	100
S51	[(**tetraphos**)-Fe(F)](BF_4)	6.06	7.68	13.74	771.30	976.50	1747.80	MeOH	29/29		20	100
S52	[(**tetraphos**)-Fe(F)](BF_4)	5.15	7.23	12.38	655.22	919.85	1575.07	MeOH	29/29		20	100
S53	$FeCl_2$	0.00	0.00	0.00	0.00	0.00	0.00	MeOH	29/29		20	100
S54	$FeCl_2$/4 PPh_3	0.00	0.00	0.00	0.00	0.00	0.00	MeOH	29/29		20	100
S55	no iron	0.00	0.00	0.00	0.00	0.00	0.00	MeOH	29/29		20	100
S56	(**SiP$^{iPr}_3$**)Fe(N_2)(H)	0.00	0.00	0.00	0.00	0.00	0.00	THF	1/1		20	60
S57	(**SiP$^{iPr}_3$**)Fe(N_2)(H)	0.00	0.00	0.00	0.00	0.00	0.00	THF	1/4		20	60
S58	(**SiP$^{iPr}_3$**)Fe(N_2)(H)	0.00	0.00	0.00	0.00	0.00	0.00	C_6D_6	1/4		20	90
S59	(**SiP$^{iPr}_3$**)Fe(N_2)(H)	0.00	0.00	0.00	0.00	0.00	0.00	THF	29/29		20	100
S60	(**SiP$^{Ph}_3$**)Fe(N_2)(H)	0.00	0.00	0.00	0.00	0.00	0.00	THF	29/29		20	100
S61	(**PhBP$^{iPr}_3$**)FeCl	0.00	0.00	0.00	0.00	0.00	0.00	THF	29/29		20	100
S62	[(**NP$^{iPr}_3$**)Fe(N_2)(H)](PF_6)	0.00	0.00	0.00	0.00	0.00	0.00	THF	29/29		20	100

Entry	Precatalyst	$(Et_3NH)(OCHO)$ Yield (mmol)	MeOCHO Yield (mmol)	Total Yield (mmol)	$(Et_3NH)(OCHO)$ TON[a]	MeOCHO TON[a]	Total TON[a]	Solvent	P_{CO_2}/P_{H_2} (atm)	Additive[b]	Time (h)	Temp. (°C)
S63	(**TPB**)(μ–H)Fe(N_2)(H)	0.00	0.00	0.00	0.00	0.00	0.00	THF	29/29		20	100
S64	(**TPB**)(μ–H)Fe(N_2)(H)	0.00	0.00	0.00	0.00	0.00	0.00	C_6D_6	1/4		20	100
S65	(**CP$^{iPr}_3$**)FeCl	0.20	0.03	0.23	24.71	3.43	28.13	MeOH	29/29		20	100
S66	(**CP$^{iPr}_3$**)FeCl	0.18	0.03	0.21	23.15	2.95	26.11	MeOH	29/29		20	100
S67	(**C^{Si}P$^{Ph}_3$**)FeCl	0.00	0.00	0.00	0.00	0.00	0.00	MeOH	29/29		20	100
S68	(**SiP$^{iPr}_3$**)FeCl	0.36	0.02	0.38	46.68	3.14	49.82	MeOH	5.5/29		20	100
S69	(**SiP$^{iPr}_3$**)FeCl	0.32	0.02	0.34	41.30	3.15	44.45	MeOH	5.5/29		20	100
S70	(**SiP$^{iPr}_3$**)FeCl	0.00	0.00	0.00	0.00	0.00	0.00	MeOH	29/5.5		20	100

Unless otherwise noted, reactions were performed under the standard conditions of 0.7 mM precatalyst, 651 mM of triethylamine, methanol (10 mL), 20 h, 100 °C, 29 atm of CO_2, and 29 atm of H_2. [a]Turnover number (TON) is the yield of product divided by the amount of added precatalyst. [c]$(Et_3NH)(OCHO)$ was detected by ^1H NMR spectroscopy, but $(Et_3ND)(OCDO)$, $(Et_3NH)(OCDO)$, and $(Et_3ND)(OCHO)$ were not detected by ^2H NMR spectroscopy. [b]$BAr^F_4 = [B(3,5\text{-}(CF_3\text{-}C_6H_3)_4)]^-$; TBAF = tetrabutylammonium fluoride.

A3.1 Hydricity Determination

Reactions relevant to determination of hydricity for (**SiP$^{iPr}_3$**)Fe(H_2)(H) (**Fe(H_2)(H)**)with a base (B), equation A3.1-A3.3. The sum of equations A3.1-A3.3 (ΣG, Scheme A3.1) represents the reverse reaction, where hydride is added to **Fe(H_2)$^+$**. Therefore, reversing the reaction and taking negative ΣG (-ΣG, equation A3.4) represents the hydricity (ΔG_H-) of Fe(H_2)(H).

Scheme A3.1 Reactions and equations relevant to hydricity determination for (**SiP$^{iPr}_3$**)Fe(H_2)(H).

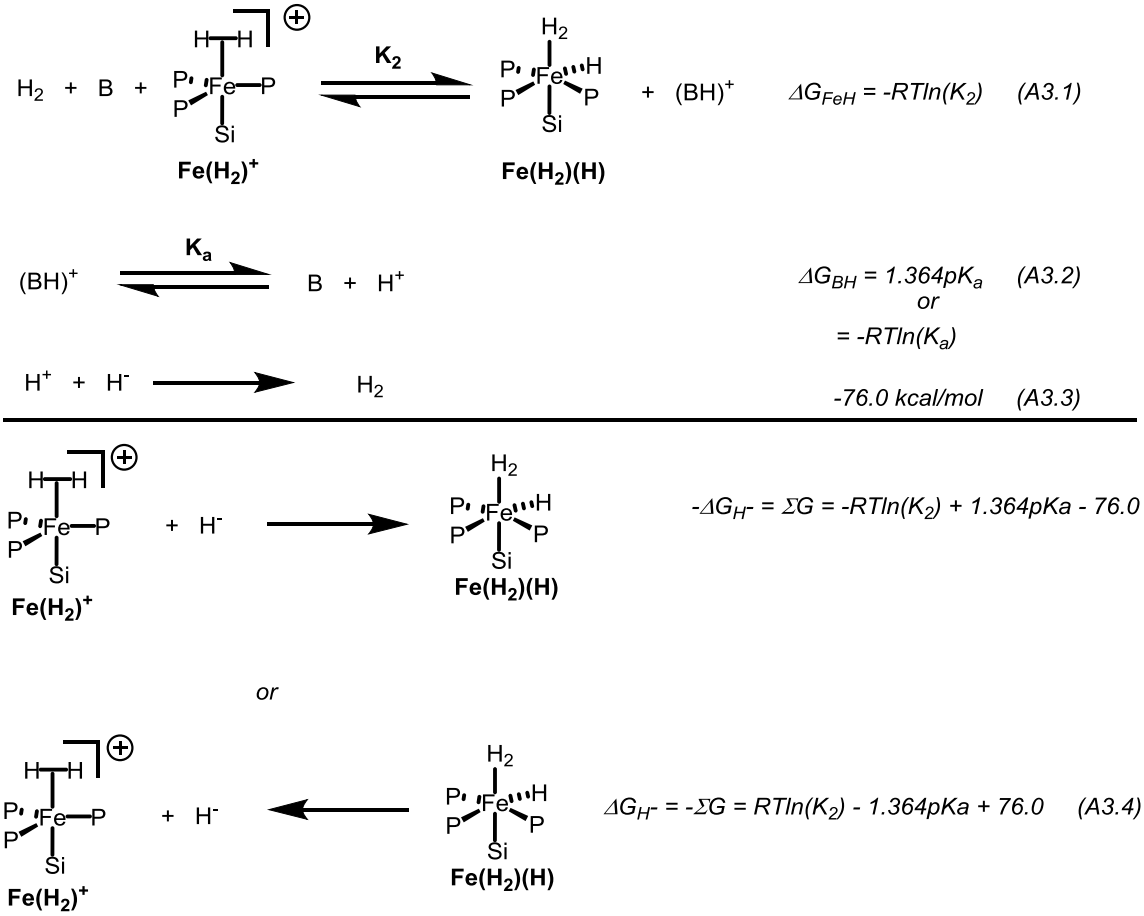

See Chart 4.1 for detailed ligand representation.

Experimentally, the deprotonation reaction of equation A3.1 was run in d_8-THF. However, THF is known to coordinate competitively to the cationic Fe^{II} complex to give **Fe(THF)$^+$**.[1] This must be taken into account. The equilibrium constant for the competitive coordination of H_2 and THF (equation A3.5) has been previously reported (K_1 = 1900 M^{-1}, equation A3.5).

Scheme A3.2 Equilibrium reaction for competitive THF/H_2 coordination by [(**SiP$^{iPr}_3$**)Fe(L)]$^+$.

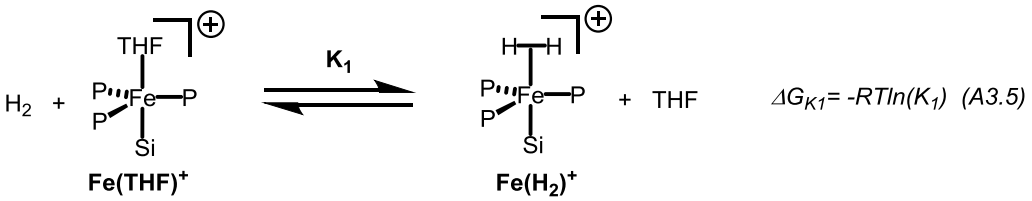

$$\textit{where } K_1 = \frac{[\mathbf{Fe(H_2)^+}][THF]}{[\mathbf{Fe(THF)^+}][H_2]} = 1900\ M^{-1}$$

Therefore, the overall reaction of equations A3.1 and A3.5 is:

$$\mathbf{Fe(THF)^+} + 2H_2 + B \overset{K_1}{\rightleftharpoons} \mathbf{Fe(H_2)^+} + H_2 + B + THF \overset{K_2}{\rightleftharpoons} \mathbf{Fe(H_2)(H)} + THF + BH^+ \quad (A3.6)$$

$$\textit{where } K_2 = \frac{[\mathbf{Fe(H_2)(H)}][BH^+]}{[\mathbf{Fe(H_2)^+}][B][H_2]}$$

And the total concentration of iron species in solution is:

$$[Fe]_{total} = [\mathbf{Fe(H_2)(H)}] + [\mathbf{Fe(H_2)^+}] + [\mathbf{Fe(THF)^+}] \quad (A3.7)$$

Experimentally, the equilibrium between the iron-species and base in d_8-THF was monitored by ^{1}H NMR spectroscopy with 1,3,5-trimethoxybenzene as an integration standard. The proton resonances from the **Fe(H$_2$)(H)**, base, and conjugate acid of the base were well-resolved and

reliably integrated in the ^{1}H NMR spectra, but the paramagnetic **Fe(H$_2$)$^+$** and **Fe(THF)$^+$** could not be reliably integrated. Therefore, equation A3.7 and K_1 were used to determine the respective concentrations of **Fe(H$_2$)$^+$** and **Fe(THF)$^+$** in order to determine the equilibrium value K_2. The activity of hydrogen at 1.0 atm was taken as unity in K_2, as this is the reference state of hydrogen for the normal hydrogen electrode.[2]

Table A3.2 Experimentally determined ΔG_{H^-} for (**SiP$^{iPr}_3$**)Fe(H_2)(H) and pK_a values for [(**SiP$^{iPr}_3$**)Fe(H_2)](BAr$^F_4$) using three different bases.

Entry	Acid	Base	K_2 (M^{-1})	(**SiP$^{iPr}_3$**)Fe(H_2)(H)	[(**SiP$^{iPr}_3$**)Fe(H_2)](BAr$^F_4$)	
				ΔG_{H^-} (kcal/mol)	pK_a^{THF}	pK_a^{MeCN}
1	[(**SiP$^{iPr}_3$**)Fe(H_2)](BAr$^F_4$)	Proton Sponge (pK_a^{THF} = 11.1)[a]	4.31[b]	54.8	10.5	15.5
2	[(**SiP$^{iPr}_3$**)Fe(H_2)](BAr$^F_4$)	2,6-Lutidine (pK_a^{THF} = 7.2)[a]	3.3 x 10^{-5} [c]	52.9	11.7	16.9
3	[(**SiP$^{iPr}_3$**)Fe(H_2)](BAr$^F_4$)	2,4,6-Trimethyl-pyridine (pK_a^{THF} = 8.1)[a]	5.1 x 10^{-3} [d]	54.9	10.4	15.4
4	[Proton Sponge-H](BAr$^F_4$)	(**SiP$^{iPr}_3$**)Fe(H_2)(H)	2.6	54.5	10.7	15.8

[a]pK_a of conjugate acid, see ref 3. [b]1 equiv of proton sponge used. [c]292 equiv of 2,6-lutidine used. [d]20 equiv of 2,4,6-trimethyl-pyridine used.

A3.2 UV-vis Titration

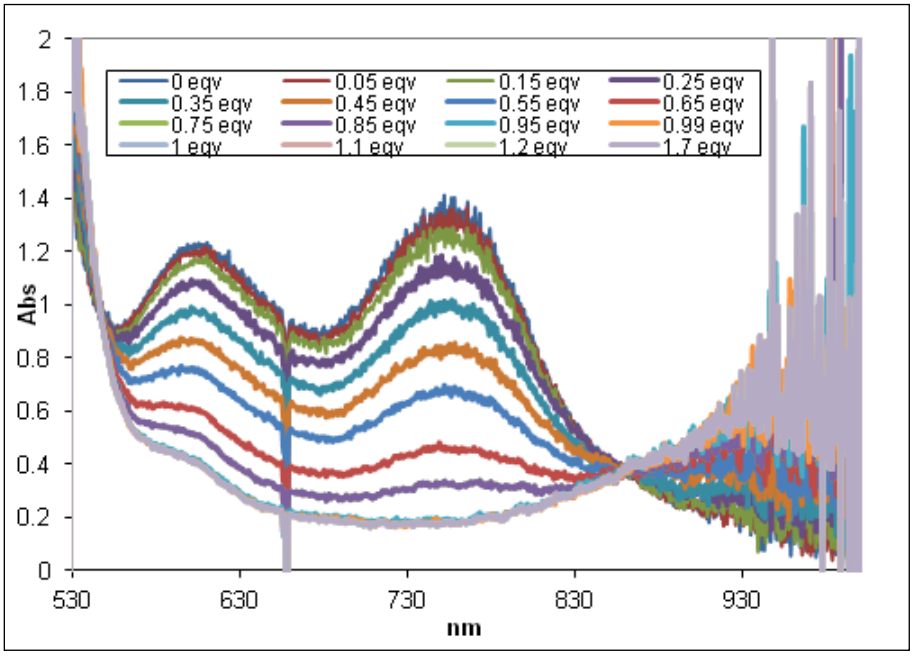

Figure A3.1 UV-vis spectra of the titration of [(**SiP$^{iPr}_{3}$**)Fe(N_2)](BAr^F_4) with Li(OCHO) in THF.

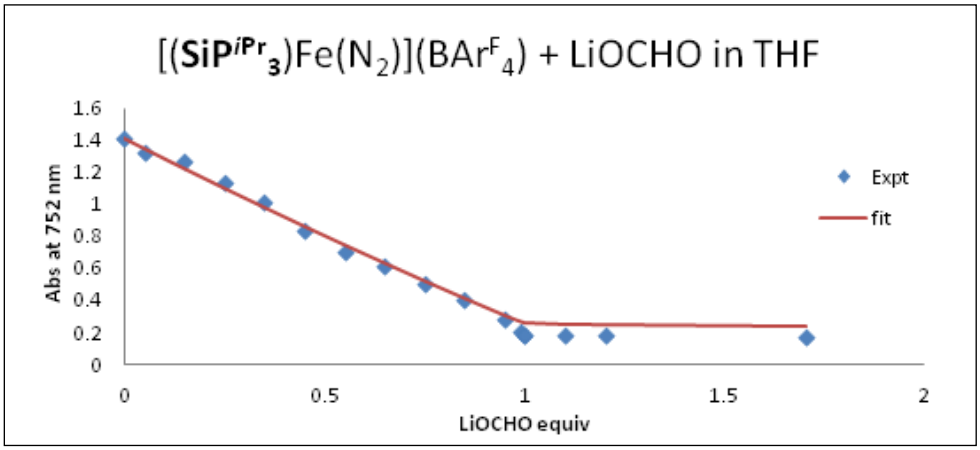

Figure A3.2 Fit of the UV-vis titration data. Absorbance at 752 nm as a function of the equivalents of Li(OCHO) added (blue diamond). The best fit of the data using K_{eq} = 3.5 x 10^6 M^{-1} is in red.

A3.3 Cited References

(1) Lee, Y.; Kinney, R. A.; Hoffman, B. M.; Peters, J. C. *J. Am. Chem. Soc.* **2011**, *133*, 16366-16369.

(2) Ciancanelli, R.; Noll, B. C.; DuBois, D. L.; DuBois, M. R. *J. Am. Chem. Soc.* **2002**, *124*, 2984-2992.

(3) Kaljurand, I.; Kütt, A.; Sooväli, L.; Rodima, T.; Mäemets, V.; Leito, I.; Koppel, I. A. *J. Org. Chem.* **2005**, *70*, 1019-1028.